UNIVERSITEIT VAN PRETORIA
UNIVERSITY OF PRETORIA
YUNIBESITHI YA PRETORIA

The effects of autogenous gas tungsten arc welding parameters on the solidification structure of two ferritic stainless steels

Prepared by

Heinrich Johann Prins

Submitted in partial fulfilment of the requirements for the degree
of Master of Engineering

University of Pretoria
Faculty of Engineering
Department of Material Science and Metallurgical Engineering

Supervisor: Prof. PGH Pistorius

February 2020

ABSTRACT

Ferritic stainless steel is typically used in the automotive industry to fabricate welded tube that is plastically deformed for flanging, bending and necking. The effect of welding parameters during autogenous gas-tungsten arc welding (GTAW) of thin sheet on the weld metal structure and tensile properties were determined. Two grades of ferritic stainless steels, a titanium-containing Grade 441 and a titanium-free molybdenum-containing Grade 436, were used as base metal. Statistical analysis was used to determine the influence of welding parameters on the microstructure of autogenous GTAW welds. The results of Grade 441 indicated that the welding speed and peak welding current had a statistically significant influence on the amount of equiaxed grains that formed. For Grade 436, the same welding parameters (welding speed and peak welding current) had a statistically significant influence on the grain size of the weld metal grains. The ductility of a tensile test coupon machined parallel to the weld direction, for both base metal grades, was unaffected by the welding parameters or the weld metal microstructure. The elongation was determined by the amount of weld metal in the gauge area of a tensile coupon. The titanium content of the base material seems to have the most significant effect on the formation of equiaxed grains.

Keywords: ferritic stainless steel, pulsed current, columnar grains, equiaxed grains, response surface regression

ACKNOWLEDGEMENTS

I have received a great deal of guidance, support and assistance throughout the writing of this thesis. I would firstly like to thank Columbus Stainless (Pty) Ltd. and its management who sponsored the project financially and provided the base materials. I would like to thank Sean du Toit for his expertise during the project as well as help with statistical analysis.

I want to thank the South African Institute of Welding (SAIW) for the financial sponsorship of my master's degree.

I would like to thank Joyce Jordaan and Gretel Crafford from the Department of Statistics at the University of Pretoria for assistance with statistical analysis of all the welding data, their expert analysis, their time and statistical advice.

Thank you to the Department of Material Sciences and Metallurgical engineering at the University of Pretoria for the opportunity to complete my master's degree.

Thank you to Lesego Makhafola, from the Faculty Library, for her advice and help with the writing of my thesis.

I would like to thank my supervisor, Prof. PGH Pistorius for his support and engineering expertise for the writing of this thesis. Prof. Pistorius's door was always open for discussion, guidance, help and I am gratefully indebted to him for his valuable time.

I would like to thank my parents, Johann and Beate Prins, for their sacrifices, love and support for me during my academic career. Thank you to my friend, Nico du Toit, for always checking in and his support.

I would like to thank my heavenly Father for my abilities to have taken on my master's degree and carrying me through my academic career.

Contents

List of Figures

List of Tables

List of Acronyms and abbreviations

CET		Columnar to equiaxed transition
GTAW	-	Gas tungsten arc welding
GMAW	-	Gas metal arc welding
FCC	-	Face centered cubic
BCC	-	Body centered cubic
SCC	-	Stress corrosion cracking
DBTT	-	Ductile-to-brittle transition temperature
HTE	-	High temperature embrittlement
CET	-	Columnar-to-equiaxed transition
FB	-	Fusion boundary
CL	-	Center-line
SEM-EDS	-	Scanning electron microscope – energy-dispersive X-ray spectroscopy
HAZ	-	Heat affected zone
DCEN	-	Direct current electrode negative
PWHT	-	Post-weld heat treatment
ASME	-	American Society of Mechanical Engineers
AC	-	Alternating current

List of letters and symbols

R	-	Solidification rate
G	-	Temperature gradient
v	-	Welding speed
N	-	Nucleation sites
R^2	-	Coefficient of determination
ρ	-	Statistical significance
t	-	Thickness
T	-	Temperature
I	-	Current

E	-	Energy
±	-	Addition or deletion
⌀	-	Change
>	-	Increase or greater than
HI	-	Heat input
V	-	Voltage
η	-	Arc efficiency
l	-	Length
f	-	frequency
$\sigma(\bar{x})$	-	Standard deviation
$\sigma(x)$	-	Fraction equiaxed grains/ columnar grain thickness/ equiaxed grain size
n	-	Number of points

CHAPTER 1: Industrial background

Modern ferritic stainless steels have good corrosion, heat and oxidation resistance. Newer ferritic grades, such as Grade 441, which is stabilised by titanium and niobium, have improved intergranular corrosion resistance (Outokumpu Stainless Oy, 2014). Ferritic stainless steels are replacing the use of expensive austenitic stainless steel due to a higher thermal conductivity, lower coefficient of thermal expansion, lower cost and increased resistance to stress corrosion cracking (SCC). Ferritic stainless steels are used where the typical application requires corrosion resistance rather than mechanical properties (Lippold & Kotecki, 2005).

Columbus Stainless (Pty) Ltd is the only South African flat rolled stainless steel producer. The plant produces a range of products which include ferritic, austenitic and duplex stainless steels. The ferritic stainless steel products are used in the automobile industry for exhaust systems. These exhaust systems operate at temperatures in the range of 600 to 900°C and temperature fluctuations in service are a common phenomenon (Mmadi, 2016). Grade 441 is typically used in the automotive industry, and to manufacture kitchenware and industrial equipment. Grade 436 has a higher molybdenum content for enhanced corrosion resistance and is used in hot water tanks, electric kettles and automotive exhaust parts (Bell, 2018). The typical chemical composition of ferritic stainless steel grades is shown in Table 1. The automotive exhaust system can be split up in different components, each being made of different or similar alloys, working at different temperatures, as noted in Table 2.

Table 1: Typical ferritic stainless steel compositions of the different components in automotive exhaust systems. The maximum values allowed are tabulated (EN 10088-1, 2005)

Grade	C	Si	Mn	N	Cr	Mo	Nb	Ni	Ti
409	0.03	1.00	1.00	-	12.50	-			0.65
429									
430	0.08	1.00	1.00	-	18.00				
436	0.08	1.00	1.00	0.04	18.00	1.40	1.00		
441	0.03	1.00	1.00	-	18.50		1.00		0.60
444	0.03	1.00	1.00	0.03	20.00	2.50			0.80

Table 2: Different automotive exhaust system components manufactured from ferritic stainless steel and typical operating temperatures (Inoue & Kikuchi, 2003; Mmadi, 2016)

Component	Service Temperature (°C)	Ferritic grades	Required Properties
Exhaust Manifold	950-750	409, 429, 430, 441, 444	• High temperature strength • Thermal fatigue life • Oxidation resistance
Front pipe	800-600		
Catalytic converter shell	800-600	409, 436, 441	• High temperature strength • High temperature salt damage resistance • Workability
Centre pipe	600-400	409, 441	• Salt damage resistance
Main Muffler	400-100	409	• Corrosion resistance on inner surface (condensate) • Corrosion damage at outer surface (salt damage)
Tail end pipe	400-100	409, 430, 436	• Corrosion resistance in inner surface (condensate) • Corrosion damage at outer surface (salt damage)

The biggest industrial problem with welding of ferritic stainless steels is the loss of ductility and toughness (Amuda & Mridha, 2011). During the fabrication of exhaust systems, the pipe blanks are often welded autogenously, after which the blank is deformed during flanging, resizing or bending. During deformation, the weld metal may crack. It is therefore important to better understand the welding behaviour of these alloys and find solutions that are cost effective to ensure a welded joint with adequate strength, ductility and toughness. The welding of ferritic stainless steels is difficult as columnar grains dominate the weld metal microstructure, partly because of excessive grain growth in the heat affected zone at high temperatures. The pulse welding of ferritic grades increases the amount of equiaxed grains within the microstructure, but a lower toughness than the base metal is still experienced (Reddy & Mohandas, 2001).

CHAPTER 2: Physical metallurgy and welding of ferritic stainless steel

2.1 Chemical composition and microstructure of stainless steels

Stainless steels are iron based alloys with a chromium content above 10.5%. The selection of stainless steels is typically based on cost, corrosion resistance, fabrication, mechanical properties and in-service temperature (Davis, 1993). Stainless steels are classified into five categories based on the microstructure of the steel. Martensitic stainless steels typically have chromium contents of 10.5 to 18%. The martensitic stainless steels are only resistant to mildly corrosive environments and are hardenable by heat treatment (Davis, 1993). Austenitic stainless steels have chromium contents that vary between 16 to 26%. Austenite has a face-centered cubic (FCC) crystal structure that is achieved by alloying with manganese, nickel or nitrogen. Duplex stainless steels contain a mixture of austenite (FCC) and ferrite (body-centered cubic - BCC). The exact mixture of phases present is a function of the chemical composition and heat treatment. Precipitation-hardening stainless steels contain elements such as copper, titanium and aluminium that precipitation-harden the alloy (Davis, 1993).

Ferritic stainless steels typically have chromium contents of 10.5 to 30%. Ferritic stainless steels exhibit excellent corrosion properties, are less susceptible to stress corrosion cracking and have a lower cost than austenitic stainless steels (Davis, 1993). However, grain growth can have detrimental effects on the mechanical properties of welded ferritic stainless steels (Amuda & Mridha, 2011).

2.2 Chemical composition of ferritic stainless steels

Ferritic stainless steels are iron-carbon-chromium alloys. Aluminium (Al), titanium (Ti), molybdenum (Mo) and niobium (Nb) may be added. These alloys typically exhibit a loss in toughness as the thickness of the material is increased. Stresses acting on discontinuities in a component vary with thickness. As the thickness is increased, the stress-strain field changes from a plane strain state to a plane stress state, which indicates that the defect will be in tension in three dimensions (thicker material) and the plastic zone will be smaller (Zhang, Zhang, Zhao, Wang &Li, 2016). The work per unit area for crack tip necking is decreased as the thickness of the material is increased. This is influenced by the combined effects of the microstructure, presence of micro-defects, roll marks and the stress which increases triaxially with thickness (Kang, Zhang, Wang, Qin, 2005). This effect governs the toughness for both base metal and welded joints.

It is because of this loss of toughness that the thickness of these alloys is limited to thinner gauges. For ferritic stainless steels, carbon affects the toughness negatively and is kept to a minimum. The most recent alloys are stabilized with nitrogen for nitride formation. This improves the toughness properties, reduces the risk for intergranular cracking and reduces the risk to stress corrosion cracking (SCC) and pitting corrosion (Singh, 2012).

Since no austenite transformation occurs, ferrite is stable at all temperatures up to the melting temperature. Consequently, ferritic stainless steels cannot be hardened by means of quenching and phase transformations. In some ferritic stainless steel alloys, small amounts of austenite transformation do occur due to interstitials being present in the alloy. These small amounts of austenite transform to martensite after heating or welding. Annealing after welding at temperatures of 760 to 815°C may be done to restore the previous corrosion resistance properties (Singh, 2012).

Molybdenum is effective in stabilising the passive surface oxide film together with chromium when exposed to chloride-containing environments. Molybdenum therefore helps to improve the resistance to pitting and crevice corrosion. (O'Brien & Guzman, 2011). Titanium and niobium are useful in small concentrations due to their high affinity for carbon and nitrogen. Aluminium is also added to combine with nitrogen or for oxidation resistance improvements at high temperatures. Silicon is added as a deoxidizer in the molten condition and provides resistance to oxide-scaling (Lippold & Kotecki, 2005).

2.2.1 Embrittlement of ferritic stainless steels

Some ferritic stainless steel grades are higher in chromium and carbon content. These grades tend to form a chromium-rich grain boundary precipitate that leaves the adjacent area to the grain boundary depleted in chromium with a detrimental effect on the corrosion resistance and toughness. This phenomenon is known as intergranular corrosion or sensitisation (O'Brien & Guzman, 2011; McGuire, 2008). Specific ferritic grades can be sensitised during welding in the heat affected zone (Bell, 2018).

The ductile-to-brittle transition temperature (DBTT) of ferritic stainless steels is usually above room temperature (O'Brien & Guzman, 2011). The higher the chromium content of the alloy, the higher the risk of forming brittle phases such as sigma and alpha prime. All ferritic stainless steel grades are susceptible to extensive grain growth at temperatures above 927°C. The large grains lower the toughness (Singh, 2012).

4

The second embrittling phenomenon is 475°C embrittlement due to the formation of α' (alpha prime), which is a chromium-rich ferrite that forms after about 100 hours of ageing in the temperature range of 425 to 550°C. Alloying elements such as titanium, niobium and molybdenum tend to accelerate the onset of 475°C embrittlement. 475°C embrittlement can be eliminated by heating the alloy to temperatures between 550 to 600°C for short times. Heating to this temperature range allows for an annealing treatment that restores the stainless steel mechanical properties such as toughness (Lippold & Kotecki, 2005).

Hydrogen embrittlement can in general be induced by a welding process when martensite forms along the ferrite grain boundaries. Ferritic stainless steels are typically not susceptible to hydrogen embrittlement as martensite typically does not form in grades with a higher chromium content (O'Brien & Guzman, 2011).

Sigma (σ) phase is an iron-chromium intermetallic compound that forms from ferrite at temperatures ranging from 500 to 800°C. σ-phase formation in the welded joint has a detrimental effect on the mechanical properties of the weldment as it is difficult to prevent with stainless steel alloys containing 20% or more chromium. The effects of σ-phase formation can be countered by heating the alloy to temperatures above 800°C for short times to allow dissolution (McGuire, 2008; Lippold & Kotecki, 2005).

The welding of ferritic stainless steels increases the temperature in the heat affected zone to temperature ranges where rapid grain coarsening can occur. The amount of grain coarsening will be a function of the peak temperature experienced and the time spent at this temperature. Grain coarsening causes ferritic stainless steels to be susceptible to high temperature embrittlement (HTE), which leads to a decrease in toughness and ductility of the weld metal and HAZ of the welded joint (O'Brien & Guzman, 2011).

2.3 Welding metallurgy of ferritic stainless steels

2.3.1 Solidification during welding

During solidification, the solid phase nucleates in the liquid metal. This nucleation can occur by means of homogeneous or heterogeneous nucleation. Homogeneous nucleation occurs spontaneously in the liquid when a nucleus of critical size is reached. Heterogeneous nucleation occurs mainly on foreign particles such as oxide, sulphides, nitrides or on existing solid substrates. Little or no constitutional supercooling is required

5

for heterogeneous nucleation. Heterogeneous nucleation on a solid substrate is known as epitaxial growth and is the main solidification mechanism in autogenous fusion welds that has no nucleation barrier (Chalmers, 1964). With epitaxial growth there is complete wettability between the liquid weld metal and the fusion line and nucleation of the liquid can occur easily. The grains tend to grow in the direction where the temperature gradient is higher. This leads to the grains growing perpendicular to the fusion boundary (Savage, Nippes & Miller, 1976).

The solidification occurs preferentially on the <100> direction also known as the easy-growth direction - Figure 1. The <100> growth direction is maintained as long as the solidifying grains remain in contact with the solid-liquid interface or until they are grown out of existence by means of adjacent grains that are more favourably orientated, a mechanism known as competitive growth. Heterogeneous nuclei can cause grain growth in advance of the solid-liquid interface. Heterogeneous nucleation typically occurs in the centre of the weld bead where the temperature gradient is lowest (Lippold, 2015; Farahani, Shamanian & Ashrafizadeh, 2012).
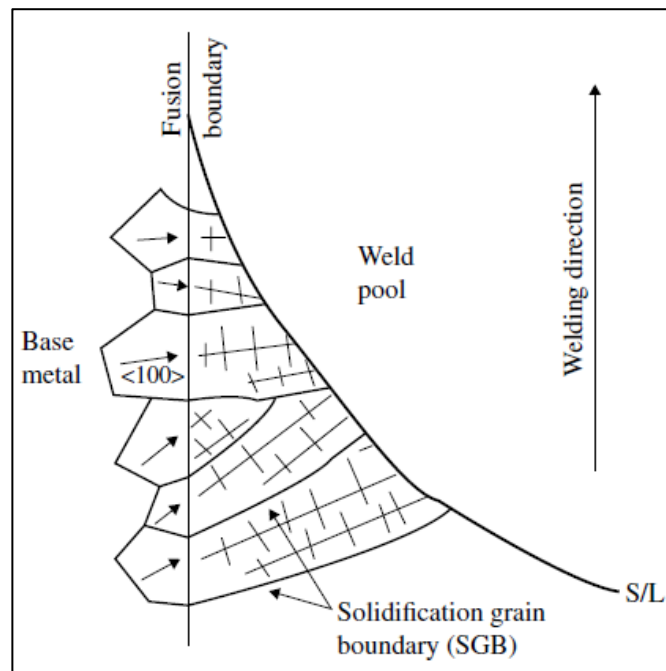
Figure 1: Epitaxial growth from an existing substrate in <100> direction (Lippold, 2015)

Villafuerte and Kerr (1990) used gas tungsten arc welding (GTAW) on ferritic and austenitic stainless steel, with full penetration bead-on-plate autogenous welds - Figure 2. They found that an increase in the titanium

and aluminium content (0.29% and 0.04% respectively) and the welding speed (14 mm/s) lead to an increase in heterogeneous nucleation (Villafuerte & Kerr, 1990).

The growth rate, constitutional supercooling, temperature gradient and alloy composition govern the final solidification structure (David, Babu & Vitek., 2003). Villafuerte, Pardo & Kerr welded different titanium grades of Grade 409 ferritic stainless steel. They found that the amount of equiaxed grains that form in the weld metal was determined by the welding speed as indicated by Figure 2. They also found that the average equiaxed grain size was determined to be a function of the titanium content as indicated by Figure 3 (Villafuerte, Pardo & Kerr, 1990).
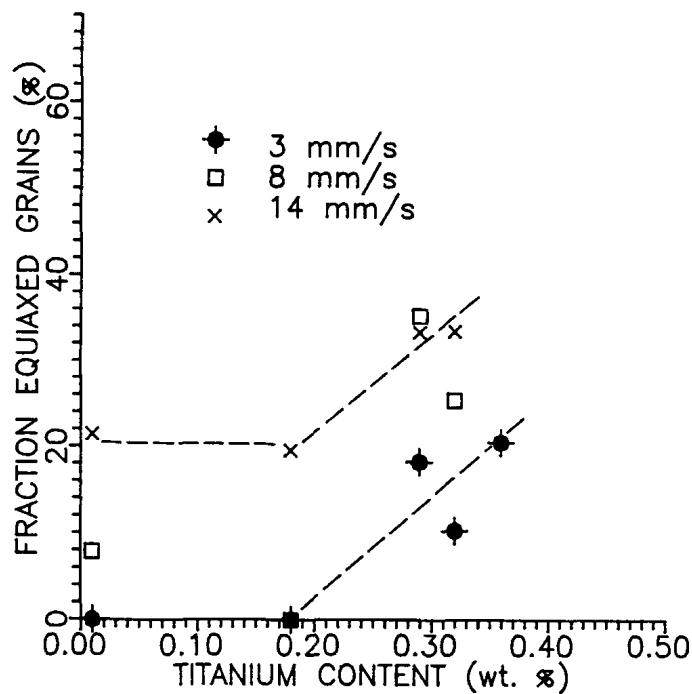
Figure 2: Effect of titanium content and welding speed on the amount of equiaxed grains forming in the weld metal of Grade 409 ferritic stainless steel, welded with GTAW. Aluminium content increased from 0.012% to 0.044% as titanium content increased (Villafuerte, Pardo & Kerr, 1990)
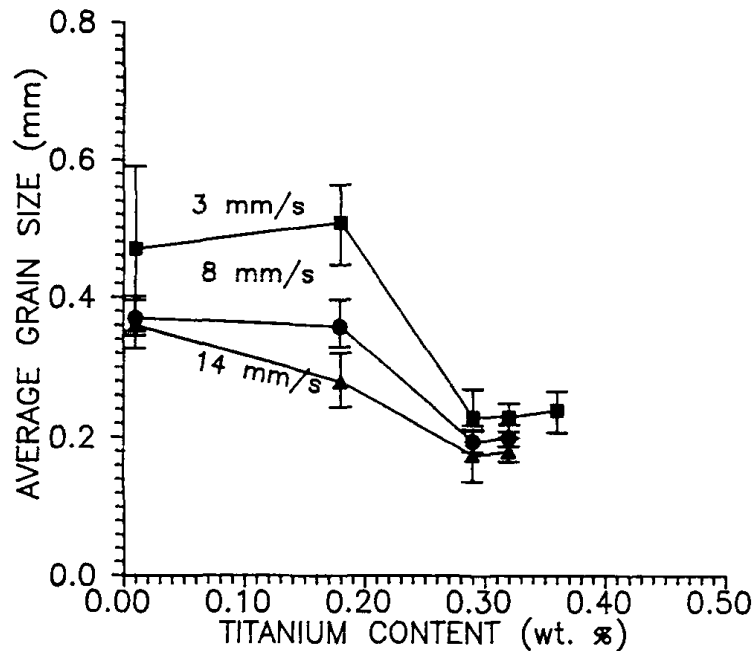
Figure 3: Effect of titanium content and welding speed on the size of the surface equiaxed grains of 409 ferritic stainless steel, welded with GTAW. The aluminium content increased from 0.012% to 0.044% as the titanium content increased (Villafuerte, Pardo & Kerr, 1990)

Villaret, Deschaux-Beaume, and Bordreuil examined the effect of titanium content on the amount of equiaxed grains that formed in full penetration gas metal arc welding (GMAW) butt-welds in Grade 444 ferritic stainless steel - Figure 4. A fully equiaxed weld structure was achieved with a titanium content of 0.15%. As the transfer ratio of titanium during welding is low, the filler metal had to contain twice the titanium content of that in the microstructure (Villaret, Deschaux-Beaume, & Bordreuil, 2013).

The cooling rate plays an important role in determining the solidification structure. If the cooling rate is high, a cellular solidification structure is expected to dominate. With a medium cooling rate, a dendritic solidification structure is expected. In stainless steel weld metals, it can occur that a cellular solidification structure appears at the weld bottom, while dendritic structures occur in the center of the same weld bead. The direction of growth is determined by the direction in which the highest heat dissipation occurs. Constitutional supercooling determines the solidification mode and varies significantly in a weld pool (Chalmers, 1964).
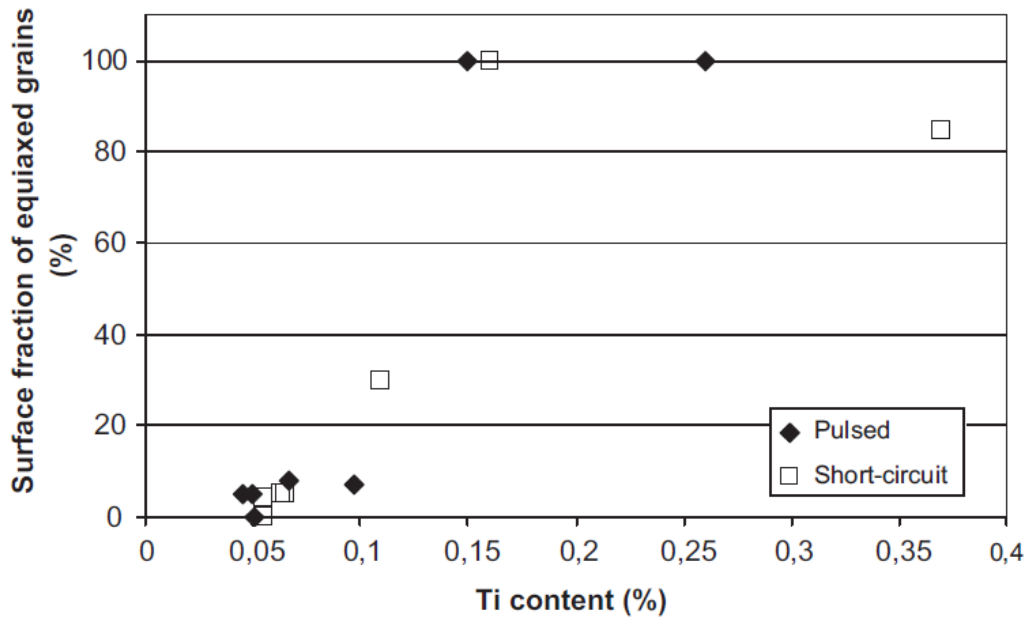
Figure 4: Amount of equiaxed grains in the weld metal as a function of the titanium content for welding of 444 ferritic stainless steel by means of short circuit transfer GMAW and pulsed GMAW (Villaret, Deschaux-Beaume, & Bordreuil, 2013)

The highest amount of constitutional supercooling will occur in the center of the weld bead. Cellular growth occurs from the solid-liquid interface towards the heat source as indicated by Figure 5. These cellular crystals then change into dendrites which are directed into the preferred orientation. At the weld pool center, the dendrites that grow are non-directed. Molybdenum or titanium is sometimes added to retard the growth of columnar grains in the weld pool. These additions allow nucleation to occur within the weld pool, but do not contribute significantly to the impact toughness of ferritic stainless steels (Folkhard, 1987).
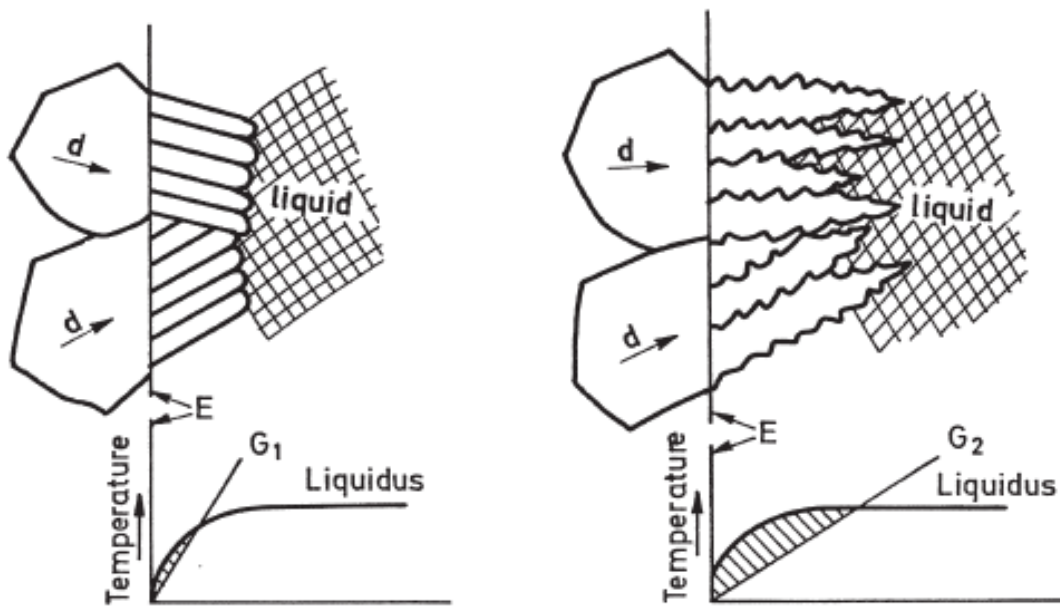
***Figure 5: Difference in solidification mode due to the amount of supercooling after welding. Left –
cellular structure: high cooling rate. Right – cellular-dendritic structure: medium cooling rate
(Folkhard, 1987)***

For the same welding solidification parameters, a higher alloyed material will contain more columnar dendritic structures compared to a cellular/cellular dendritic solidification structure for a lower alloyed material. This effect is illustrated in Figure 6. Closer to the weld center, the temperature gradient (G) decreases and the solidification velocity (R) increases. This indicates that in a low alloyed base material, more of the weld metal will contain cellular and cellular-dendritic structures. For a higher alloyed material, the solidification mode will also move to a columnar dendritic structure closer to the weld center (Lippold, 2015).
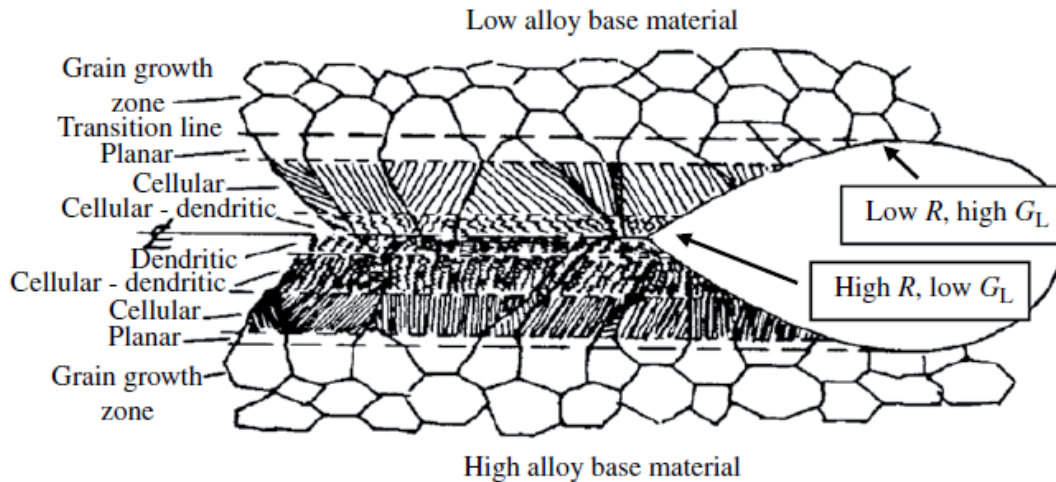
Figure 6: Schematic of typical solidification structures that occur in low and high alloy base materials respectively (Lippold, 2015)

The main solidification structures for most alloys are the cellular and the cellular-dendritic structures. The structure formation is typically determined by the alloy composition, temperature gradient (G) and solidification velocity (R) (Lippold, 2015). Equiaxed dendritic structures (illustrated in Figure 7) are usually not observed in fusion welds. Equiaxed dendrites can be present, where the temperature gradient (G) is very low due to the welding arc being extinguished. This mechanism may be active during current pulsing (Lippold, 2015).

Electromagnetic forces generated by interaction between the welding current and the induced magnetic field cause weld pool stirring. These stirred weld pools have two temperature cycles in the weld pool indicated by Figure 8 (Kim & Na, 1998; Villafuerte & Kerr, 1990).
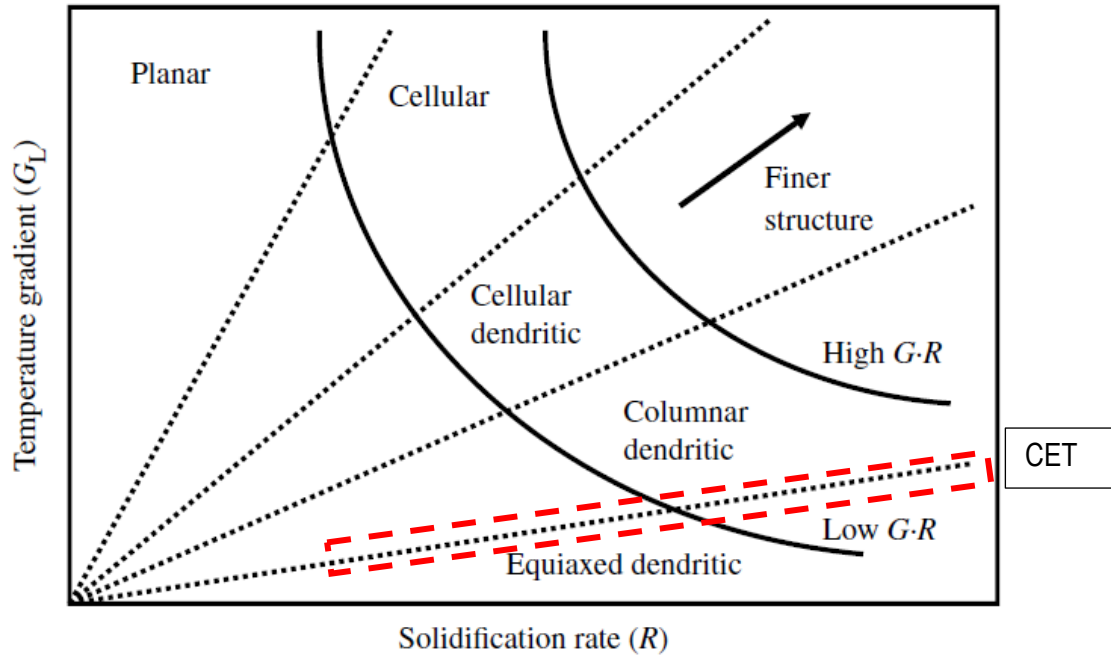
Figure 7: Graphic representation of the solidification mode of most alloy welds as a function of temperature gradient (G) and solidification velocity (R) (Lippold, 2015). The added dotted box describing the columnar to equiaxed transition (CET) was marked in red
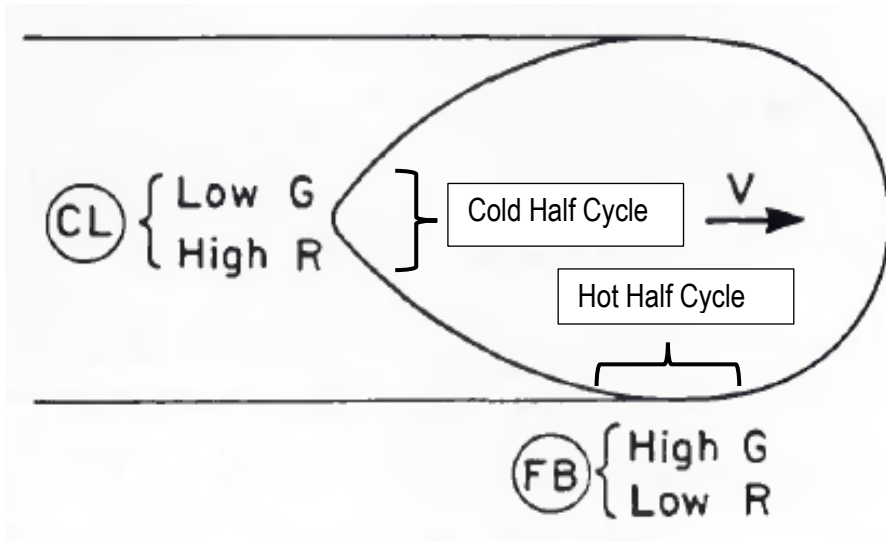
Figure 8: Indication of where the two temperature cycles occur in the weld pool. V – welding speed and weld direction, G – temperature gradient, R – solidification velocity, FB – fusion boundary, CL – center line of weld (Villafuerte & Kerr, 1990)

During the hot half cycle, the overheated liquid reaches the solid-liquid interface and increases the temperature gradient (G) within the liquid. Due to the temperature gradient increasing, the rate of solidification (R) decreases. This cycle decreases the constitutional supercooling, reducing the likelihood of equiaxed grain formation. (Lippold, 2015; Villafuerte, Kerr & David, 1995; Villafuerte & Kerr, 1990)

During the colder half cycle, the fluid motion in the weld pool is reversed, which drops the liquid temperature ahead of the solid-liquid interface. This lowers the temperature gradient (G) and increases the rate of solidification (R). This leads to the constitutional supercooled zone to increase and leads to the formation of dendrite fragments. (Lippold, 2015; Villafuerte, Kerr & David, 1995; Villafuerte & Kerr, 1990)

The use of the term "half cycle" may be interpreted to imply pulsing, which is not considered in the arguments presented by these authors. This decrease of the temperature gradient from the fusion line to the weld center favours crystal structures that transform from cells to branched dendrites (Villafuerte, Kerr & David, 1995) These temperature fluctuations close to the solid-liquid interface lead to the dendrite fragmentation, which is considered to be the main mechanism responsible for the growth of equiaxed grains (Kou, 2003).

As the welding speed increases, the solidification velocity increases. For a faster welding speed, a corresponding increase in welding current is required to maintain a full penetration weld, which will lead to a decrease in the temperature gradient (G) at the center line of the weld (Villafuerte & Kerr, 1990).

2.3.2 Columnar to equiaxed transition (CET) during solidification

During welding of ferritic stainless steel, the fusion zone's microstructure typically exhibits a fully columnar grain structure that is detrimental to the mechanical properties of the welded joint (Davis, 1993; Kou & Le, 1988). Equiaxed grain structures in the weld center are desirable due to being more isotropic, reducing the probability of segregation and enhancing the toughness (Villafuerte, Kerr & David, 1995). For columnar grains, crystal growth dominates and little to no nucleation is observed. The columnar grains grow in size until they reach their neighbouring columnar grains and grow in one preferred direction, the direction of heat-flow. The columnar crystal growth occurs when existing crystal in the base material or near mould walls have favourable directions that allow rapid columnar dendritic growth. Columnar crystal growth with less favourable directions are eliminated by the more favourable directed ones. The elimination of the less favoured grains

leads to larger diameter columnar grains closer to the central zone of welds or castings (Abbaschian, Abbaschian & Reed-Hill, 2009).

The columnar-to-equiaxed transition (CET) can only occur when nuclei or embryos are present ahead of the advancing columnar front and favourable thermal conditions for nuclei/embryos to survive and grow, exist (Villafuerte, Kerr & David, 1995). Enough undercooling-driven columnar growth and a sufficient number of heterogeneous nucleation sites (N) will initiate the columnar-to-equiaxed transition. For a given alloy, the number of available nuclei will be constant. Sufficient undercooling-driven columnar growth will help with the growth of equiaxed grains to block the growth of columnar grains, but will only be possible above a critical columnar solidification rate. The time for equiaxed grains to grow is dependent on the temperature gradient (G) (Villafuerte, Pardo & Kerr, 1990). The higher the number of nucleation sites (N), the wider the equiaxed grain zone will be in the weld bead (Jula, Dehmolaei & Alavi Zaree, 2018; Villafuerte & Kerr, 1990).

From Figure 9, the intersection of the centreline (CL) – fusion boundary (FB) line with the columnar to equiaxed transition lines will determine the location where the columnar to equiaxed transition will start and therefore the fraction of equiaxed grains in the weld metal. The figure also indicates that an increase in the number of nuclei will shift the columnar-to-equiaxed transition closer to the fusion boundary line, thus leading to a higher fraction of equiaxed grains (Villafuerte, Kerr, 1990). The goal is to shift the CL-FB line, which is controlled by the local thermal conditions (solidification rate (R) and temperature gradient (G)), into the equiaxed zone and so increase the fraction of equiaxed grains in the weld bead (Villafuerte & Kerr, 1990; Villafuerte, Pardo & Kerr, 1990).
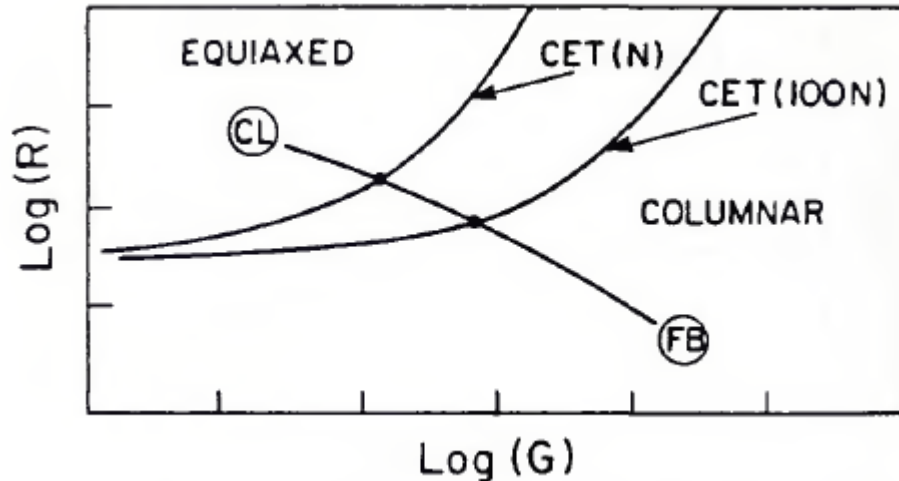
Figure 9: Map of temperature gradient (G) and solidification rate (R), indicating the regions where equiaxed and columnar grains are dominant, with addition of the columnar-to-equiaxed transition lines as functions of amount of nuclei (The 100N line indicates a larger amount of nuclei than the N line), where CL is the centreline of the weld and FB is the fusion boundary (Villafuerte & Kerr, 1990)

The columnar-to-equiaxed transition has been explained by different grain refining mechanisms; however, it remains difficult to determine the dominating mechanism. The mechanisms that enhances the CET include (Villafuerte, Kerr & David, 1995):

1. The breaking-off of dendrite arms or their partial remelting. Convection in the weld pool breaks off the dendrite tips and the fragments will act as new nuclei for new grain formation.
2. Heterogeneous nucleation occurs when grains can grow on an existing foreign solid particle (such as Ti(CN)) by means of inoculation which acts as nuclei for grains to nucleate heterogeneously with a reduced critical activation energy, without having to overcome the higher critical energy barrier for homogeneous nucleation.
3. Surface nucleation – which is followed by the free fall or break-off of surface dendrites. Surface nucleation occurs due to removal/reduction of heat input on the surface of the weld pool; it is therefore likely to be active during pulsed welds.
4. Gas impingement, electromagnetic stirring, magnetic arc oscillation and current pulsing.
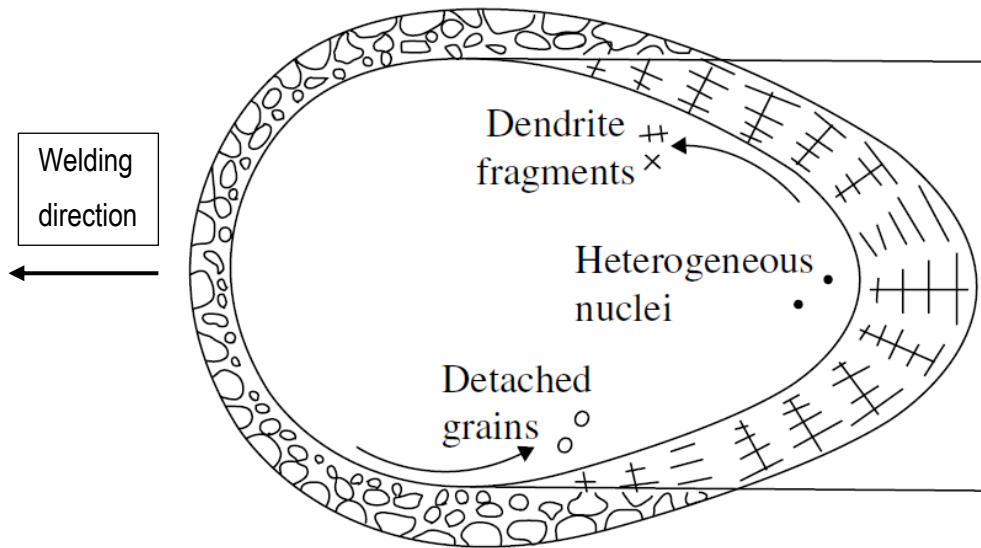
Figure 10: Schematic representation of different grain refining mechanisms that can occur during welding, when convection is present in the weld pool (Kou, 2003)

Figure 10 indicates the different grain refining mechanisms that can occur in a weld pool. Dendrite fragmentation and grain detachment, as proposed by Kou (2003), are grain refining mechanisms that have been cited in numerous articles as the main determining factors for equiaxed grain formation in ferritic stainless steels (Jula, Dehmolaei & Alavi Zaree, 2018; Farahani, Shamanian & Ashrafizadeh, 2012; Amuda & Mridha, 2011; Karunakaran & Balasubramanian, 2011; Reddy & Mohandas, 2001; Villafuerte, Kerr & David, 1995; Villavuerte & Kerr, 1990). A contrary point of view is that due to the relatively small size and interdendritic spacing of fusion welds, grain detachment may not be successful (Karunakaran & Balasubramanian, 2011).

High melting point particles formed in the weld pool can also act as nucleation sites. These particles can cause nucleation to occur on the surface of the solidifying weld pool, especially when an oxide surface layer is formed (Lippold, 2015). The region of equiaxed grains exists in the through thickness of the weld metal. The imposed magnetic field influences the fluid motion in the weld pool, as the welding current interacts with the magnetic field to cause Lorentz forces (Villafuerte & Kerr, 1990). The Lorentz force is the force being exerted on a particle that is charged and moving at a specific velocity through an electric and magnetic field (McElhinny & McFadden, 2000).

Previous studies on weld microstructures reported that aluminium and titanium-rich particles were present in the equiaxed grain centers, i.e. that heterogeneous nucleation is active during solidification (Villafuerte & Kerr, 1990). It is clear from previous investigations that the presence of TiN particles in equiaxed grains was associated with a mechanism of grain refinement (heterogeneous nucleation). Alloys without titanium had a fully columnar weld microstructure, however, the titanium addition alone was not responsible for equiaxed grains that form within the weld metal. It was suggested that the welding speed, titanium and aluminium additions jointly contribute to a higher fraction of equiaxed grains in ferritic stainless steel weld metal. It was stated that the equiaxed grains only formed in ferritic stainless steel that contained titanium. (Villafuerte, Kerr & David, 1995).

Titanium carbide precipitates are cubic in appearance and appeared randomly throughout the ferrite matrix of stabilised Grade 409. The TiC precipitates also nucleated on the existing TiN precipitates, with the TiN reaching stability before TiC precipitates on cooling. Energy-dispersive X-ray spectroscopy (SEM-EDS) analysis indicated that the dark region in the cubic precipitate was rich in nitrogen and the outer lighter regions rich in carbon (van Niekerk, du Toit & Erwee, 2012). Van Niekerk, du Toit and Erwee (2012) also concluded that TiN precipitates together with ferrite during solidification at a temperature of 1500°C, after which TiC will start to precipitate below 1150°C.

TiN precipitates were witnessed in the matrix of as-cast ferritic stainless steel microstructures. The particles were witnessed at or adjacent to the grain boundaries (Shi, Cheng, Li & Zhao, 2008). Due to the interface energy, the TiN particles will have a cubic morphology. TiN precipitates will form in the melt if the product of the titanium and nitrogen content is higher than the equilibrium concentration product at a specific temperature. It was shown by Fu, Qiu, Nie and Wu (2017), that the product of titanium and nitrogen contents are less than the equilibrium concentration at the liquidus temperature. This indicated that the TiN particles will not form from the melt, but rather that the particles will form during solidification as the solubility of titanium and nitrogen decreases as the melt temperature decreases. Solute redistribution during solidification will allow the accumulated titanium and nitrogen solutes to precipitate as TiN. The TiN precipitates that had formed above the liquidus temperature may allow heterogeneous nucleation of ferrite to occur on them (Fu, Qiu, Nie & Wu, 2017). This heterogeneous nucleation provides evidence of ferrite grain refinement of ferritic stainless steels with additions of titanium. It could therefore be interpreted that the grain refinement of ferrite

will lead to the formation of the equiaxed grains present in the weld metals of ferritic stainless steel that is stabilised with titanium.

2.3.4 Current Pulsing

Pulsed current GTAW was developed in the 1950's (Tong, Zhentai and Rui, 2013, Karunakaran & Balasubramanian, 2011). Pulsed current GTAW is suitable for applications where metallurgical control over the weld metal is critical (Farahani, Shamanian & Ashrafizadeh, 2012). Pulsed current works on the principle that the welding current is alternated between a high and low value. The peak welding current will allow adequate penetration and contouring of the weld bead, while the background current allows for solidification and maintains a stable arc. The cycle between peak- and background current occurs at a fixed frequency. The welding speed divided by the pulse frequency determines the amount of weld bead overlapping. The pulse on-time can also be changed on certain welding power supplies. The pulse on-time indicates the ratio of the peak current to the background current time for one pulse and is typically selected as 1:1 or 2:1 (Farahani, Shamanian & Ashrafizadeh, 2012).

The pulsing of current allows arc energy to be used efficiently while fusing small overlapping spots. The pulsing current also limits the amount of heat loss through conduction to the surrounding base material. Fusion energy is only supplied during the peak welding time, while heat is allowed to dissipate through the surrounding base material leading to a narrower HAZ (Karunakaran & Balasubramanian, 2011).

The pulsing of current causes cyclic variation in the energy input that leads to thermal fluctuations in the weld pool and causes a constant interruption of the weld solidification process. When the peak current decays (Point 1 in Figure 11), the solid-liquid interface moves towards the arc. When the current increases from the background current (Point 2 in Figure 11), the growth is arrested and remelting of the growing dendrites occurs (Karunakaran & Balasubramanian, 2011).
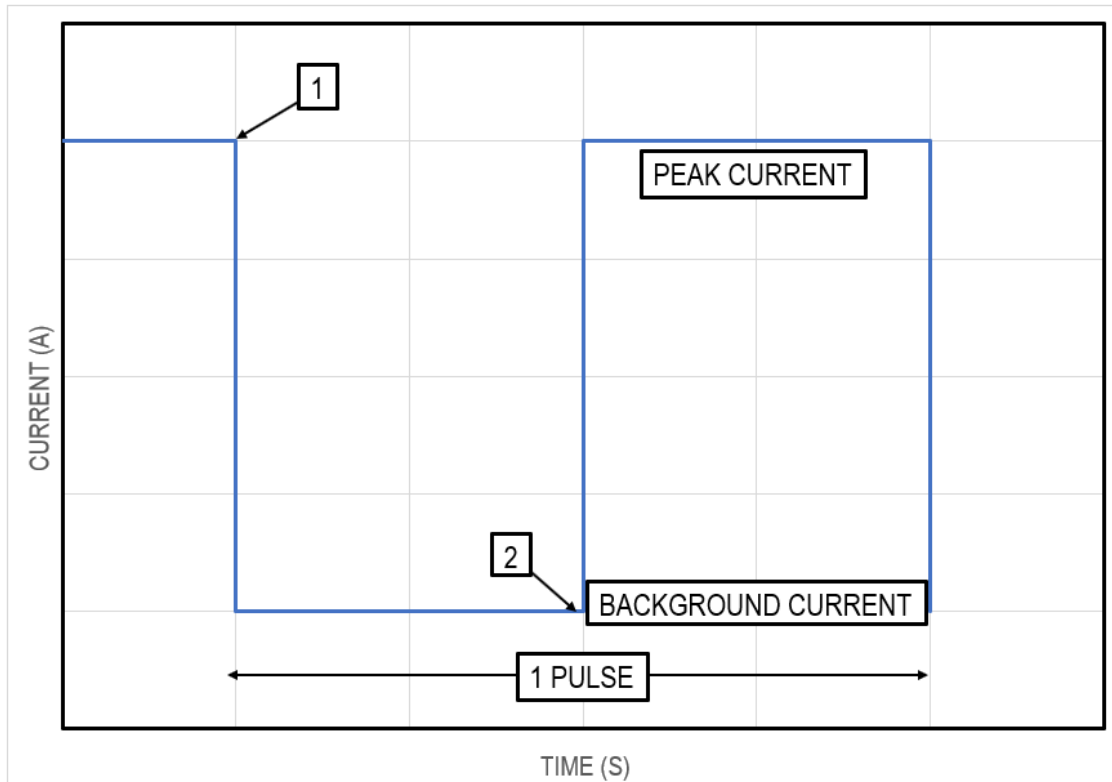
Figure 11: Schematic of how current is pulsed between peak- and background currents over time for one pulse. Point 1: Peak welding current decays. Point 2: Current increases from background current to peak welding current. The pulse on-time ratio is indicated as 1:1

The true energy input to a weldment during the use of pulsing or a more complex waveform, is not simply determined by means of average current and voltage values. Instead, the use of pulsing requires equipment that can capture the instantaneous voltage and current values at a high acquisition frequency. This is to ensure that the instantaneous power and energy is calculated at a similarly high rate. The energy input to the weld is determined by integrating the instantaneous power over time (Melfi & Daniel, 2010).

Arc forces are periodically changed due to the pulsing current and allows additional fluid flow to occur in the weld pool (Karunakaran & Balasubramanian, 2011). This additional fluid flow allows the temperature to decrease ahead of the solidifying interface. Temperature fluctuations are inherent to pulsed current welding and lead to continuous changes of the weld pool shape and size that favours the growth of new grains. Although grain refinement was cited to be due to dendrite fragmentation, it could never be observed due to the fragments growing to form the equiaxed grains during solidification. It is therefore imperative to note that

the effects of grain refinement were probably due to the pulse effects on the weld pool shape, the fluid flow in the weld pool and temperature fluctuations (Karunakaran & Balasubramanian, 2011).

A change of forces in the arc and melt is typically affected by modifying process parameters such as current, temperature and arc heat distribution. These modifications can lead to different stirring forces on the weld pool and is subsequently done by current pulsing or by applying an external magnetic field. Current pulsing has two effects on the weld pool: the plasma momentum increases and the electromagnetic body force value in the weld pool increases (Saedi & Unkel, 1988).

The electromagnetic body force is the result of the action between the applied current on the imposed magnetic field. Since current pulsing increases the electromagnetic body force, the use of current pulsing could therefore change the geometry of the weld bead. Studies indicated that the main influencing factor for weld bead geometry was the stirring force in the weld pool. These stirring forces were due to the increased electromagnetic forces that are associated with current pulsing. Current pulsing also increased the weld penetrating depth without influencing the weld bead width. As a result, current pulsing changes the geometry of the weld bead (Saedi & Unkel, 1988). The increased convection and oscillation presumably allow dendrite tips to be broken off, where these broken tips will act as new nuclei (Jula, Dehmolaei & Alavi Zaree, 2018).

During pulsed current welding, the electrical arc energy is abruptly reduced when the welding current drops to the background current. This ensures that the weld pool temperature decreases and allows for the molten metal to undergo supercooling, where surface nucleation increases and the nuclei will be stable due to the decreased electrical arc energy. The intermittent change between peak welding current and background current also contributes to the weld pool having increased convection and oscillation that leads to the nuclei being evenly spread throughout the weld metal. Due to epitaxial growth occurring during welding, the dendrite tips in the mushy zone are broken off due to the increased convection and oscillation in the weld pool. These dendrite fragments then act as new heterogeneous nucleation sites in the weld pool (Jula, Dehmolaei & Alavi Zaree, 2018).

The continuous change of the weld pool shape during pulsed current welding is of particular importance. At the solid-liquid interface, the temperature gradient changes as the weld pool shape changes with the effect of newer grains being favourably orientated as illustrated by Figure 1. This type of grain growth allows the

grains to grow over shorter distance. The shorter distances that the grains grow, results in new grains to be more favourably orientated and a finer grain size (Karunakaran & Balasubramanian, 2011). It was observed that the pulse frequency and background current did not have an effect on the depth of penetration achieved by a single pass weld. The peak welding current and the pulse on-time were the main pulsing parameters to affect the depth of penetration with similar weld bead widths (Manikandan, Nageswara, Ramanuiam & Ramkumar, 2014).

It is possible to change the welding parameters specifically by using pulsed current, where the epitaxial columnar growth transforms to equiaxed growth. This is done by limiting the amount of heat input into the welding process, typically by welding faster than for conventional constant current welding (David, Babu & Vitek, 2003). The use of pulsed current GTAW on Grade 430 ferritic stainless steel with unknown additions of titanium and aluminium, can improve the ductility of the weld metal by 20% as compared to conventional welds (Amuda & Mridha, 2011).

In order to reduce the heat input during welding it is suggested to use pulsed current that also acts as a grain refining mechanism. (Abu-Aesh, Taha, Sabbagh & Dorn, 2019). Pulsed current GTAW reduces the heat input into the weld pool that results in less distortion, weld bead size, residual stresses and porosity. (Farahani, Shamanian & Ashrafizadeh, 2012; Madhusudhan Reddy; Mohandas & Sambasiya Rao, 2005; Kim & Na, 1998)

Grain refining by pulsed current can be attributed to the decreased heat input that leads to faster cooling rates after welding. Furthermore, it was stated that the pulsed current influences the dendrite formation, where the pulsed current breaks off the dendrite tips to form nucleation sites for equiaxed grains to grow. The formation of dendrites is associated with higher degrees of segregation and cracking. The phenomenon of segregation and cracking is reduced due to the dendrites breaking off during pulsing (Farahani, Shamanian & Ashrafizadeh, 2012). Even though the main parameters influencing the amount of equiaxed grains were welding speed and heat input, the electrode tip angle could influence the shape of the weld pool and therefore the formation of equiaxed grains (Villaret, Deschaux-Beaume & Bordreuil, 2016; Ramkumar, Chandrasekhar, Singh, Ahuja, Agarwal, Arivazhagan & Rabel, 2015).

Abu-Aesh, Taha, Sabbagh and Dorn (2019) welded fully austenitic stainless steels, bead on plate, 3 mm thick, by means of pulsed current GTAW. They found that the weld metal contained an equiaxed structure at the centre of the weld that was surrounded by coarse columnar grains. It was also indicated that the pulse frequency had an influence on the amount of equiaxed grains that form in the weld microstructure. An increase in the pulse frequency influenced the shape of the weld pool and the amount of overlapping that occurred. These authors focussed on the grain size of equiaxed grains that formed, rather than the fraction of equiaxed grains in the weld metal. The authors did not have full penetration bead-on-plate welds and investigated individual pulsed puddles. The equiaxed grain band in the middle of the weld could be divided into two regions. A coarser grain region in the middle of the weld that is surrounded by finer equiaxed grains as indicated by Figure 12 (Abu-Aesh, Taha, Sabbagh & Dorn, 2019).

The grain size of the equiaxed grains in the center of the weld decreased from 210 µm to 120 µm as the pulse frequency was increased from 0.2 Hz to 50 Hz. These coarser equiaxed grains are due to higher temperatures in the middle of the weld pool and the decreased cooling rate. Further, as the pulse current increases, the size of equiaxed grains decreases due to the higher rate of cooling for lower frequencies. It should be noted that more overlapping due to higher frequencies, lowers the cooling rate and the grains will be coarser. The bands of columnar grains that form in stainless steel weld metal are expected to be the main structure that leads to crack propagation (Abu-Aesh, Taha, Sabbagh & Dorn, 2019).
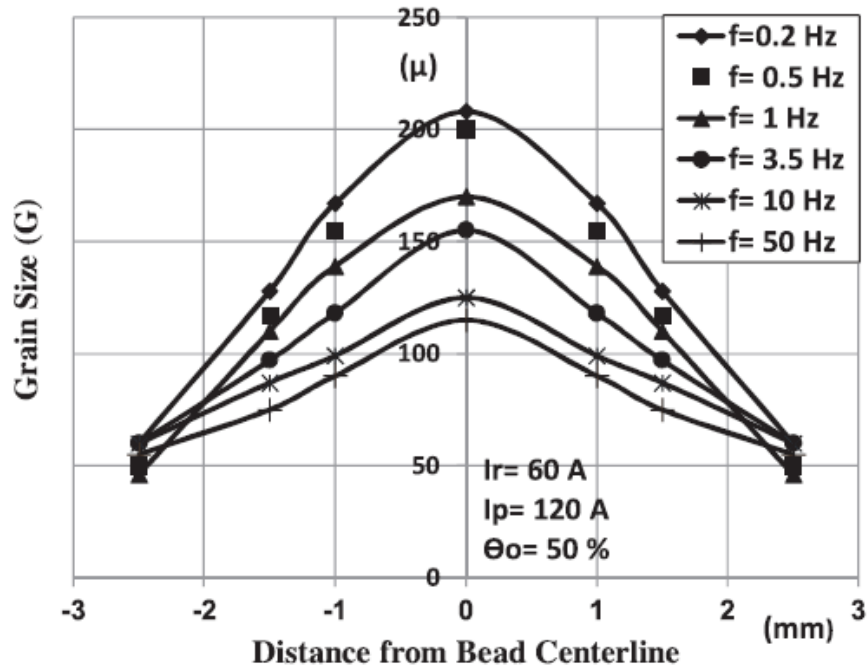
Figure 12: The average grain size of equiaxed grains in the weld center as a function of the pulse frequencies for GTA welds in 3 mm thick fully austenitic stainless steel. The peak-to-background current ratio was selected to be 2:1 (Abu-Aesh, Taha, Sabbagh & Dorn, 2019)

2.4 Practical welding of ferritic stainless steels

The ferritic stainless steel to be welded should be clean from any contamination and the base metal as well as the weld pool should be shielded from atmosphere. For the GTAW process, the electrode, weld pool, arc and material are shielded by means of a shielding gas. The gas is typically an inert gas or a mixture of inert gas where argon and argon-helium mixtures are usually employed in the industry. The shielding is provided to prevent atmospheric contamination of the weld pool. The composition of the shielding gas has an influence on the arc temperature and in certain conditions, it can affect the weld pool shape (Davis, 1993). The success of welding ferritic stainless steel is dependent on preventing carbon, nitrogen and oxygen contamination of the weld pool (Davis, 1993). A rule of thumb is that the width of the area to be cleaned before welding should be 1.5 times the thickness of the base metal. Due to the lack of fluxing during Gas Tungsten Arc Welding (GTAW) and Gas Metal Arc Welding (GMAW), special precautions for surface cleaning must be taken to prevent contamination. Carbon pickup can adversely affect the metallurgical properties and corrosion properties of stainless-steel welds. It is therefore important to use solvents to remove hydrocarbons from the surface of the stainless steel (Singh, 2012).

Arc welding is the most common welding technique to fuse ferritic stainless steels. Since ferritic stainless steel grades are mostly thinner gauges of material, the GTAW process is typically used for welding ferritic stainless steels since it provides the highest quality of welds. GTAW provides lower heat inputs, less distortion, better hot cracking resistance and better control over the fusion zone of the weldment that will improve the mechanical properties (Mallaiah, Kumar, Ravinder Reddy & Madhusudhan Reddy, 2012). Direct current electrode negative (DCEN) is the usual polarity (Davis, 1993).

For thin sections that require full penetration welding, backing gas is used to protect the bottom of the weld joint from oxidation (Davis, 1993). Filler metal is typically used with arc welding processes. The filler metals for ferritic grades are typically matching chemical compositions to allow a ferritic microstructure to form in the weld metal or austenitic stainless-steel filler metal to provide ductility and toughness to the weld metal or nickel-based filler metals. Matching ferritic filler metals are seldomly used due to the lack of toughness that results in the weld metal and HAZ. Austenitic stainless steel filler metals are preferred for their superior weld metal toughness, but compromise the application in chloride-containing environments that will cause stress corrosion cracking (SCC) (Davis, 1993).

Preheating can reduce the level of residual stresses. Since excessive grain growth occurs at high temperatures, it is recommended to use low preheating and interpass temperatures usually below 150°C. If it is deemed necessary for post-weld heat treatment (PWHT), a temperature range of 700-843°C is recommended followed by rapid cooling to 540°C to prevent embrittlement (Singh, 2012).

For the welding of thin gauge ferritic stainless steels, it is required to take necessary care to avoid distortion of the material during the welding process. This can include the use of clamps to keep the material flat during welding (Laksminarayanan, Shanmugam, & Balasubramanian, 2009). During the pulsed current GTAW process, the amount of heat input is controlled, and distortion of the welded joint is minimised (Baghel & Nagesh, 2016).

2.5 Statistical analysis of welding data

Engineering problems often involve the study and investigation of relationships between two or more variables. Regression analysis is a collection of statistical tools used to investigate the relationships between the variables (Montgomery & Runger, 2014). As newer welding machines allow more accurate capturing of the welding data, statistical analysis is useful in finding the relationships between different welding parameters and the final microstructure and mechanical properties.

Descriptive statistics are used where organizing and summarizing of data is required to improve the interpretation and the subsequent analysis of the data. Basic statistical terminology often includes (Montgomery & Runger, 2014):

- Sample mean: The average of all the observations made in the total set of data.
- Standard deviation: Indicates the variability or the scatter of the data.
- Median: a value that divides the data in two equal halves.
- Sample range: It indicates the difference between the maximum and the minimum value of the observations. The sample range is useful for determining the amount of variation that exists. As the amount of variability in a set of data increases, the sample range will increase.

The frequency distribution is a compact summary of the data. The data is divided in equal intervals to improve the visual information of the data. The frequency distribution is typically used to plot a histogram (Montgomery & Runger, 2014).

The most common form of data in industry is multivariate in nature. Scatter diagrams are a useful tool to illustrate a pair of observations between two variables. For data that consists of more than two variables, a matrix of scatter diagrams is useful to test pairs of variables against one another. Such a matrix of scatter diagrams is illustrated in Figure 13 where different welding defects during gas metal arc welding (GMAW) were tested for correlation between two welding defects. When considering the first row of diagrams in Figure 13, the porosity is evaluated against lack of penetration, spatter, undercut, lack of fusion and cracking. From Figure 13, a strong linear relationship can be seen between undercut and porosity, with the datapoints being in a narrower linear relationship. Further, there was no relationship between the porosity and cracking as

evidenced by the wide scatter. The matrix of scatter diagram gives a quick overview of the relationships (linear, quadratic polynomic etc.) that exist between dependent and independent variables.
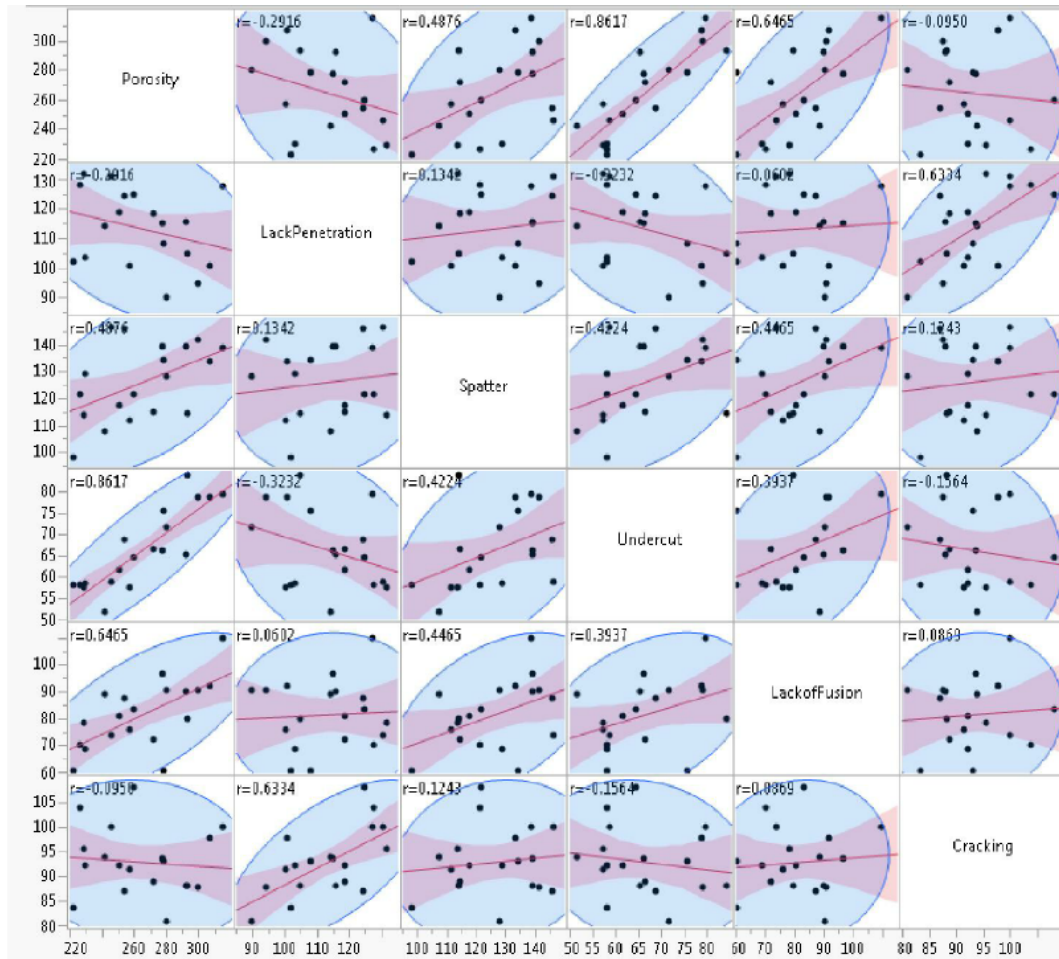
Figure 13: Matrix of scatter diagram with six GMAW defects tested against each other (Butte, 2014)

The analysis of variance (ANOVA) is used to test the significance of the regression model. The ANOVA method uses the basis of partitioning the variability in the dependent variable into meaningful components. The coefficient of determination (R^2) is used to judge how adequate the regression model is to the data. It is also used to indicate the amount of variability in the data that is explained for by the regression model. This means that for an R^2 equal to 0.887, 87.7% of variability in the data is explained by the regression model. The R^2 value will increase if another independent variable is added to the dataset, but will not necessarily prove that the new model will be superior to the previous model. If a high R^2 value is achieved, it will not

necessarily prove that the regression model will provide accurate predictions for future observations (Montgomery & Runger, 2014).

Multivariate statistical analysis methods, such as correlation coefficients, linear regression and covariance matrices can be used to monitor, analyse, model, predict, classify and control processing parameters and outcomes (Butte, 2014). During the development of the regression analysis models, it was assumed that the independent variable is to be a mathematical variable that was measured with a negligible error and that the dependent response was a random variable (Montgomery & Runger, 2014).

A simple linear regression model has only one independent variable and the equation typically includes an error term, as indicated in Equation 1 (Montgomery, Runger, 2014):

$$Y = \beta_0 + \beta_1 x + \varepsilon \qquad \textit{Equation 1}$$

Where β_0 and β_1 are the regression coefficients and ε the error term. The regression coefficients typically result in a line that is a best fit to match the data. The regression coefficients are determined by means of minimising the sum of the squares for the vertical deviations in the data (Montgomery & Runger, 2014).

The ρ-value in statistics indicates whether there is a significant linear, quadratic or cross-product relationship between the independent variables examined. The ρ-value is typically stated as a value between 0 and 1, where a value closer to 1 indicates no statistical linear significance and a value closer to 0 indicates a statistical linear significance. Statistical software packages, such as SAS Version 9.4, distinguish between significant and highly significant. A highly statistically significant fit of the data is indicated by a ρ-value of 0.0001 or a 99% level off significance (Jordaan, 2019).

The typical correlation coefficient tests used to identify correlations between independent and dependent variables are the Pearson and Spearman correlation coefficients. The Pearson correlation coefficient tests the data for linearity, while the Spearman correlation coefficient tests the data for a monotonic increase or decrease. The Pearson or Spearman correlation coefficients are an indication of how strong the fit of data is. The correlation coefficients are typically expressed as a value ranging between -1 and 1, where a value closer to -1 or 1 indicate a strong fit, while a value closer to 0 indicating a weak fit of the data (Jordaan, 2019).

From Equation 2: should $\rho = 0$, then β_1 will equal zero. This then implies that there is no regression of Y on X, i.e. the knowledge of independent variable X will not assist in predicting the independent variable Y (Montgomery & Runger, 2014).

$$\beta_1 = \frac{\sigma_y}{\sigma_x}\rho \qquad\qquad \textit{Equation 2}$$

Multiple regression analysis has a form as indicated by Equation 3, where more than one independent variable influences the dependent variable. For multiple regression analysis, β_1 and β_2 are known as the partial regression coefficients. This is due to β_1 measuring the expected change in Y for a change in x_1, while x_2 is held constant. β_2 measures the expected change in Y for a change in x_2, while keeping x_1 constant (Montgomery & Runger, 2014).

$$Y = \beta_0 + \beta_1 x_1 + \beta_2 x_2 \ldots \qquad\qquad \textit{Equation 3}$$

Response surface regression methodology uses the method of least squares by fitting linear and quadratic surface regression models to the data. Response surface regression is a general model which focusses on the characteristics of the response of the regression model and indicates the optimum response parameters. Response surface regression can also be used to test the lack of fit of the data, test individual parameters for significance, analyse the canonical structure of the response surface and predict new response values (SAS Institute Inc., 2013).

The t-test helps to understand if the differences between sample means are due to chance or are actually real. The t-test analyses whether the average values of two data sets or different data variables come from the same population. The following assumptions are made when applying the t-test:
1. The data should follow a continuous or ordinal scale.
2. Observations should be randomly selected in the data set.
3. The data should be normally distributed (Analytics Vidhya Content Team, 2019).

The t-test provides two output values, the t-value and the degrees of freedom. The t-value is compared to a value from the critical value table or T-distribution table. The T-distribution tables are typically calculated by statistical analysis software packages. The comparison of this t-value and the T-distribution table determines if the difference between two data set means are by chance or if there are important differences. A larger t-value indicates that the two data sets are different and a small t-value, closer to zero, indicates that the two data sets have more similarities. The degrees of freedom indicate the number of values that are free to vary in the data set or the number of independent information pieces that was used for the statistical calculation (Kenton, 2019).

2.6 Summary of findings from literature

The loss of ductility and toughness is the biggest industrial problem with the welding of ferritic stainless steel, which are susceptible to excessive grain growth at high temperatures (Lippold, 2015; Folkhard, 1987). During autogenous GTAW, epitaxial growth from an existing solid substrate is the main solidification mechanism (Villafuerte, Pardo & Kerr, 1990). Faster cooling rates tend to favour the formation of cellular solidification structures. The growth of the grains is determined by the direction with the highest heat dissipation (Lippold, 2015; Folkhard, 1987).

Weld pool stirring is important as it creates two half cycles during solidification: (1) the hot half cycle occurs near the fusion boundary where the temperature gradient (G) is high and the solidification rate (R) is low which will lead to more cellular structures, and (2) the cold half cycle where the solidification rate (R) is high and the temperature gradient (G) is low that will lead to more of a dendritic structure to form (Lippold, 2015; Villafuerte, Kerr & David, 1995).

Higher welding speeds lead to an increase in the solidification rate (R), but requires an increase in the welding current to maintain a full penetration weld, which will subsequently lead to a decrease in the temperature gradient (G). The simultaneous increase in the solidification rate and a decrease in the temperature gradient favours a transition from cellular structures to dendritic structures. These dendrites tend to break off due to temperature fluctuations and weld pool stirring (Villafuerte & Kerr, 1990, Villafuerte, Pardo & Kerr, 1990).

The columnar-to-equiaxed transition requires nuclei ahead of the advancing columnar growth and favourable thermal conditions. The surviving nuclei that can grow ahead of the columnar growth are the main reason for the columnar-to-equiaxed transition. The higher the number of nuclei, the higher the amount of equiaxed grains will be found in the microstructure (Jula, Dehmolaei & Alavi Zaree, 2018; Villafuerte, Kerr & David, 1995, Villafuerte & Kerr, 1990).

It was found that a higher titanium and aluminium content and faster welding speeds lead to smaller equiaxed grains in the weld metal of ferritic stainless steels. An increase in titanium content from 0.20% to 0.35% resulted in an increase of the amount of equiaxed grains by 20%. The amount of equiaxed grains also increased by 20% as the aluminium content was increased from 0.01% to 0.04% at 0.29% titanium. A higher titanium content resulted in a decrease in the size of the equiaxed grains in the weld metal microstructure

while the welding speed influences the amount of equiaxed grains present. Ferritic stainless steels that contain no titanium have fully columnar weld grain structures (Villafuerte, Pardo & Kerr, 1990). Titanium and aluminium precipitates were found to be present in the center of the equiaxed grains (Villafuerte, Kerr & David al., 1995).

The heat input during the welding of ferritic stainless steel needs to be low. One possibility to decrease the heat input is by using pulsed GTAW (David, Babu & Vitek, 2013; Madhusudhan Reddy; Mohandas & Sambasiya Rao, 2005). The use of a pulsed current can increase the ductility of the weld metal by 20%. A pulsed current also increases the convection and oscillation in the weld pool, which can effectively lead to dendrite fragmentation, which is typically stated to be the main mechanism of equiaxed grain formation (Kou, 2003).

Based on these findings, the need was identified to study whether the change in welding parameters, and the use of pulsed current, will transform the large columnar grains in the weld metal to smaller equiaxed grains. The experimental design to address these issues is set out in the next chapter.

CHAPTER 3: Experimental Procedure

3.1 Hypothesis

By changing the welding parameters of the welding process, it is possible to transform large columnar grains in the weld metal of Grade 441 and 436 ferritic stainless steels to smaller equiaxed grains that will lead to increased ductility of the weld metal.

3.2 Research Questions

- Will the use of pulsed current GTAW refine the weld metal microstructure of ferritic stainless steel as compared to constant current welding?
- Is it possible to increase the amount of equiaxed grains in the weld metal of Grades 441and 436, by changing the welding parameters such as current, welding speed and electrode tip angle?
- Will the ductility of the weld metal improve with an increase in equiaxed grains in the weld metal?

3.3 Outline of current study

A welding matrix was developed that incorporated the selected electrode tip angles, pulse frequency, welding speed and current that was used during the current study. The matrix formed the basis of which variables would provide the best possible outcomes and provided the extremes of welding Grade 441 and 436 ferritic stainless steel. It further helped in the selection of which parameters should be duplicated to validate authenticity of results. Table 3 indicates the different input parameters that were changed with their range and the objectives of the specific changes. The welding speeds and peak welding currents were selected on the basis of testing the extremes that will lead to full penetration welds and did not burn through during the welding process. The welding speeds were also selected based on industry specifications that require the welding of these grades of steel to be welded as fast as possible. The electrode tip angles were selected on acute angles where the arc energy was less focussed on the welding area, to less acute angles where the arc energy was more focussed on the welding area. The pulse frequencies were selected based on the peak welding currents and welding speeds, to allow full overlapping of each pulsed weld bead and allowing full penetration.

The electrode diameter or truncation of the electrode tip will also have an effect on the arc diameter and the consequential transfer of energy from the electrode tip to the workpiece and the heat flow in the molten weld pool. This flattening of the electrode tip improves the penetration, electrode life and prevents contamination (Diamond Ground products, 2013). The effect of changes in the electrode tip diameter was not considered as it adds to a higher number of variables to control and to a larger data set that would be required for statistical analysis. The electrode tip was kept sharp for all welds.

Table 3: Welding parameters that were used during experimentation and objective of changes (Abu-Aesh, Taha, Sabbagh & Dorn, 2019; Tong, Zhentai & Rui, 2013)

Parameter	Actual values used		Objective of change
	Grade 436	Grade 441	
Welding Speed (mm/s)	5, 8, 10	4, 5, 6.5, 8, 10, 12, 14	Welding speed would determine the penetration and heat input. Weld speed and pulse frequency would determine the amount of weld overlap.
Peak Current (A)	130, 140, 150, 160, 170, 180, 190	90, 100, 110, 120, 130, 140, 170	Peak current would determine the penetration and fusion of the workpieces. It would change the heat input into the system and determine the final microstructure.
Background Current (A)	56, 60, 64, 68, 72, 76	54, 60, 66, 72, 78, 84, 102	Background current would allow the arc to remain ignited and allow the weld pool to solidify, increase the cooling rate and alter the final microstructure.
Electrode Tip Angle (°)	30, 60	20, 30, 45, 60	The tip angle would affect the electron transfer from electrode to workpiece. It would determine the penetration, arc stability and influence the fusion line angle.
Pulse Frequency (Hz)	15, 25	15, 20, 25, 30	Pulse frequency would determine the overlap of each pulsed weld to ensure a fully fused weld. Pulse frequency would work interactively with weld speed and current.

Table 4 indicates the essential, supplementary-essential and non-essential requirements as stated by ASME Section IX that formed part of the successful welding of Grade 441 and 436 ferritic stainless steel.

Table 4(a): Documentation of all welding parameter essentials and supplementary essentials of the gas tungsten arc welding process as set out per ASME IX (The American Society of Mechanical Engineers, 2017)

Paragraph			Variables	Importance	Fixed/Varied during current study	Value used
QW-402 Joints	1	ø	Groove Design	Non-essential	Fixed	Square butt-weld
	5	+	Backing	Non-essential	Fixed	None
	10	ø	Root Spacing	Non-essential	Fixed	0 mm
	11	±	Retainers	Non-essential	Fixed	None
QW-403 Base Metal	5	ø	Group Number	Supplementary	Fixed	2
	6		T Limits	Supplementary	Fixed	1.2 mm
	8		T Qualified	Essential	Fixed	1.2 mm
	11	ø	P-No Qualified	Essential	Fixed	7
QW-404 Filler Metals	3	ø	Size	Non-essential	Fixed	No filler metal used
	4	ø	F-Number	Essential		
	5	ø	A-Number	Essential		
	12	ø	Classification	Supplementary		
	14	±	Filler	Essential		
	22	±	Consumable Insert	Non-essential		
	23	ø	Filler metal product form	Essential		
	30	ø	t	Essential		
	33	ø	Classification	Non-essential		
	50	±	Flux	Non-essential		
QW-405 Positions	1	+	Position	Non-essential	Fixed	Flat (butt-welds)
	2	ø	Position	Supplementary	Fixed	Flat (butt-welds)
	3	ø	Vertical Welding	Non-essential	Fixed	Not used
QW-406 Preheat	1		Decrease > 55°C	Essential	Fixed	Welded at ambient temperature
	3		Increase > 55°C	Supplementary		
QW-407 PWHT	1	ø	PWHT	Essential	Fixed	Not used
	2	ø	PWHT (T & T range)	Supplementary		
	4		T Limits	Essential		
QW-408 Gas	1	±	Trail or ø comp.	Non-essential	Fixed	Not used
	2	ø	Single, mixture or %	Essential	Fixed	Single (99.99% Ar)
	3	ø	Flow rate	Non-essential	Fixed	15 L/min
	5	±	or ø Backing flow	Non-essential	Fixed	15 L/min
	9	-	Backing or ø comp.	Essential	Fixed	Single (99.99% Ar)
	10	ø	Shielding or trailing	Essential	Fixed	Shielding constant

Table 4(a): Documentation of all welding parameter essentials and supplementary essentials of the gas tungsten arc welding process as set out per ASME IX (The American Society of Mechanical Engineers, 2017) (continued)

Paragraph			Variables	Importance	Fixed/Varied during current study	Value used
QW-409 Electrical Characteristics	1	>	Heat input	Supplementary	Varied	100-260 J/mm
	3	±	Pulsing I	Non-essential	Varied	15-30 Hz
	4	ø	Current or Polarity	Supplementary & Non-essential	Varied	56-170 A (DCEN)
	8	ø	I & E range	Non-essential	Varied	Pulsed parameters
	12	ø	Tungsten electrode	Non-essential	Fixed	2% Thoriated (2.4 mm)
QW-410 Technique	1	ø	String/Weave	Non-essential	Fixed	String
	3	ø	Orifice, cup or nozzle size	Non-essential	Fixed	#10 Cup
	5	ø	Method cleaning	Non-essential	Fixed	Industrial alcohol
	6	ø	Method back gouge	Non-essential	Fixed	Not used
	7	ø	Oscillation	Non-essential	Fixed	Not used
	9	ø	Multi to single pass/side	Supplementary & Non-essential	Fixed	Single one side
	10	ø	Single to multi electrodes	Supplementary & Non-essential	Fixed	Single
	11	ø	Closed to out chamber	Essential	Fixed	Not used
	15	ø	Electrode spacing	Non-essential	Fixed	Not used
	25	ø	Manual or automatic	Non-essential	Fixed	Mechanised
	26	±	Peening	Non-essential	Fixed	Not used
	64		Use of thermal processes	Essential	Fixed	Not used

3.4 Base metal
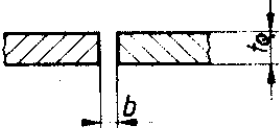
Sheet samples of Grade 441 and 436 ferritic stainless steel were received from Columbus Stainless (Pty) Ltd which had been cut from the same coil and slit. Grade 441 material had a thickness of 1.2 mm and Grade 436, 1.5 mm. The chemical compositions of the base materials as received are shown in Table 5, with the equivalent specified limits from BS EN 10088:1-2005 stated for comparison. The manufacturing production order numbers (MPO's) were 4199474 (for Grade 441) and 4212173 for (Grade 436).

Table 5: Chemical composition of Grade 441 and 436 as received from Columbus Stainless (Balance Fe). Values from EN 10088-1 indicate the maximum levels allowed

Element	Si	Mn	Ni	Cr	Mo	Ti	Nb	C	N	Al
Grade 436 Actual	0.39	0.41	0.29	17.38	0.82	0.002	0.38	0.01	0.02	0.004
Grade 436 EN 10088-1	1	1	-	18	1.4	-	1	0.08	0.04	-
Grade 441 Actual	0.51	0.37	0.22	17.56	0.08	0.18	0.41	0.01	0.01	0.02
Grade 441 EN 10088-1	1	1	-	18.5	-	0.6	1	0.03	-	-

The weld joint design is shown in Table 6. The weld joint was a square butt weld with no gap and a thickness of 1.2 mm for Grade 441 and 1.5 mm for Grade 436. A guillotine was used to cut these sample sheets into coupons, 30 mm wide by 150 mm long. Partially penetrated welds were not considered for weld characterisation. The joint design was shaped in such a way that full weld penetration and weld bead overlapping was achieved by autogenous GTAW. Before welding commenced, the sheets were wiped clean with industrial alcohol to clean off grease on the sheets and avoid any contamination (Ramkumar et al., 2015; Mallaiah, Kumar, Ravinder Reddy & Madhusudhan Reddy, 2012;).

Table 6: Weld joint design requirements as per EN 29692:1993. The table includes the specified value and values used for this study

Ref. No.	Designation	Cross section	Parameters to be specified	Values used during this study
1.2	Square butt weld		Gap (b) Thickness (t_0)	b = 0 mm t_0 – Grade 436 = 1.5 mm t_0 – Grade 441 = 1.2 mm

The welding was mechanised by means of a translation table moved by an alternating current (AC) motor and gearbox. The motor was controlled by means of an AC programmable controller. The linear moving speeds were then calibrated to the pre-determined welding speeds and corresponded to a certain frequency that was sent to the motor. The speeds were determined by means of a ruler and stopwatch as indicated in Table 7.

Table 7: Calibration results to determine the welding speed of the linear translation table. The welding speed was determined by measuring the time to cover 50 mm

Selected Speed	Time (seconds)						Calculated Speed (mm/s)
	1	2	3	4	5	Average	
4 mm/s	12.5	12.4	12.4	12.6	12.5	12.5	4.0
5 mm/s	9.8	9.8	10.1	9.9	9.8	9.9	5.1
6.5 mm/s	7.8	7.8	7.6	7.7	7.7	7.7	6.5
8 mm/s	6.5	6.4	6.2	6.3	6.3	6.3	7.9
10 mm/s	5.1	5.0	5.0	5.1	4.9	5.0	10.0
12 mm/s	4.2	4.2	4.3	4.3	4.3	4.2	11.8
14 mm/s	3.7	3.6	3.7	3.6	3.6	3.6	13.7

$y = 0.97x + 0.1764$
$R^2 = 0.9998$
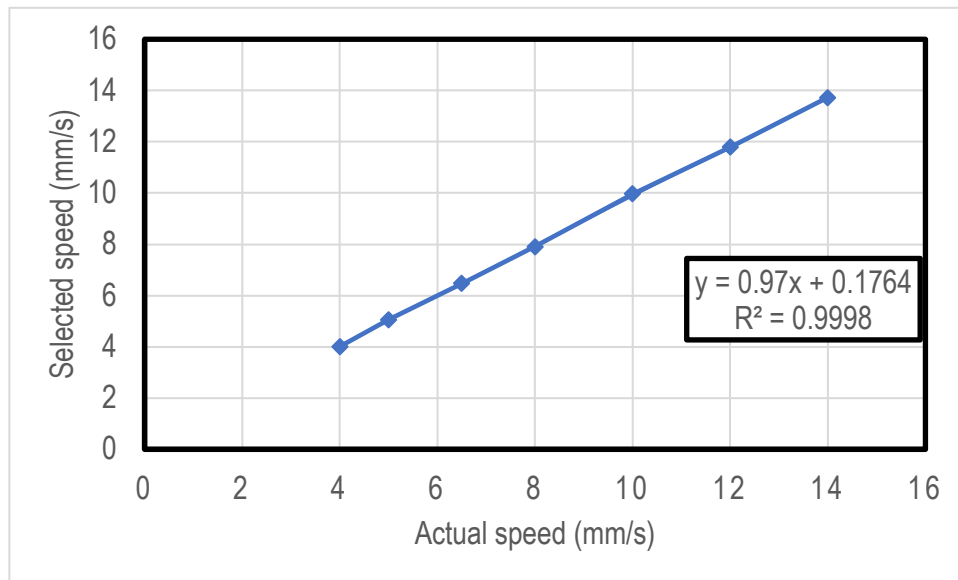
Figure 14: Actual versus selected welding speeds of the translation table illustrated in Figure 15

A welding jig was built that fitted onto the translation table to allow for back purging with industrial argon (99.99%) gas and to clamp the specimens down to avoid warping and keep the arc length constant. A laser

line was used to keep the welding constant over the square butt welds. The arrangement is shown in Figure 15.
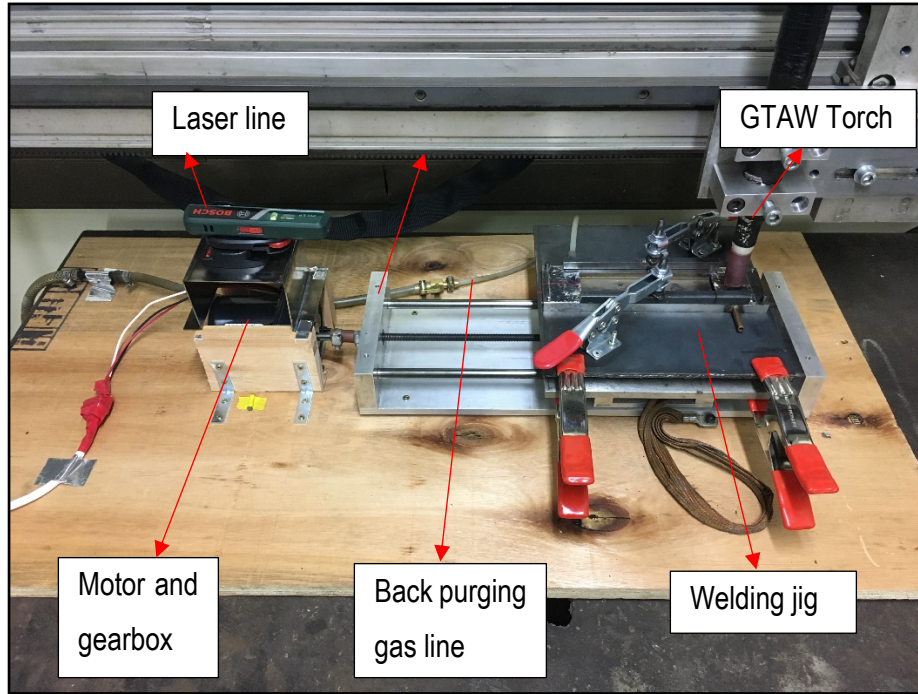
Figure 15: Weld setup used for experimentation, fully isolated from electrical interference and set up with a laser line for consistently accurate welds

The specimens (two 150 mm x 30 mm x 1.2 or 1.5 mm) were tack welded together at the edges to allow easy clamping into the welding jig and avoid distortion during welding. High frequency arc initiation was used to avoid contamination of the tungsten electrode. Due to the nature of the high frequency arc start, all electronic equipment (laptop computer and AC motor controller) was moved a distance away from the arc itself to prevent any interference and damage. The welding translation table, motor, gearbox and GTAW torch holder were all electrically isolated from one another and earthed. The electrode holder was water cooled by means of a Tweco TCV900 water cooler.

3.5 Heat input calculation

The heat input governs the cooling rate of the welded joint. For this investigation, it was important to understand how pulsed current power supplies influence the heat input and the weld metal microstructure. The conventional calculation of heat input is typically determined by the voltage, current and welding speed as indicated by Equation 4.

$$HI = \frac{\eta VI}{v}$$ *Equation 4*

Where: HI – heat input (typically measured in kJ/mm or J/mm)

η – the arc efficiency (it was 1 for this investigation)

V – voltage

I – peak welding current

v – welding speed (typically measured in mm/min or mm/s)

The conventional heat input equation (Equation 4) could however not be used as pulsed current has a square wave form. It is for this reason and the work done by Melfi and Daniel (2010), that the instantaneous power provided by the welding power supply, was used as a more accurate measure. The power provided by the welding machine is calculated by integrating over time, the instantaneous voltage and current as illustrated by Figure 16. The determination of the heat input by means of the power is shown in Equation 5, where:

$$HI = \frac{\eta E}{l}$$ *Equation 5*

E – instantaneous average energy provided by the welding machine

η – the arc efficiency (it was assumed to be 1 for this investigation)

l – weld bead length (measured in mm)

The arc efficiency assumed to be 1 for the current investigation was appropriate as the study focussed only on the GTAW process and not between different welding processes. Further, the ASME Section IX equation for determining the heat input of waveform welding processes was used as illustrated by Equation 5 which

omits the arc efficiency. The current study focussed on the welding parameter effects on the weld metal microstructure of two ferritic stainless steel grades, therefore, no cooling/heating rate equations such as the Rosenthal equations were analysed, which would require the arc efficiency to be included.

3.6 Electrode tip angle

The electrode tip angle was changed to ensure that all parameters were covered for the investigation of achieving high amounts of equiaxed grains in the microstructure. The 2% thoriated tungsten electrodes, 2.4 mm in diameter for Grade 441 and 3.2 mm diameter for Grade 436, were used and sharpened by a Piranha II Tungsten Grinder to ensure accurate angles. The electrode tip angle was changed to include very acute angled tungsten electrodes of 20° and 30°, an intermediate angle of 45° and a least acute angle of 60°. Previous studies revealed differences in electrode tip angles used, where 60° and 45° were typical (Villaret, Deschaux-Beaume & Bordreuil, 2016; Ramkumar et al., 2015).

3.7 GTAW Pulse parameters

Since the welding was mechanised, welding could be done with good accuracy at the different welding parameters. The peak welding current was varied between 90-190A. The peak current was set to values corresponding to the welding speeds that would introduce low heat inputs into the process, while maintaining full penetration welds as noted in Table 3. It was stated that a lower heat input leads to the development of equiaxed grains within the weld metals of ferritic stainless steels. This then further lead to increased mechanical properties (Amuda & Mridha, 2012).

Peak and background currents were defined in industry by means of a ratio and differs depending on the material used and what output was required. The industry ratios typically vary between 2:1 and 5:1 and should be selected to best suit the welding requirements. A peak welding current to background welding current ratio was selected as 1.67:1, i.e. with background current being 60% of the peak welding current.

The pulse frequency would determine the amount of overlap that would occur during welding and is typically expressed by means of a percentage, i.e. 75% overlap from pulse to pulse. The pulse frequency depends on the peak and background current time, as shown in Equation 6:

$$f = \frac{1}{t_B + t_P} \qquad \qquad \textit{Equation 6}$$

Where t_B refers to the time on background current, and t_P the peak current time in seconds. Different ratios of times between peak and background current can be selected, however for this investigation, the welding equipment was limited to a set 1:1 ratio (Omar & Lundin, 1979). The pulse frequencies used were 15, 20, 25 and 30 Hertz.

3.8 Weld Data

There are welding sources that can generate and control complex wave shapes. These include the use of pulsed current power sources. For recording weld data at high sample rates (typically 1 to 30 kHz), the welding current and voltage are still measured. These data sets kept in the welding machine are typically not available for data analysis due to the complex waveform algorithms used by welding machines to capture the data (Jooste, 2019).

The power source used in the current study (*Lincoln PowerWave S350*) could accurately record the arc energy and time. All welding data were captured by means of Lincoln Electric's Power Wave Manager software by using its *Weld View* function and capturing data at a frequency of 12 000 Hz. This arc energy that is provided by the welding machine is the instantaneous power measured by the welding algorithm at that specific time based on the frequency at which data is captured - Figure 16. This way of calculating the instantaneous power and energy provides the most accurate results. This method of heat input calculation does not include an arc efficiency constant (Melfi & Daniel, 2010). This energy was recorded for each weld bead and used in conjunction with the total length of the weld (Figure 17) to get to the average heat input for the specific weld in kilojoule per millimeter (kJ/mm) - Equation 5. The heat input was then converted from kilojoule per millimeter to joules per millimeter (Jooste, 2019).

For the calculation of heat input, it is important to look at how different codes allow it to be calculated. It is stated that it should be calculated by an input power rather than using the product of voltage and current as discussed in Equation 4 and Equation 5. Further, for welding machines that measure instantaneous welding current and voltage values, the correct energy (instantaneous power integrated over time) supplied by the

welding machine is achieved. The results provided by the welding machine (*Lincoln PowerWave S350*) were, therefore accurate (Jooste, 2019).
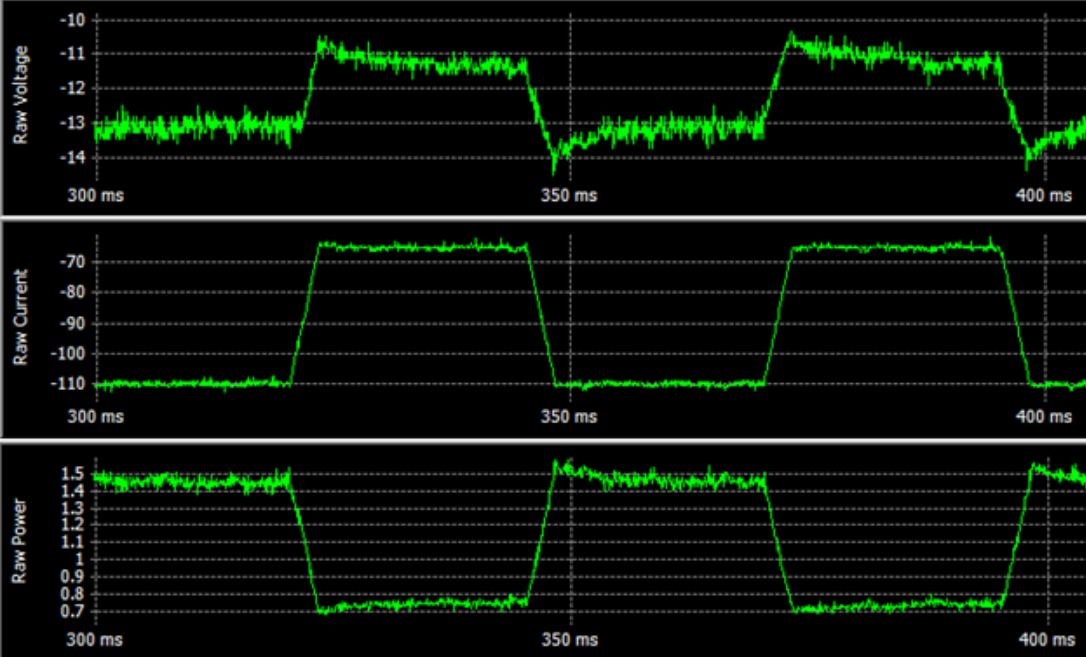
Figure 16: Pulsed current welding data recorded in the present study. Values were recorded as the negative by the power source for welding current and voltage (Weld ID: AB1108)

Figure 17: Illustration of the measurement for determining the length of the weld bead for both Grade 441 and 436. The figure indicates a Grade 441 weld completed with 120A, 8 mm/s, pulsed at 15Hz and an electrode tip angle of 20° (Weld ID: AA1208)

3.9 Characterisation of geometry and microstructure of the weld bead

In this study, only full penetration butt welds were considered, consistent with the requirements of industrial processes. The possibility of a completely different solidification structure exists between full and partial penetrated welds - Figure 1 and Figure 18.

The characterisation of the geometry of the weld bead is of importance. Figure 18 indicates a partial penetrated and full penetrated weld. It is evident that Figure 18 (a) will have weld metal grains growing from the base metal in horizontal and vertical directions, while Figure 18 (b) will only allow horizontal grain growth. Figure 19 indicates a partially penetrated weld as discussed in Figure 18. Here it was seen that the equiaxed grains were only observed in the top portion of the weld bead and not throughout the weld bead as in Figure 18 (b). The heat flow conditions for the partial penetration and full penetration welds in Figure 18 will differ. The partial penetrated weld will have 3-dimensional heat flow while a full penetration weld will have 2-dimensional heat flow Weld characterisation will help to understand what has occurred in the final microstructure, and subsequently the mechanical properties, when certain welding parameters are changed.

The geometry of the welds was examined to identify the effects of the weld bead shape on the solidification structure.
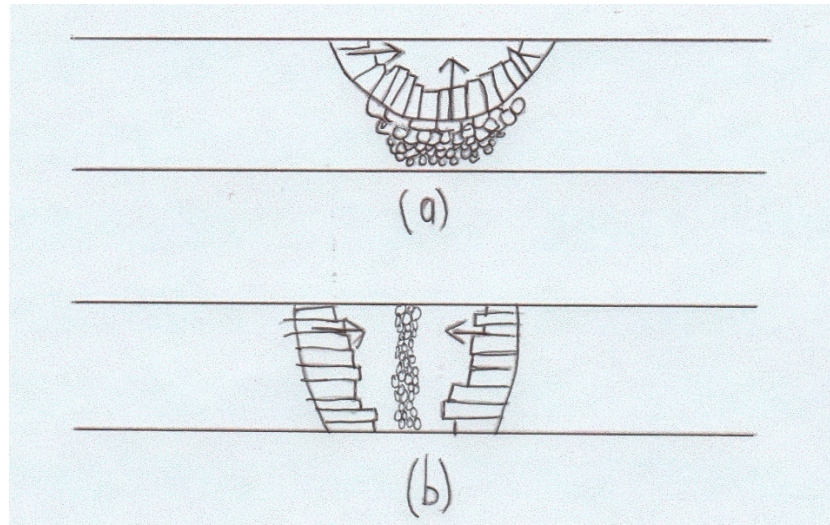
Figure 18: Characterisation of a partially penetrated and a fully penetrated butt weld: (a) will allow columnar grains to grow diagonally upwards with equiaxed grains mostly on the weld surface, (b) columnar grains will only grow in horizontal directions from the base metal with equiaxed grains through the entire weld thickness
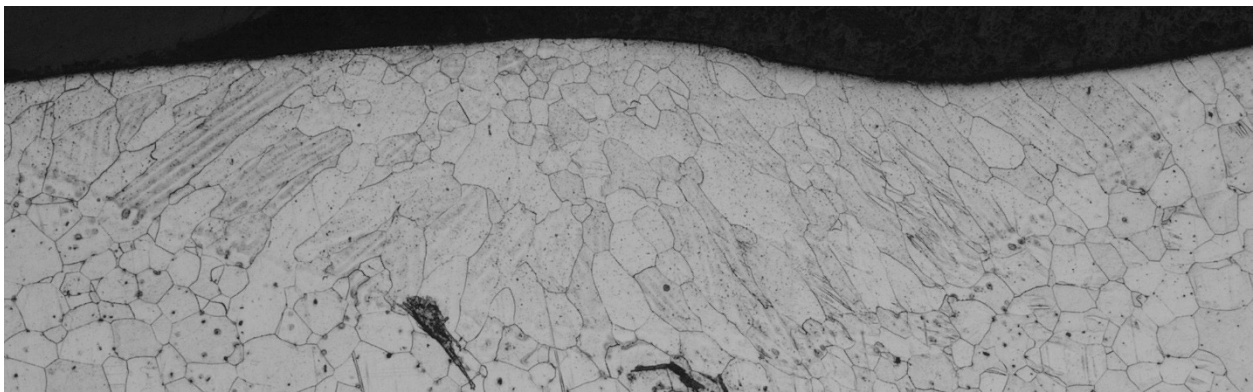
Figure 19: A partially penetrated butt-weld of Grade 441. The microstructure only exhibited equiaxed grains on the surface of the weld bead and not through the entire weld as noted in Figure 18 (Weld ID: BC908)

The weld top and bottom widths were measured for determination of the weld areas and could be used to determine the fusion line angle of the weld area - Figure 20.
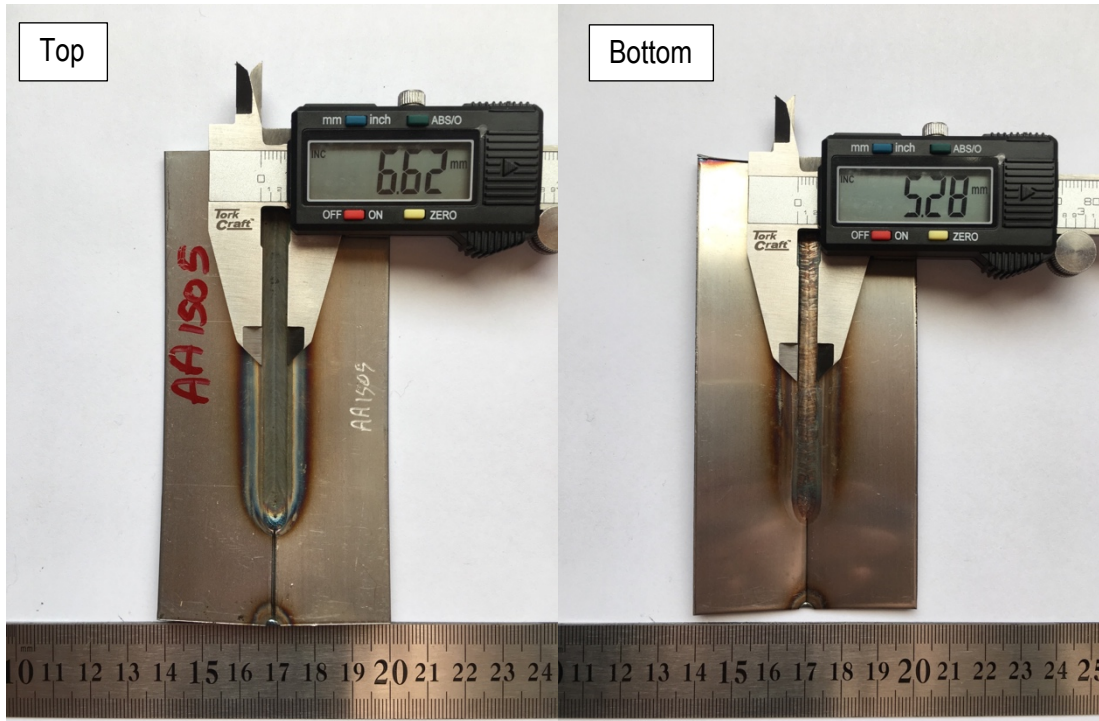
Figure 20: Illustration of the measurements of the top and bottom widths of the weld bead using a digital Vernier for both Grades 441 and 436. The figure illustrates a Grade 436 weld completed with 150A, 5 mm/s, pulsed at 15Hz and an electrode tip angle of 30° (Weld ID: AA1505)

Macroscopic analysis included the measuring the distance associated with a pulse by means of the welding speed and the pulse frequency. Figure 21 indicates how this distance was calculated.

Distance associated with a pulse
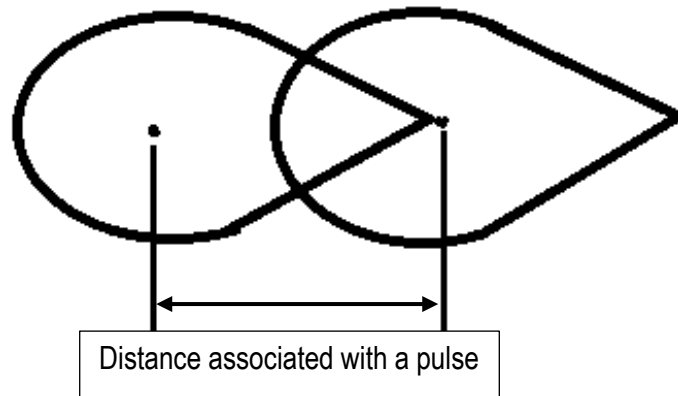
Figure 21: Definition of the distance associated with a pulse, calculated from the welding speed and pulse frequency

Microstructural analysis included the investigation on solidification effects that were determined by the different welding parameters, especially the welding speed and current. All weld metals were evaluated microstructurally. The samples had to be cut out into smaller sections. The ASM Handbook Volume 9, Figure 22, provides the different sectioning methods and the uses of these sections.

Normal section

Section parallel to the solidification front

Longitudinal section

Transverse section
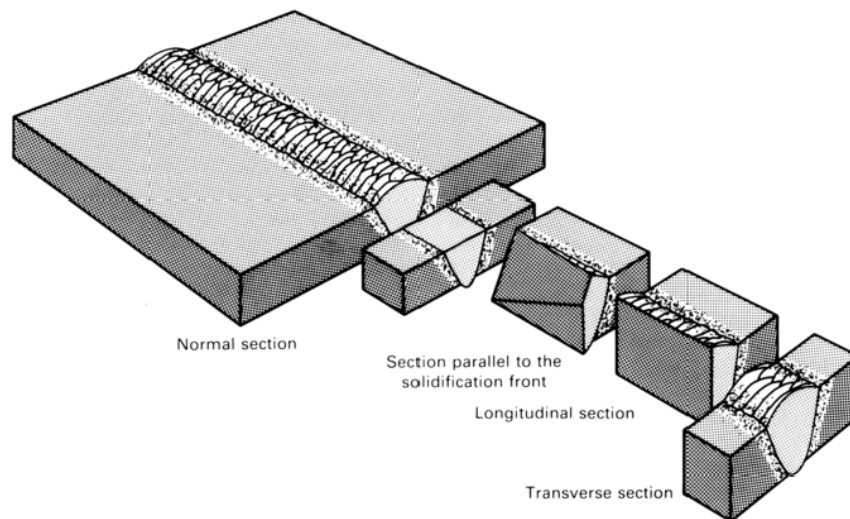
Figure 22: Different sectioning directions of a weldment that can help investigate different welding related problems (Davis, 1993)

For the investigation, a transverse section was done on all samples since it is the section that provides the bead geometry, the solidification structure, joint characterisation and whether any defects are present in the microstructure (Davis, 1993). Supplementary normal sectioned samples were also investigated for examining the solidification mode of the grains present in the weld metal. The cut sections were mounted in Bakelite. These mounted samples were then ground (180, 400, 600, 800 and 1200 grit) and polished to a 1-micron finish. For the etching of grain boundaries, Vilella's reagent consisting of 5 ml hydrochloric acid, 1g picric acid and 100 ml ethanol was used. Etching was done at room temperature (Davis, 1993). The samples were submerged during etching for 2 minutes. The welds were examined under a Zeiss AXIO Imager A1m microscope with a 0.63x magnification on the camera and a magnification of 2.5x, 5x or 10x on the objective lens. The fusion line angle was defined as the angle between the fusion boundary and the base metal surface as indicated in Figure 23. The columnar-to-equiaxed transition and the fusion boundary are included in red on Figure 23.
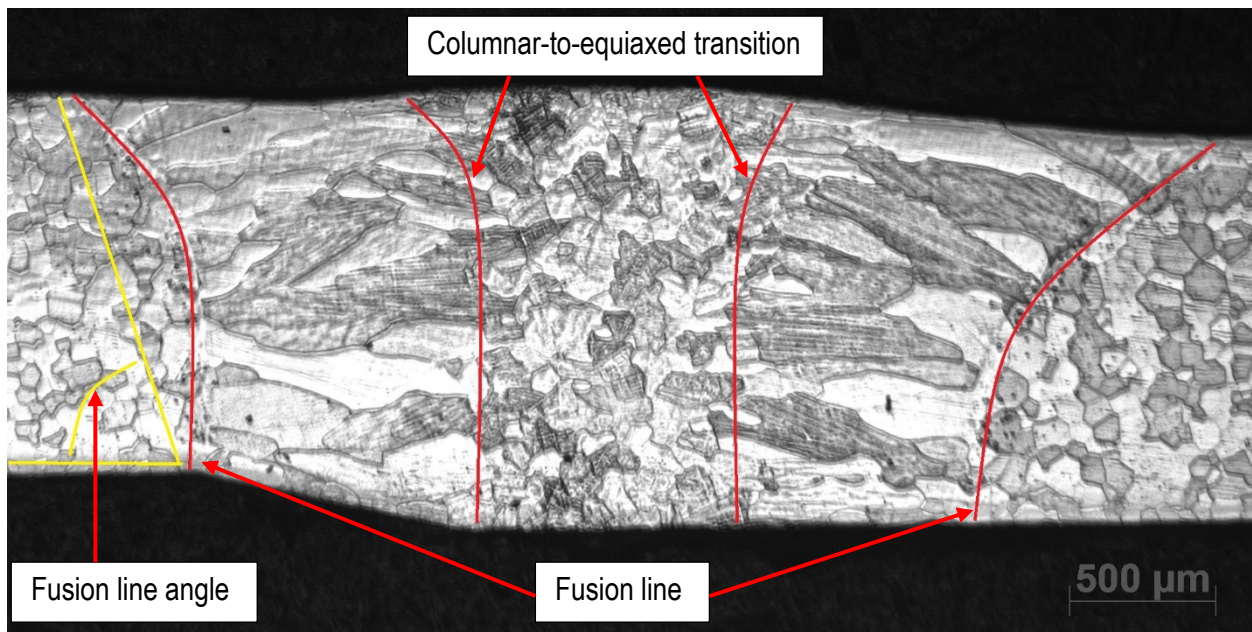
Figure 23: Fusion line angle determination of the welds indicated in yellow. The fusion line and the columnar-to-equiaxed transition is shown in red (Weld ID: DD13010, welded at 130A, 10 mm/s, electrode tip angle of 60° and a pulse frequency of 30Hz) (Magnification: 1.6x)

All welds of Grades 441 and 436 had a relatively flat weld bead top and some weld metal bowing at the bottoms of the welds. This was due to gravitational pull on the molten weld metal. Higher welding currents led to melt-through where the molten metal is pushed out the bottom of the plates (The James F. Lincoln Arc

Welding Foundation, 2000). The shape of the weld bead could also be determined by the thickness of the as received plates. The shape of the weld beads was not considered for the study and not influenced by the clamping of the individual samples.

3.9.1 Quantitative Metallography

Quantitative metallurgy was done by means of point counting, which is the simplest operation to examine areal features in the microstructures. A point grid was inserted on the micrograph using ImageJ software. The grid selected were 5000 pixels^2, the grids were centred on each micrograph and all points were spaced evenly apart. The total amount of points was then counted that fell on the weld area only. The total amount of points was therefore not constant for all samples due to the different weld sizes and weld geometries. The points were then counted that fell on the columnar- and equiaxed grains of the microstructure as indicated by Figure 24. Any points that fell on the grain boundaries were also considered to "fall" on columnar or equiaxed grains, depending on the area of the weld metal. The standard deviation and 95% confidence level were also calculated (Underwood, 1970).
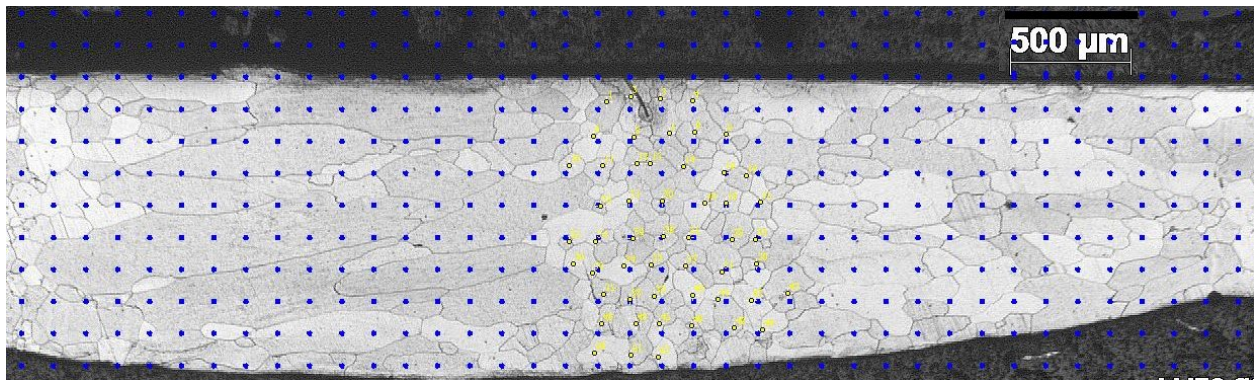
Figure 24: Illustration of the point counting method illustrated by the blue dots. The manual point counting of the equiaxed grains is illustrated by the yellow dots

The fraction equiaxed grains ($\sigma(x)$) was determined by Equation 7, where σ is the number of points that fell on the equiaxed grains and n the total number of points counted on the weld metal. The standard deviation of a sample mean should be obtained to further determine the 95% confidence level of the points counted on a microstructure. The standard deviation could be calculated by means of Equation 8 (Underwood, 1970):

$$\sigma(x) = \frac{\sigma}{n} \qquad \text{Equation 7}$$

$$\sigma(\bar{x}) = \frac{\sigma(x)}{\sqrt{n}}$$

Equation 8

Where $\sigma(\bar{x})$ is the standard deviation, $\sigma(x)$ is the fraction equiaxed grains and $\sqrt{n}$ is the total number of points counted to fall on the equiaxed grains for a given micrograph. To ensure certainty of the amount of points counted, a 95% confidence level could be determined to state that in this 95% confidence interval lies the true percentage of equiaxed grains determined. The smaller the interval and the closer it was to the determined value, the better the point counting method was for the individual micrograph (Underwood, 1970). The 95% confidence interval was determined as shown in Equation 9.

$$\mathbf{95\% \ Confidence \ Interval = 1.96\sigma(\bar{x})} \qquad \text{Equation 9}$$

A sample calculation of the standard deviation and 95% confidence level is shown in Table 8. This method was used for all full penetration welds. It should be noted that a weld process is not stable and the metallurgical results of the welding process is unknown. This was evident with repeated welds, where the same welding parameters gave different metallographic results, i.e. different amounts of equiaxed grains in Grade 441. The variation of weld process input parameters is yet to be investigated.

Table 8: Sample calculation of the 95% confidence interval for three different Grade 441 welds completed. The welds used have indicated low, average and high amounts of equiaxed grains respectively

Weld ID	Points on equiaxed structure σ	Total points on weld micro-structure (n)	Fraction equiaxed $\sigma(x)$ (%)	Standard deviation $\sigma(\bar{x})$	95% Confidence interval $1.96\sigma(\bar{x})$	Fraction equiaxed grain interval (%)
A11010CW	28	146	19	4	7	19±7
BB1205	234	493	48	3	6	48±6
BA1108	125	170	74	7	0.13	73±13

The average grain size of the equiaxed grains in Grade 441 weld metal and the columnar grain thickness in Grade 436 weld metal were determined by means of the line intercept method. The line intercept method requires a line being drawn on the weld microstructure and counting the number of grain boundaries crossed by the line. The line intercept method was also used to determine the average grain size of Grade 441 equiaxed grains at the centreline of the weld. Figure 25 illustrates the line intercept method on a fully columnar weld metal of Grade 436. The micrographs were all enlarged to focus on the weld metal areas and the distances calibrated in ImageJ software to allow accurate measurements of the grain sizes of the two grades of weld metals. For Grade 436 weld metal, the average columnar grain thickness was measured on both sides of the weld center (where the columnar grains meet, creating a linear plane). This was done to reduce the standard deviation of the measurement of the dimensions of the columnar gains. As Grade 436 had completely different weld metal microstructures from Grade 441, the high standard deviation was not of concern as direct comparison of weld metal microstructures were not possible.
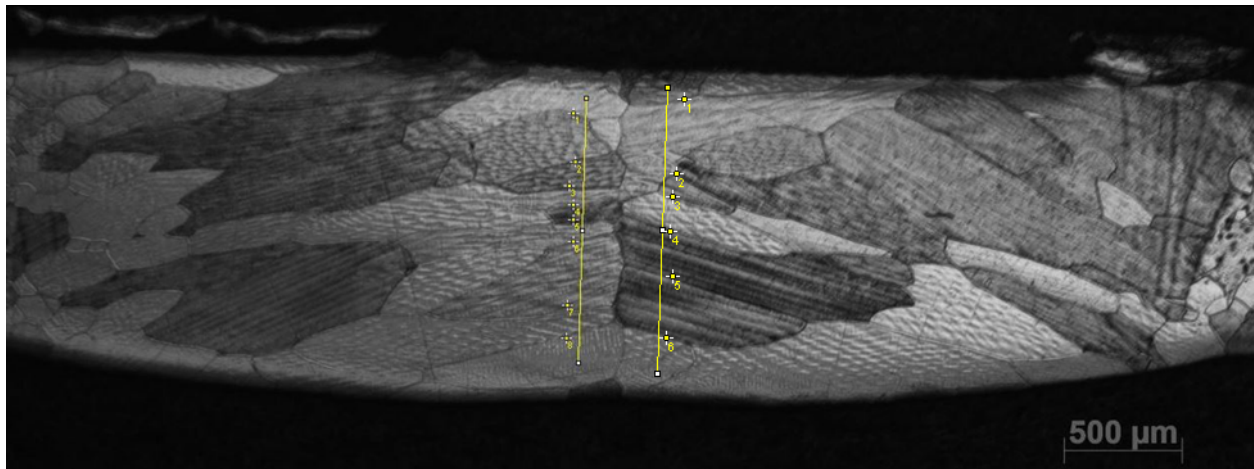
Figure 25: Illustration of the line intercept method used to determine the average grain size in the weld metal. This method was used for both Grade 436 and 441

Equation 7, Equation **8** and Equation 9 were used to determine the 95% confidence interval for determining the average dimension of columnar grain in the through thickness direction or columnar grain thickness of Grade 436 as defined in Figure 25. A sample calculation is included in Table 9.

Table 9: Sample calculation of the 95% confidence interval for three different Grade 436 welds completed. Welds were selected based on small, average and large columnar grain thicknesses.

Weld ID	Average line length σ (µm)	Average intercepts (n)	Average columnar grain thickness $\sigma(x)$ (µm)	Standard deviation $\sigma(\bar{x})$	95% Confidence interval $1.96\sigma(\bar{x})$	Average columnar grain thickness interval (µm)
AB1608	1456	11	132	3.47	6.80	132±7
AA1405	1377	7	212	5.71	11.19	212±11
BA1505	1412	5	282	7.52	14.73	282±15

3.10 Tensile Testing

The tensile specimens were cut longitudinally to the weld direction. This was done as transverse tensile tests are not suitable for determining the elongation, reduction in area or yield strength of the weld metal. This is due to the strain not being uniform in the gauge length during yielding (AWS Committee on B4 Committee on Mechanical Testing of Welds, 2016). The tensile specimens were cut parallel to the welding direction for analysing the elongation of the weld metal rather than the ultimate tensile strength of the welded joint.

The samples that were welded were sub-sized specimens and the mechanical properties were tested by means of tensile tests. For tensile tests, the welded samples were cut by means of CNC wire cutting. CNC wire cutting involves the process of spark erosion between an electrode, typically the wire and the workpiece. This process allows complex shapes to be cut and with small tolerances. ASTM E8 (2013) provided the specification to which the samples had to be cut. Figure 26 and Table 10 gives a graphical representation of the dimensions of the tensile test coupon.
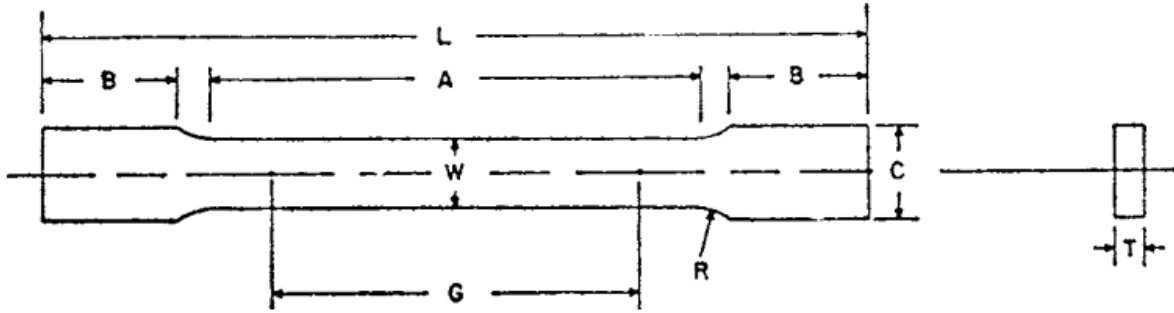
Figure 26: ASTM E8 standard to which dimensions the tensile test specimens were cut (ASTM E8, 2013)

Table 10: Dimensions to be used for Figure 26 according to ASTM E8 (ASTM E8, 2013)

	Dimension (mm)
G – Gauge length	25 ± 0.1
W – Width	6 ± 0.1
T – Thickness	1.2 or 1.5
R – Radius of fillet (min)	6
L – Overall Length (min)	100
A – Length of reduced section (min)	32
B – Length of grip section (min)	30
C – Width of grip section (approx.)	10

It should be noted that the coupon gauge width typically contained not only weld metal, but also some base material. The amount of base material present in the gauge width differed due to different welding parameters for each weld. Tensile specimens did not fracture completely, but the two parts of the coupon were typically still attached by the base metal present in the gauge width - Figure 27.
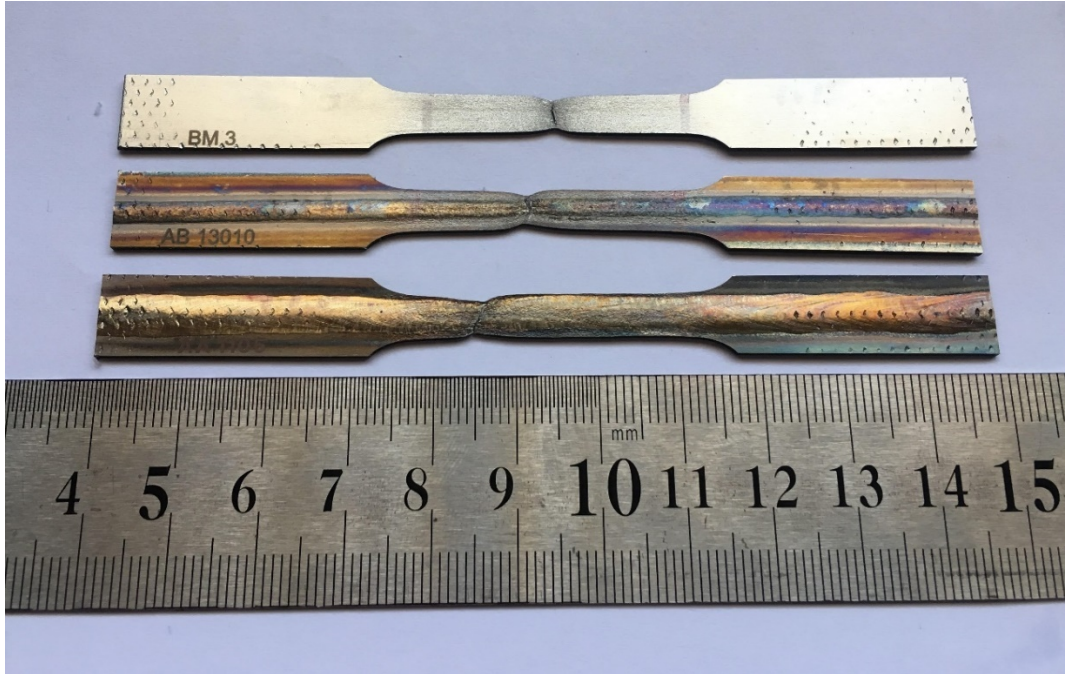
Figure 27: Tensile specimens still attached where base material is present in the gauge width of Grade 441. The top specimen (ID: BM3) indicates the Grade 441 base material, the middle specimen (ID: AB13010, welded at 130A, 10 mm/s welding speed, 20° electrode tip angle and 20Hz pulse frequency) illustrates a 50% weld metal in the gauge width and the bottom specimen indicates a 100% weld metal in the gauge width (ID: AA1105, welded at 110A, 5 mm/s welding speed, 20° electrode tip angle and 15Hz pulse frequency)

From Figure 28, it was expected that the weld metal should have a higher strength, but a lower ductility. For the current study where the weld metal was not necessarily the full gauge width wide, the tensile curve was expected to be between the 100% weld metal and 100% base metal.
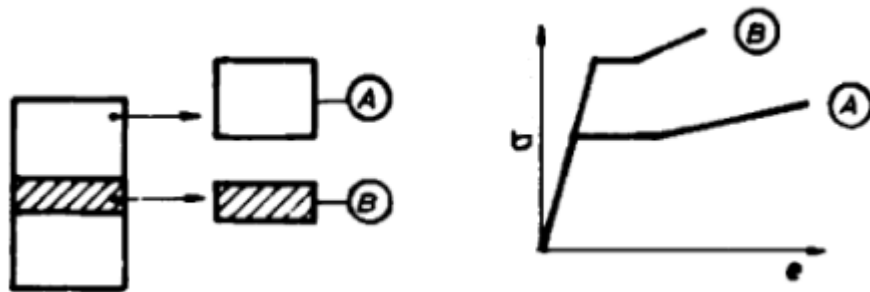
Figure 28: Illustration of the tensile properties of base material and weld metal separately (Denys, 1985)

3.11 Data analysis

Multiple regression analysis requires a host of datapoints. A rule of thumb for the minimum amount of datapoints required is five times the number of independent variables. This required the minimum set of datapoints for the current investigation to be 25 (Jordaan, 2019). The pulsed current welds for Grade 441 and 436 met the statistical requirements for analysis. Due to the small number of observations conducted with non-pulsed welds for both Grade 441 and 436, the constant current data sets could not be examined through statistical analysis. The data was analysed by means of SAS Version 9.4. The independent variable is the variable that is controlled or changed in an experiment to test the effects on dependent variables. The dependent variable is the variable that is tested or measured. The list of independent and dependent variables is shown in Table 11.

Table 11: Dependent and independent variables used for statistical analysis

Variable	Independent variable	Dependent variable
% Equiaxed grains		x
Grain size/ thickness (μm)		x
Fusion line angle (°)		x
Peak welding current (A)	x	
Electrode tip angle (°)	x	
Pulse frequency (Hz)	x	
Welding speed (mm/s)	x	
Heat input (J/mm)		x
Elongation (%)		x

The data was analysed with the following methods:

1. Descriptive statistics included the mean, standard deviation, median, maxima and minima.
2. Matrices of scatter diagrams of the welding variables were drawn up in Python for both Grade 441 and 436 pulsed current welds. The matrix of scatter plots gave a visual indication whether any relationships existed between any two welding variables.

3. Correlation coefficients. The correlation between welding variables were drawn up and tested by means of the t-test and a 0.05 level of significance. A Pearson correlation coefficient was firstly determined to test the data for linearity, while Spearman was used to test the data for correlations that were not linear. The data showed multicollinearity, which indicated that some independent variables were dependent on other independent variables. This was true for the heat input that is a function of the welding speed and welding current - Equation 4. This therefore confirmed that the heat input was a dependent variable.

4. The data was analysed by means of linear multiple regression models. The multiple linear regression model data was excluded as the results were incorporated by means of the final response surface regression (linear effects) results. The R^2 for the linear multiple regression model was very low (0.16) which indicated that the data might not be linear, as noted in Section 4.5.

5. Response surface regression was used to examine the best quadratic fit between welding parameters and the % equiaxed grains for Grade 441 and the grain size of Grade 436. The response surface contours were drawn up and conclusions could be made. The heat input that was calculated from the weld energy and the weld bead length, showed multicollinearity.

The number of observations for the pulsed and constant current welds are illustrated in Table 12. The different statistical analysis applied to the data sets are indicated by an x. As stated earlier, the constant current welds did not have the required minimum 25 datapoints for statistical analysis and those results were only used for comparison purposes. It is important to note that most statistical analysis conducted, assume that the final outcomes (in this case, the microstructural parameters) are precisely quantified. In this study, the microstructural parameters were estimated and not precisely known.

Table 12: Summary of the data analysis done on the dependent variables of pulsed and constant current welds of Grade 441 and 436

	Number of observations	Descriptive statistics	Correlation coefficients (Pearson and Spearman)	Response surface regression
Grade 441 Pulsed current	257	x	x	x
Grade 436 Pulsed current	24	x	x	x
Grade 441 Constant current	16	x		
Grade 436 Constant current	12	x		

CHAPTER 4: Metallurgical results

4.1 Structure of Grade 441 welded joints

In order to understand the solidification sequence for the welding of Grade 436 and 441 ferritic stainless steel, transverse sectioned microstructures were taken and examined as indicated by Figure 22. Figure 29 indicates the Grade 441 base material's microstructure in the as received condition. The typical grain size of Grade 441's base material was determined by the line intercept method to be 48 µm.
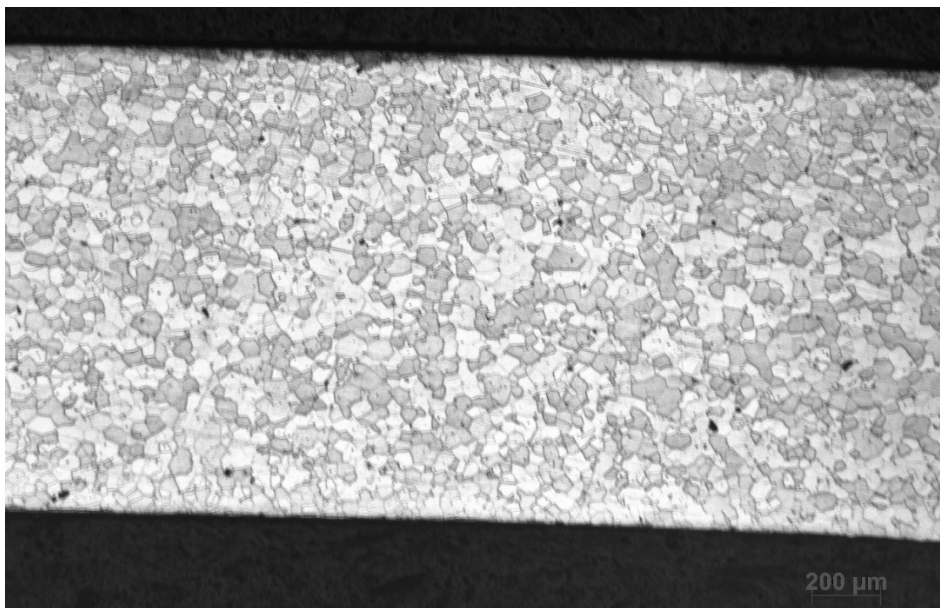
Figure 29: Transverse microstructure of 441-base material as received from Columbus Stainless (Pty) Ltd (Magnification: 50x)

Figure 30 and Figure 31 indicate microstructural differences for a faster welding speed and a slower welding speed, respectively. (All microstructures were oriented so that the top of the figure corresponded to the upper surface of the weld bead). The general trend for a faster welding speed (Figure 30), was that the percentage equiaxed grains increased and, for a slower welding speed (Figure 31) that the percentage of equiaxed grains were lower. However, the percentage equiaxed grains decreased as even faster welding speeds (typically 14 mm/s) were used. The comparison between fast and slow welding speeds were done as Villafuerte, Pardo and Kerr (1990) stated that the fraction of equiaxed grains was determined by the welding speed. This was found to be true for welding speeds up to 10 mm/s, but not for faster welding speeds. Further, Villafuerte and

Kerr (1990) stated that the temperature gradient (G) would decrease as the welding speed increases, with a corresponding change in peak welding current. Since the peak welding current was kept constant for these welds in Figure 30 and Figure 31, the temperature gradient (G) did not decrease and lead to columnar grains to form preferentially – as explained in Figure 8.
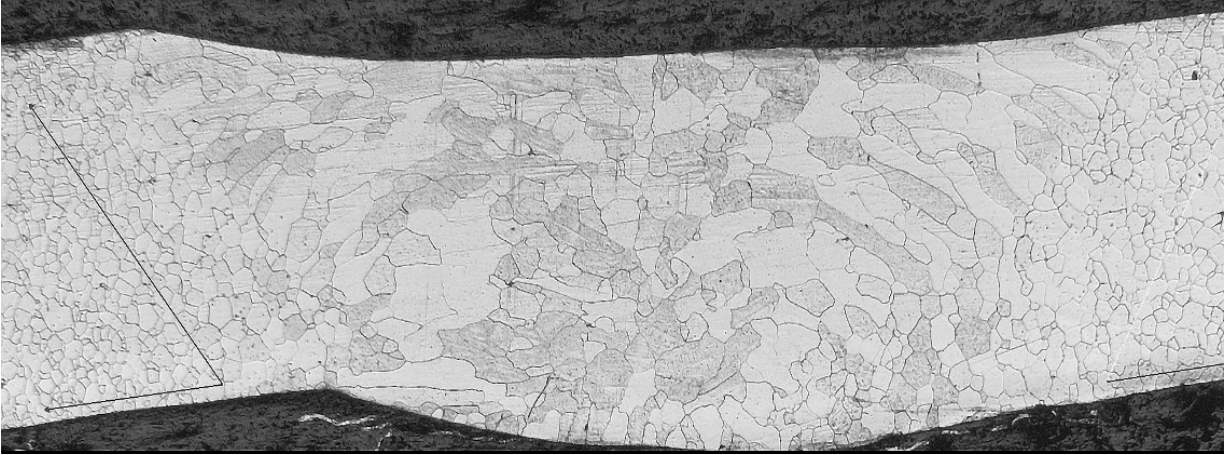
Figure 30: Transverse microstructure of the pulsed welded Grade 441 with a faster welding speed with a determined 58% equiaxed grains (Weld ID: BA11010, welded at 110A, 10 mm/s, heat input of 112 J/mm, electrode tip angle of 30° and a pulse frequency of 15Hz) (Magnification: 25x)
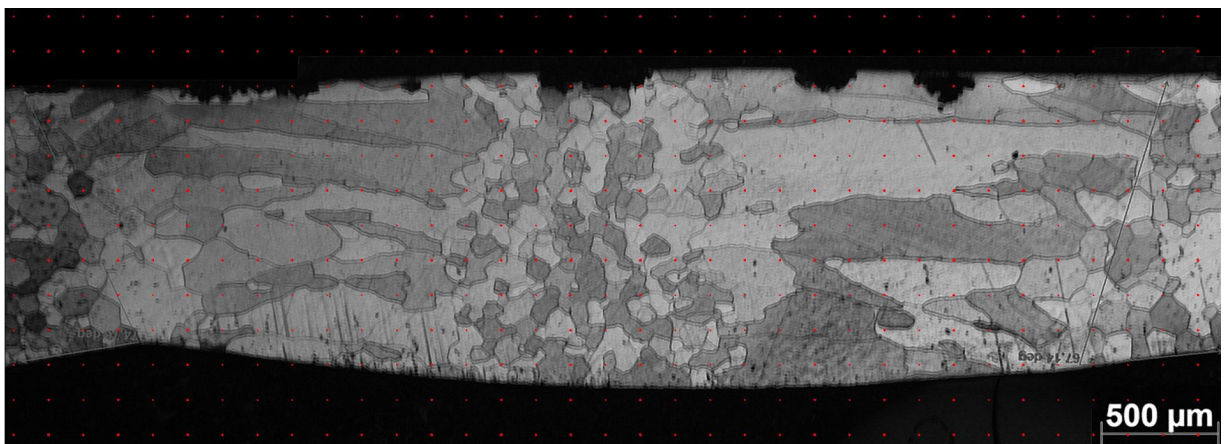
Figure 31: Transverse microstructure of the pulsed current welded Grade 441 with a slower welding speed with a determined 44% equiaxed grains (Weld ID: AA1005, welded at 100A, 5 mm/s, heat input of 195 J/mm, electrode tip angle of 20° and a pulse frequency of 15Hz) (Magnification: 25x)

Figure 32 and Figure 33 indicate the differences in microstructural characteristics between pulsed current welds and constant current welds with similar heat inputs. The point counting results indicated that all pulsed

current welds (Figure 32) had higher percentages of equiaxed grains as compared to the constant current welds (Figure 33). This was expected as pulsed current was considered to be a mechanism for grain refinement by breaking off dendrite fragments in the weld pool (Farahani, Shamanian & Ashrafizadeh, 2012).
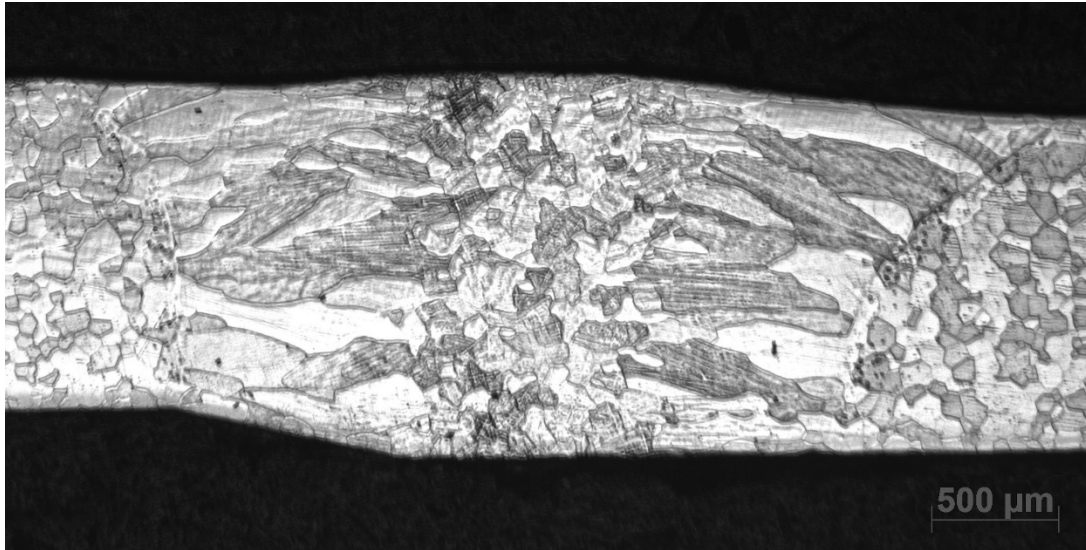
Figure 32: Transverse microstructure of a pulsed current weld of Grade 441 with a determined 59% equiaxed grains in the weld bead grains (Weld ID: DD13010, welded at 130A, 10 mm/s, heat input of 139 J/mm, electrode tip angle of 60° and a pulse frequency of 30Hz) (Magnification: 25x)
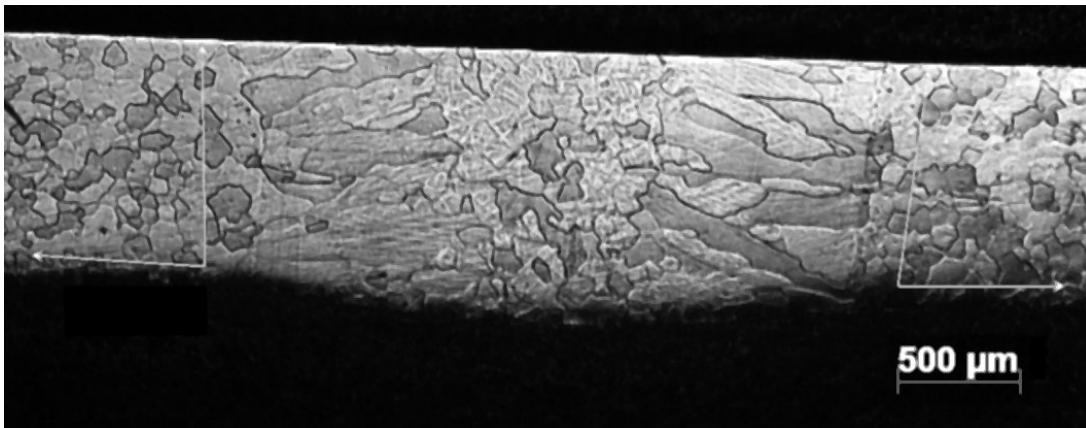
Figure 33: Transverse microstructure of a constant current weld of Grade 441 with a determined equiaxed grain amount of 34% in the weld bead (Weld ID: B11010CW, welded at 110A, 10 mm/s, heat input of 136 J/mm, electrode tip angle of 30 and the use of constant current) (Magnification: 25x)

Figure 34 illustrates the longitudinal cross section of Grade 441 weld metal, normal to the weld direction. The section was taken in the weld center to illustrate that the grains in the weld center were equiaxed grains

formed by heterogeneous nucleation and not columnar grains bending. Clear form the figure is the equiaxed grain structure as witnessed in Figure 36.
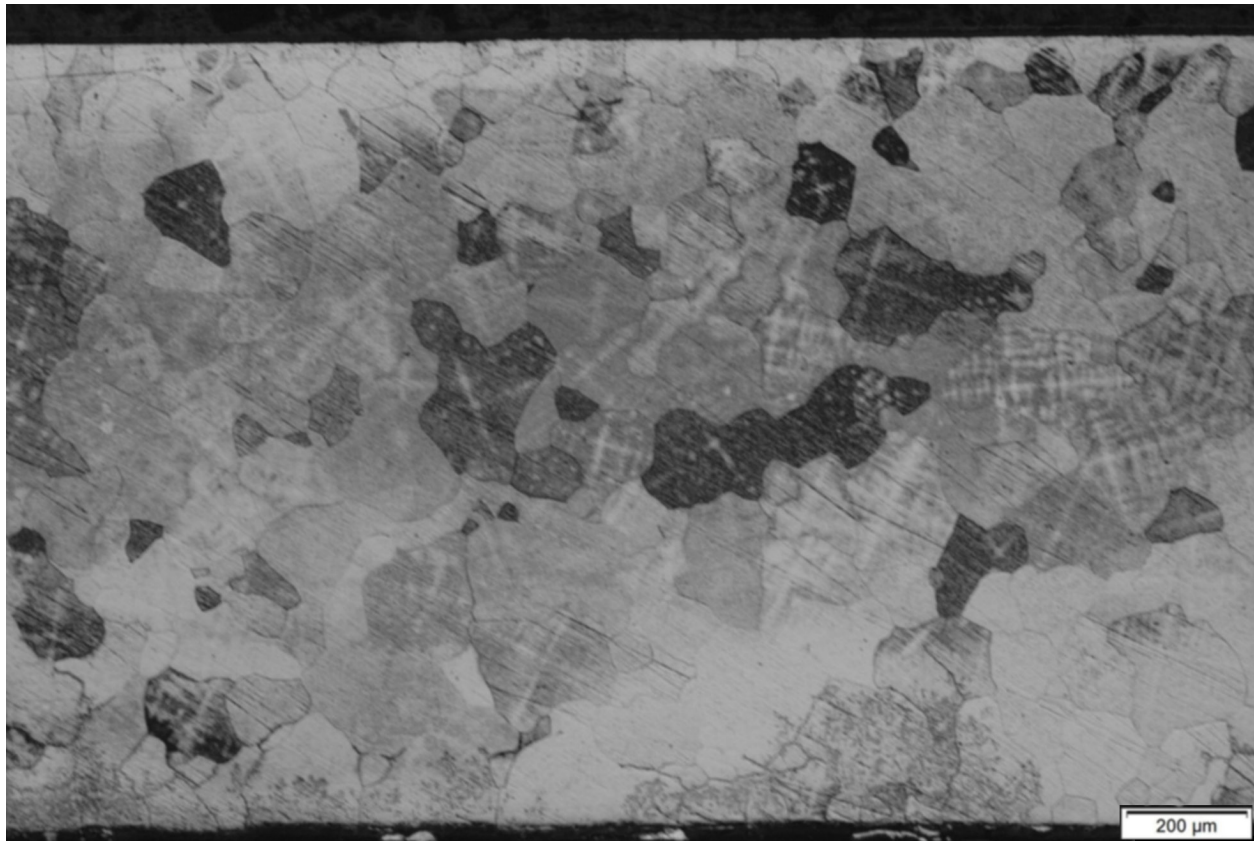
Figure 34: Longitudinal section of equiaxed grains in Grade 441 weld metal. The micrograph was sectioned parallel to the weld direction in the weld center. (Weld ID: BB1108, welded at 110A, 8 mm/s, heat input of 148 J/mm, electrode tip angle of 30° and a pulse frequency of 20Hz) (Magnification: 50x)

It was of importance to understand the solidification structure that occurred after welding was completed. To determine the solidification structure, representative samples from Grade 441 welds were electropolished with A3 electrolyte solution to enhance the solidification structures. The A3 electrolyte solution had a composition of 75% methanol and 25% 2-butoxyethanol, before etching with Villela's reagent. Figure 35 indicates a normal section of the equiaxed solidification structure usually observed in the smaller central grains in the welds of Grade 441 ferritic stainless steel. This fine structure was observed in the center of the welds of Grade 441 where equiaxed grains were present, which was similar to Lippold's (2015) observations

- Figure 36. The equiaxed structure grew equiaxially in all directions under the correct solidification parameters: low temperature gradient (G) and high solidification rate (R), as noted in Figure 7.
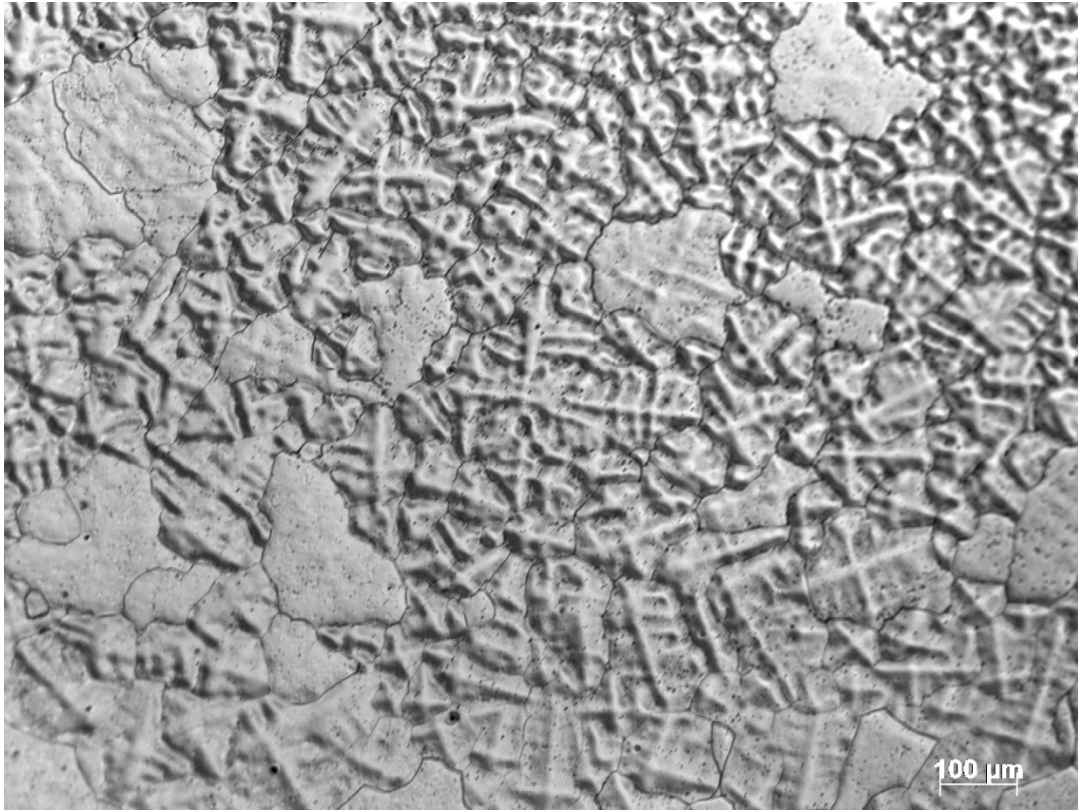
Figure 35: Equiaxed solidification structure present in the equiaxed grains of Grade 441 welds, examined by optical microscopy. The plane of polish was parallel to the plate surface, defined as a normal section in Figure 22. These structures start from a central point and grow equiaxially in all directions until it meets an adjacent grain that limits the growth due to orientation preferences. The weld was electropolished with A3 solution and etched with Villela's reagent (Magnification: 100x).

Equiaxed dendrite
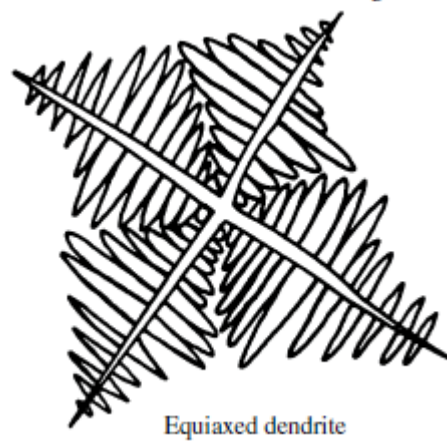
Figure 36: Expected solidification structure of an equiaxed grain (Lippold, 2015)

Figure 37 illustrates the columnar and equiaxed solidification structures of a normal sectioned weld bead observed in Grade 441. The columnar grains exhibited the cellular solidification structure, consistent with a high cooling rate as discussed by Figure 5.

Figure 37: Solidification structures visible by optical microscopy. The plane of polish was parallel to the plate surface, defined as a normal section in Figure 22. At the top of the figure, the cellular mode of solidification is present in the larger columnar grains of Grade 441. At the bottom of the figure, the small equiaxed mode of solidification can be seen in the smaller equiaxed grains. The weld was electropolished with A3 solution and etched with Villela's reagent. The welding direction is indicated by the yellow arrow in the top left corner and the columnar-to-equiaxed transition (CET) was indicated with an orange line (Magnification: 50x).

As discussed in previous work (van Niekerk, du Toit & Erwee, 2012), TiN will nucleate before solidification starts in Grade 441. The TiN precipitates have been found to be distributed throughout the weld metal of Grade 441 as indicated by Figure 38. The left figure in Figure 38 indicates the cuboidal TiN precipitate found on a grain boundary of equiaxed grains with its chemical composition indicated by SEM-EDS in Table 13.

The right figure in Figure 38 indicates the same cuboidal precipitate that was found in the columnar grains of Grade 441 weld metal. Again, clear from the chemical composition in Table 13, the precipitate was a TiN precipitate. These precipitates were found throughout the weld metals of Grade 441, regardless of pulsed current, constant current or different welding parameters. It was clear from the SEM micrograph that the particles in question were in fact TiN, as the particles were cuboidal, a distinct identification of TiN. The SEM-

EDS analysis indicated different chemical compositions for similar particles. This was mainly due to the electrons bombarding right through these particles and thicknesses of these particles were unknown. The results were used to confirm the TiN particles spread throughout the weld metal.
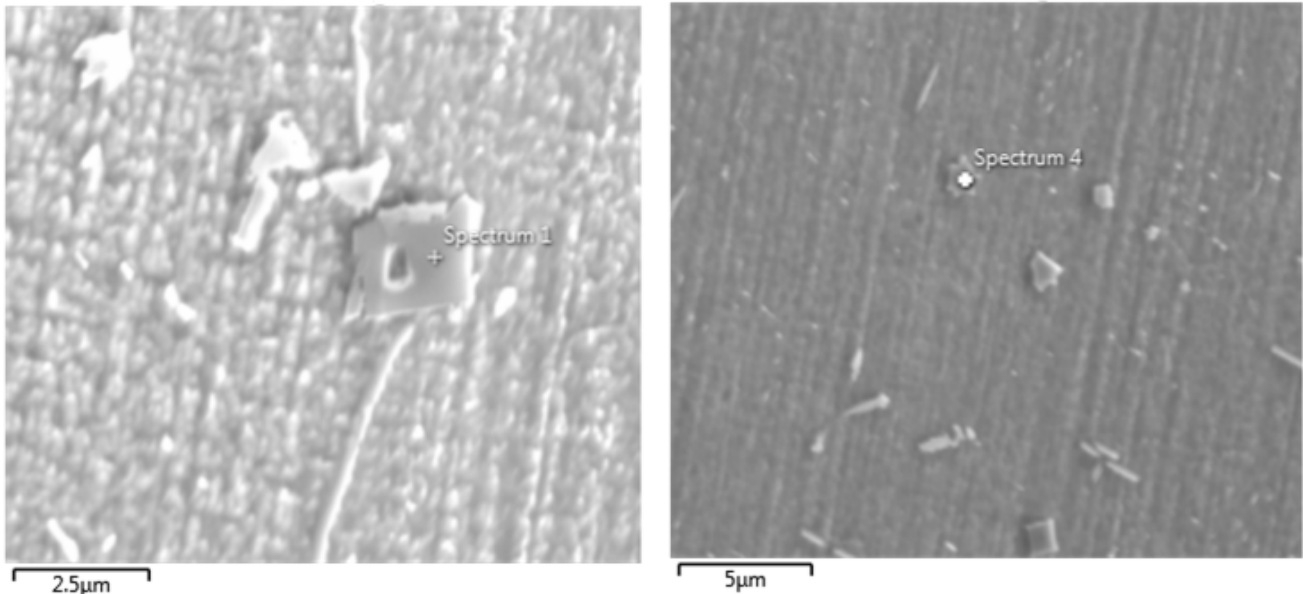
Figure 38: SEM-EDS micrograph of TiN square precipitates found distributed throughout the weld matrix of Grade 441. The left figure illustrates the TiN precipitate on the equiaxed grain boundary. The right figure illustrates the TiN precipitate in the columnar grains. (Weld ID: BD1108, where the electrode tip angle was 30°, the pulse frequency 30Hz, the peak welding current 110A and the welding speed 8 mm/s)

Table 13: The chemical composition ranges of the square precipitate visible in Figure 38 for equiaxed grains and columnar grains, as determined using SEM-EDS.

Element	Weight percentage (%) range in equiaxed grains	Weight percentage (%) range in columnar grains
Fe	14 - 16	24 - 37
Cr	4 - 7	8 - 11
Ti	30 - 42	26 - 41
Nb	5 - 26	4 - 6
N	6 - 17	10 - 14
O	3 - 5	4 - 9
V	0.2 - 0.5	0.4 - 0.5
Al	0.04 - 0.3	0.2 - 5

Since the welding data of percentage equiaxed grains versus the independent welding parameters indicated a larger variance for Grade 441, two repeatability tests were conducted on two subsets of welding parameters. These sets included 10 separate welding joints, with the welding parameters kept constant. The two sets of welding parameters were selected based on the initial welds having 50% and 70% equiaxed grains respectively in the weld metal. The individual results are set out in Table 14 and Table 15, with the variability also shown. A large difference in equiaxed grain percentage for the same welding parameters was observed, between 10 and 20 percent for the two subsets of welding parameters.

Table 14: Repeatability test of weld with 70% equiaxed grains and observed 10% difference in equiaxed grains (Weld ID: BB1108, welded at 110A, 8 mm/s, average heat input of 143 J/mm, electrode tip angle of 30° and 20Hz pulse frequency) Weld parameters were kept constant for each weld and welded ten times to indicate variation in % equiaxed grains in Grade 441 weld metal

Observation	% Equiaxed grains	Standard deviation (%)	Minimum (%)	Maximum (%)	95% Confidence interval (%)
1	65	9	47	83	65±9
2	64	6	52	76	65±6
3	64	9	47	81	65±9
4	61	9	44	78	61±9
5	68	10	49	86	68±10
6	59	8	43	75	59±8
7	57	8	42	73	57±8
8	59	7	45	74	59±7
9	64	9	45	82	64±9
10	60	12	36	83	60±12
Average	62	8	45	79	62±8

Table 15: Repeatability test of weld with 50% equiaxed grains and observed 20% difference in equiaxed grains (Weld ID: CA1105, welded at 110A, 5 mm/s, average heat input of 200 J/mm, electrode tip angle of 45° and 15Hz pulse frequency) Weld parameters were kept constant for each weld and welded ten times to indicate variation in % equiaxed grains in Grade 441 weld metal

Observation	% Equiaxed grains	Standard deviation (%)	Minimum (%)	Maximum (%)	95% Confidence interval (%)
1	48	4	44	52	48±4
2	48	4	44	52	48±4
3	48	4	44	51	48±4
4	48	5	43	52	48±5
5	48	4	44	52	48±4
6	38	9	29	46	38±9
7	50	9	41	59	50±9
8	43	9	34	52	43±9
9	43	9	34	52	43±9
10	30	8	22	39	30±8
Average	44	7	38	51	44±7

The highest % equiaxed grains for Grade 441 welds were found at lower heat inputs as illustrated by Figure 39, where equiaxed grains higher than 60% were found at heat inputs lower than 150 J/mm. It is clear from the figure that the variation was high and that the pulsed current and constant current overlapped over a large range. The average percentage equiaxed grains were higher for pulsed current welds as compared to constant current welds.
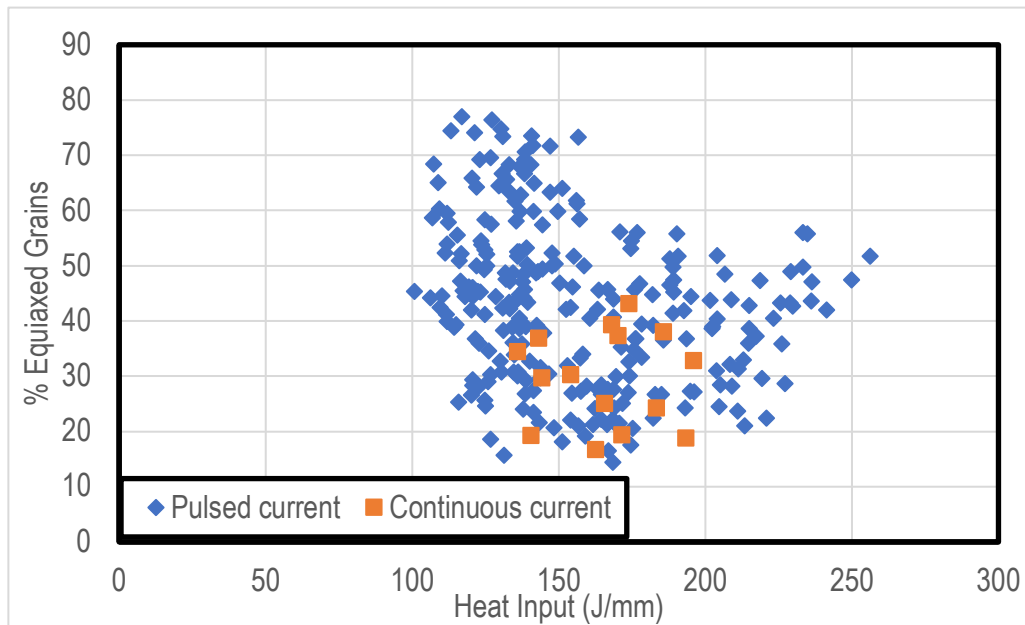
Figure 39: Percentage of equiaxed grains that formed in the weld metal of Grade 441 as a function of the heat input

Figure 40 shows the effects of the heat input on the grain size of Grade 441 for pulsed and constant currents. The grain size of Grade 441 does not seem to be influenced by the welding parameters, specifically the heat input as determined by the welding speed and peak welding current. Figure 41 indicates the effects of pulsed current as compared to constant current welds. The datapoints were selected where one datapoint of the constant current and one of pulsed current welds had similar welding speeds, peak welding currents and electrode tip angles. It is clear from the figure that the pulsed current doubles, for some cases, the amount of equiaxed grains that form in the weld metal. The heat input was reduced by using pulsed current as compared to constant current welding. This reduction in heat input due to the use of pulsing was consistent with previously published work (Abu-Aesh, Taha, El-Sabbagh & Dorn, 2019; David, Babu & Vitek, 2003).
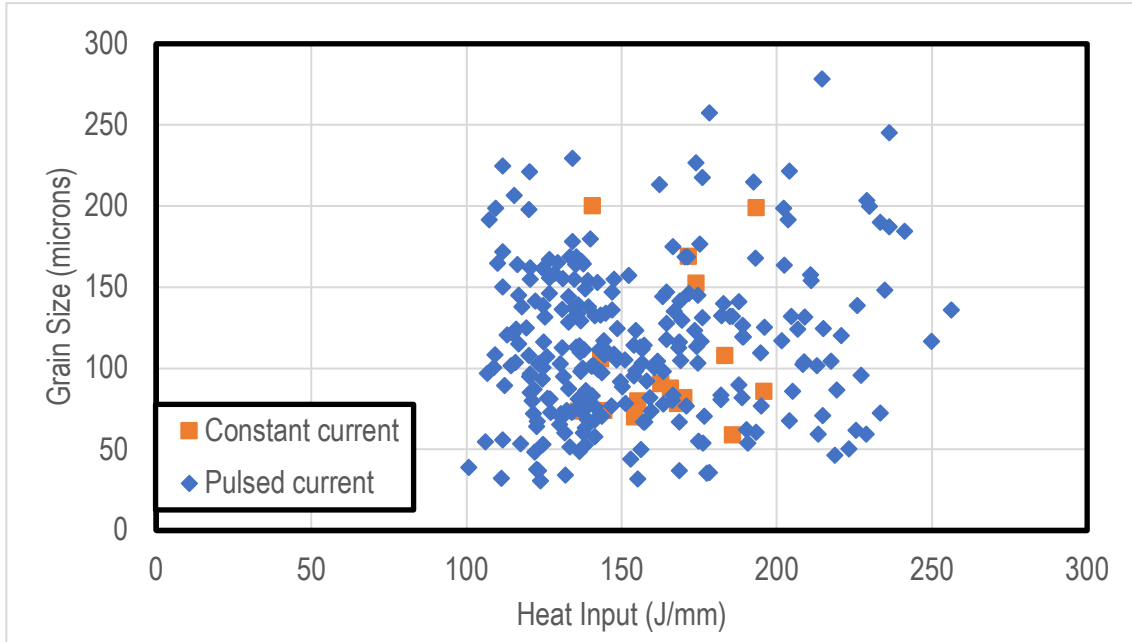
Figure 40: Equiaxed grains size as a function of the heat input in Grade 441
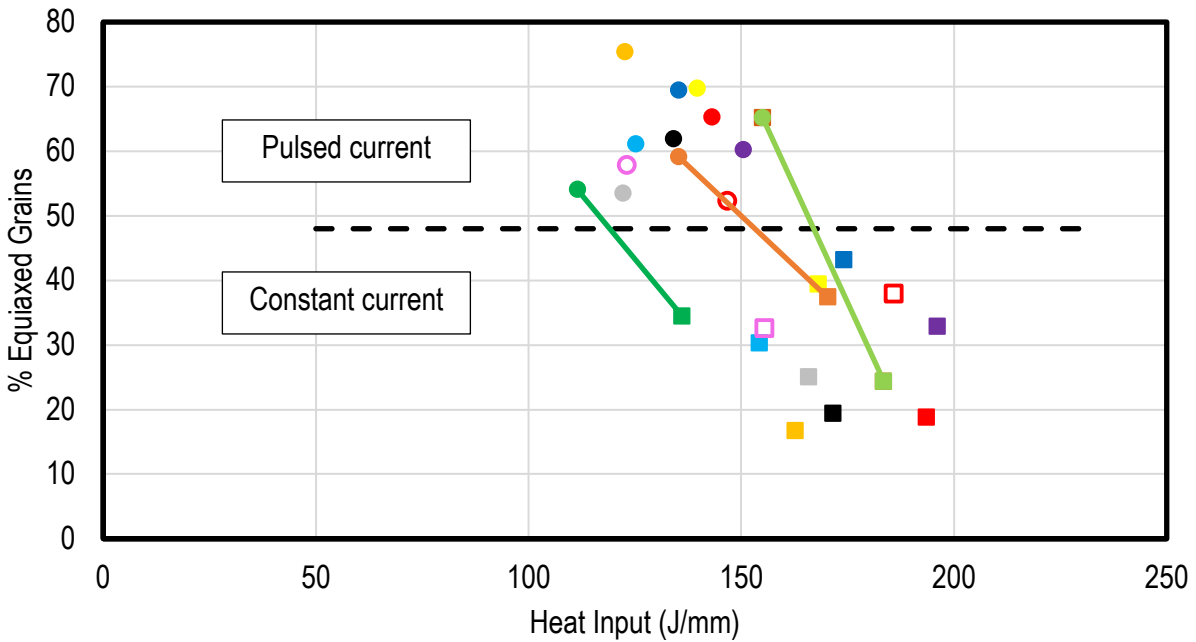
Figure 41: Effects of pulsed current welds versus constant current welds of Grade 441. The data indicates direct comparisons from a subset of data selected, where a pulsed current weld corresponds with a constant current weld (indicated by the same colour and shape), with similar peak welding currents, welding speed and electrode tip angle. For illustration, three data sets were connected by lines.

4.2 Structure of Grade 436 welded joint

Figure 42 indicates the Grade 436 base material structure. The average grain size as received was determined to be 41 µm using the line intercept method. Figure 43 shows a typical all weld metal microstructure of Grade 436 that represents all samples that were welded autogenously with both constant and pulsed current. Grade 436 did not have any equiaxed grain formation in the welds and all microstructures were 100% columnar. All the microstructures of Grade 436 had a linear plane of grain boundaries meeting in the weld center from opposite sides. From Figure 43, the cellular solidification structure of the columnar grains could also be seen.

Figure 42: Typical microstructure of Grade 436 base material as received from Columbus Stainless (Pty) Ltd. (Magnification: 50x)
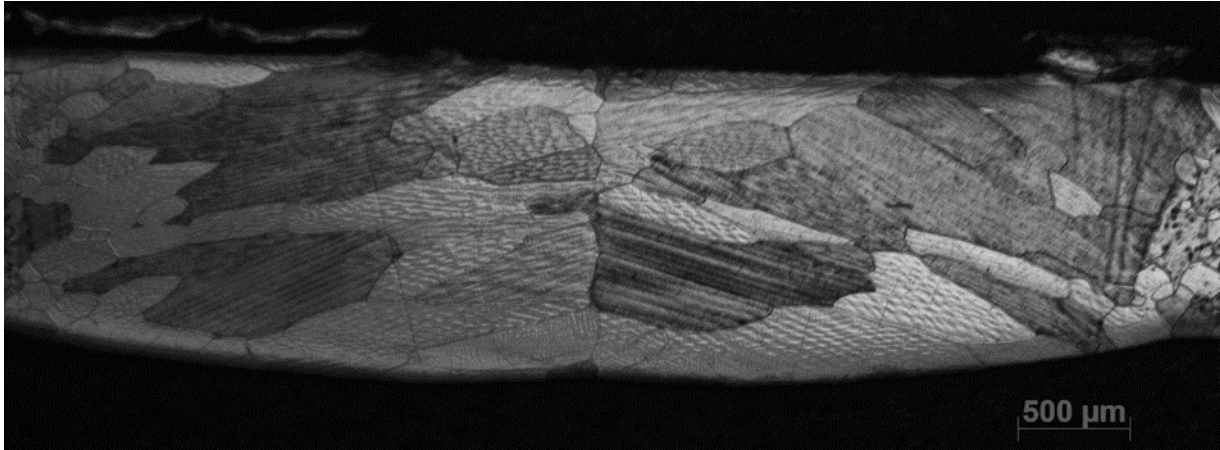
Figure 43: Typical transverse microstructure of Grade 436 weld metal. The microstructure represents both pulsed and constant current welds with no equiaxed grains observed (Weld ID: A18010, welded at 180A, 10 mm/s, an electrode tip angle of 30° and constant current) (Magnification: 25x)

Figure 44 illustrates the effects that the heat input has on the grain size of Grade 436 welds. The constant current Grade 436 welds had higher heat inputs and resulted in thicker columnar grains as compared to the pulsed current. It was shown that a heat input of 190-230 J/mm achieved by current pulsing had the smallest grain thicknesses.
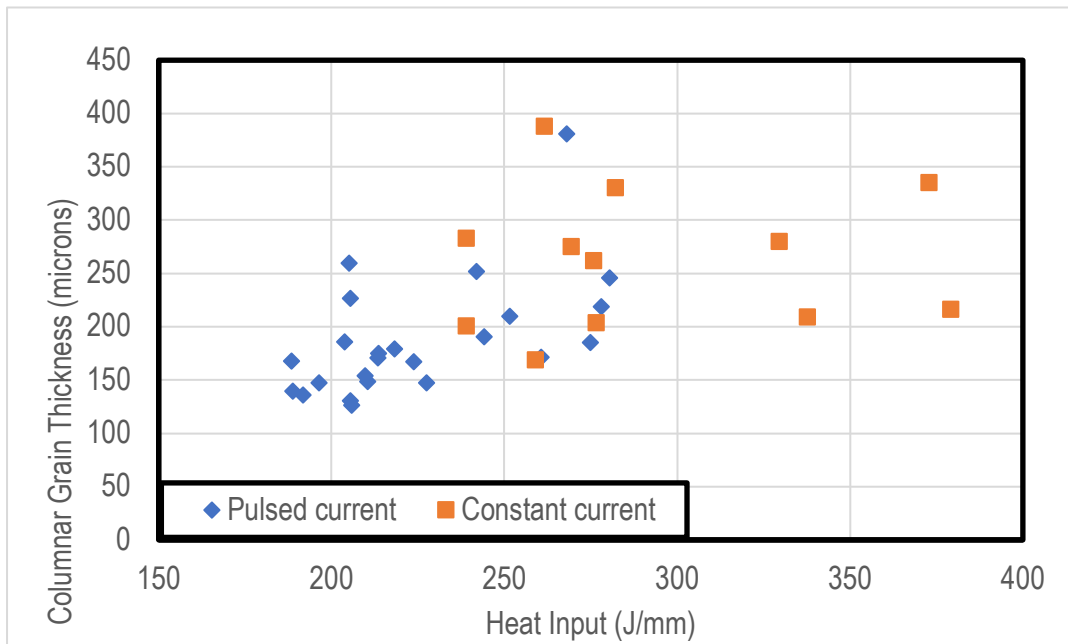
Figure 44: Effects of the heat input on the columnar grain thickness of Grade 436 weld metal, as measured by means of the linear intercept method, discussed in Figure 25

Figure 45 indicates the differences achieved by pulsed current compared to constant current found in the columnar grain thickness. It can be observed that the pulsed current had an effect on the heat input to the process and that the columnar grain thickness remain within 50 microns regardless of welding speed and peak welding current. The constant current welds indicated a higher heat input and larger columnar grain thickness if compared to pulsed current welds. The reduction in heat input due to the use of a pulsing current was consistent with previously published work (Abu-Aesh, Taha, El-Sabbagh & Dorn, 2019; David, Babu & Vitek, 2003).The columnar grain thickness for constant current welds was observed to be within a range of 200 µm regardless of welding speed and peak welding current. It should however be noted that even though the heat input decreased for pulsed current welds, the constant current welds overlapped the pulsed current welds when the columnar grain thickness was considered. The effects of pulsing can therefore be observed as minimal when the columnar grain thickness of the weld is considered.
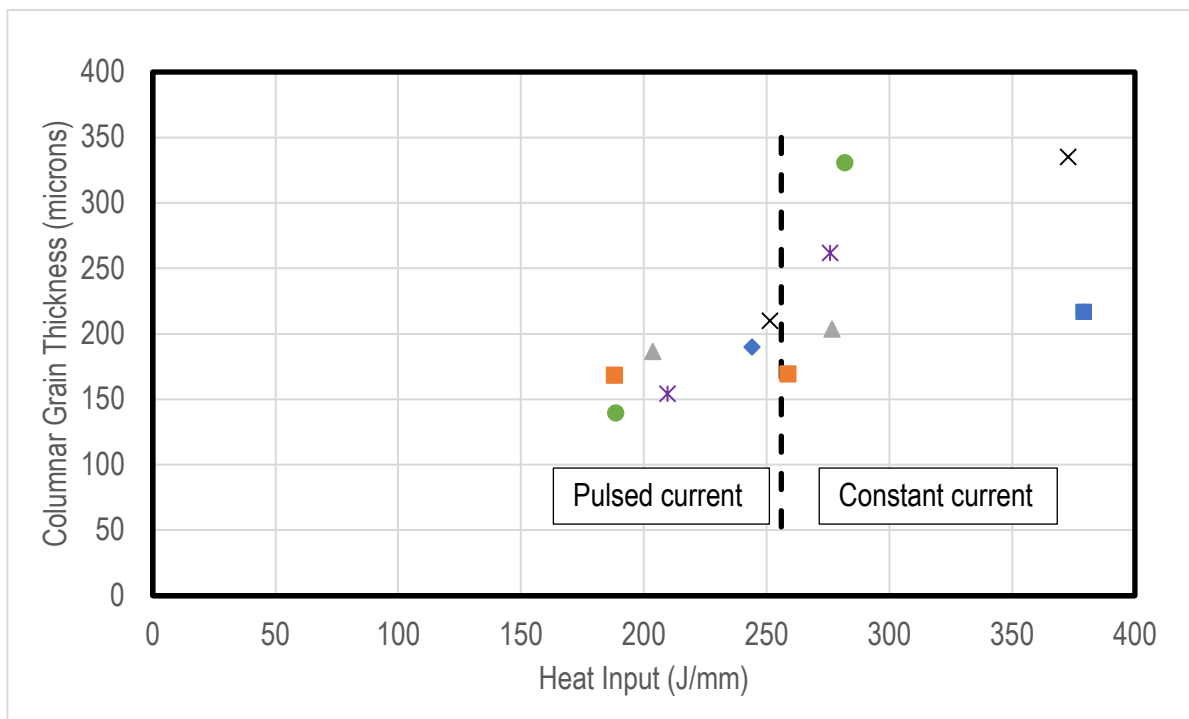
Figure 45: Effects of pulsed current welds versus constant current welds of Grade 436. The data indicates direct comparisons from a subset of data selected, where a pulsed current weld corresponds with a constant current weld, with similar peak welding currents, welding speeds and electrode tip angles.

4.3 Mechanical properties of the weld metal

Hardness profiles on transverse sectioned welds were measured of selected welds of Grade 441 - Figure 46. The base metal usually had a lower hardness than the weld metal. A transverse tensile test coupon would most likely have failed in the base material rather than testing the elongation of the weld metal.
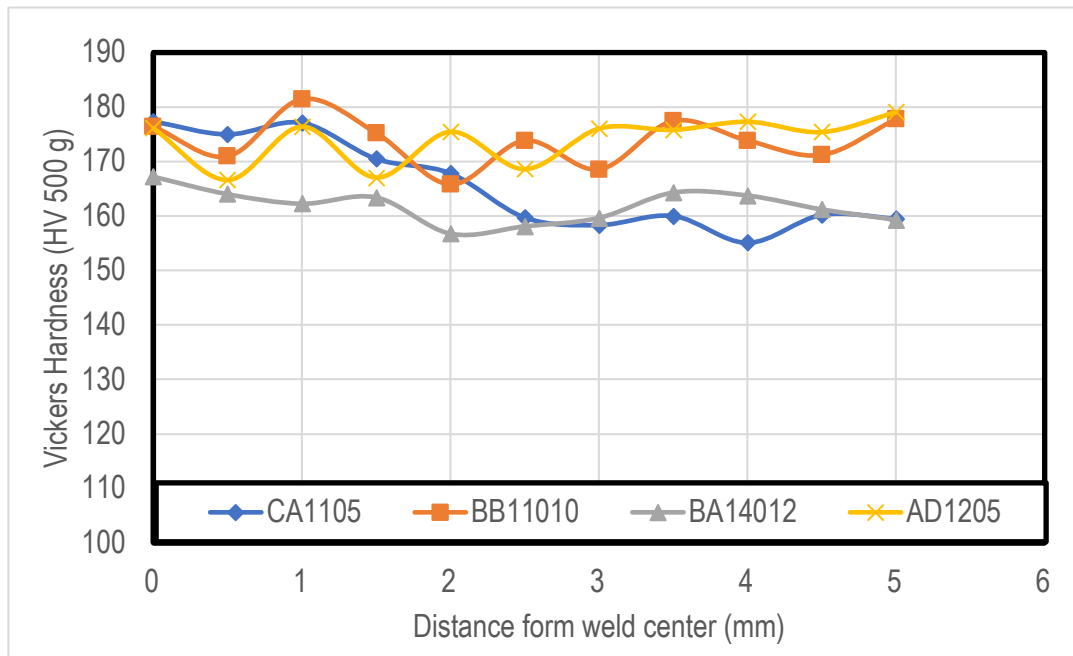
Figure 46: Hardness profiles of selected transverse sections across the weld metal of Grade 441. The fusion boundaries were at 2 mm from the weld center for the samples considered.

Typical stress-strain curves of Grade 441 are illustrated by Figure 47. Three representative specimens were selected for each subset that represents a 50% weld metal in the tensile specimen gauge width, a full weld metal in the gauge width and a full base material specimen. It should be noted that the range in ultimate tensile strength for 100% weld metal, 100% base metal and 50% weld metal were small. As a consequence, the tensile strength (R_m) was not evaluated. The base metal was expected to resist a higher strain as Figure 47 shows, between 40 and 45% elongation. The 50% weld metal strain (between 30 and 35%) fell in between the 100% weld metal and the 100% base metal coupons, which was expected that the base material present in the tensile gauge area would maintain the strain when the weld metal has failed. The 100% weld metal tensile coupons had lower strains than the 50% weld metal and 100% base metal coupons, falling in between 27 to 31%.
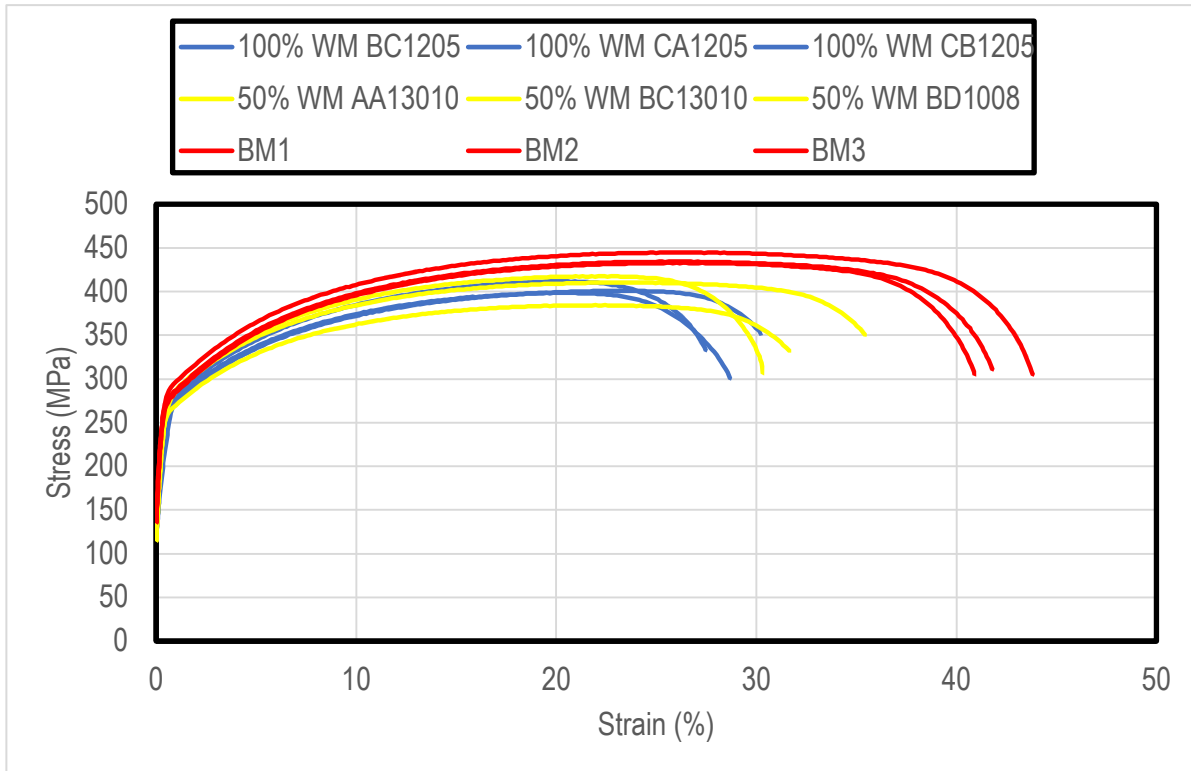
Figure 47: Illustration of the different tensile specimens observed of Grade 441. The results indicated how faster welding speeds (50% weld metal, Weld ID: AA13010) compared to slower welding speeds (100% weld metal, Weld ID: BC1205) and the 100% base material of Grade 441

Figure 48 illustrated the elongation as a function of the heat input at different welding speeds for pulsed current, the base material and constant current welds. An increase in the welding speed leads to a decrease in the heat input. Further, the heat input does not have an influence on the elongation of Grade 441 ferritic stainless steel. The elongation remained constant with no clear effect of welding parameters on the elongation. Figure 49 illustrated how the amount of equiaxed grains influenced the elongation. From the figure it could be assumed that a higher welding speed leads to an increase in the amount of equiaxed grains present in the weld metal. This could however not be concluded from this figure as large overlapping occurred between different welding speeds. The fact that welding speed has an influence on the amount of equiaxed grains present in Grade 441 was however confirmed with statistical analysis. It was clear from the figure that the elongation was not affected by the amount of equiaxed grains present in the weld metal microstructure of autogenously welded Grade 441. For this grade, the ductility, quantified as tensile elongation to fracture of the weld metal, was not influenced by using either pulsed or constant current, the heat input or the amount of equiaxed grains.

72
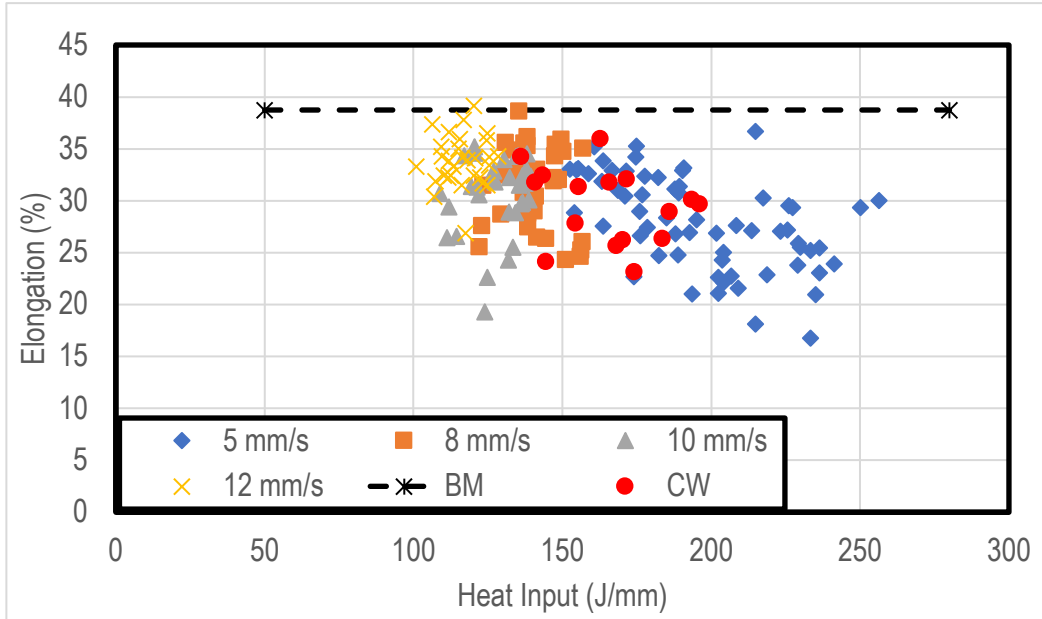
Figure 48: Ductility, quantified as tensile elongation to fracture for Grade 441 weld metal, as a function of heat input at different welding speeds. The base metal elongation is indicated by a dotted line.
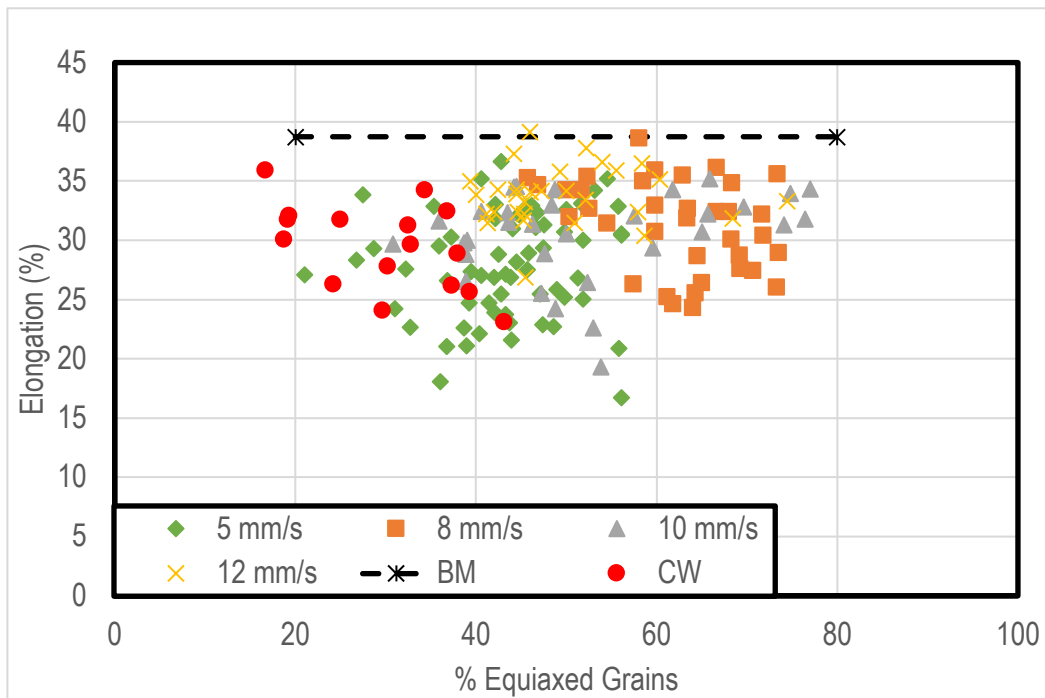
Figure 49: Ductility, quantified as tensile elongation to fracture, as a function of % equiaxed grains in Grade 441 weld metal. The base metal elongation is indicated by a dotted line.

73

Figure 50 illustrates how the percentage weld metal in the gauge area of a tensile coupon was calculated from the cross sectional area of the gauge area and the area of the weld metal. The weld bead top width (w_{top}) and weld bead bottom width (w_{bottom}) were measured as indicated by Figure 20 and the area of the weld metal was determined by the trapezoidal area – Equation 10.

$$Weld\ area = \frac{w_{top} + w_{bottom}}{2}\ t \qquad\qquad \textit{Equation 10}$$
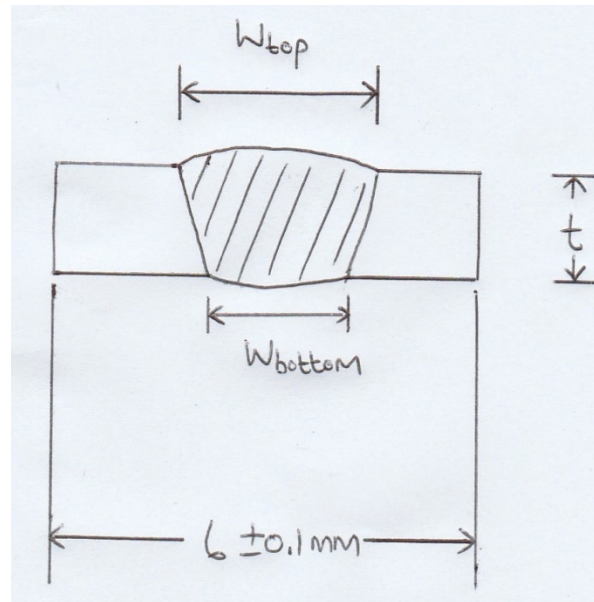
Figure 50: Illustration of how the percentage weld metal in the tensile gauge area was determined.

The effect of the fraction of weld metal in the gauge width of the tensile coupon gauge area (as determined by Figure 50) was further investigated to identify the effects that the base metal present (if any) had on the elongation. Figure 51 indicates the distribution of Grade 441 tensile data as a function of the percentage weld metal present in the tensile coupon gauge area. The figure also includes the average elongation that relates to the percentage weld metal present in the gauge area of the tensile coupon. From the figure it can be concluded that the elongation was determined by the amount of weld metal present in the gauge area of the tensile coupons. The fit of this data extrapolates to 40% elongation at zero weld metal, consistent with the average elongation recorded for Grade 441 base material (39%). This is consistent with Figure 51, where the best fit equation indicates that the base material should have an elongation of 40% and an R^2 of 0.87, which indicates a strong correlation. This could be due to the equiaxed grains present in the weld metal of

Grade 441 having similar shapes and sizes to the as received grain structure of the base metal, hence providing similar elongation results.
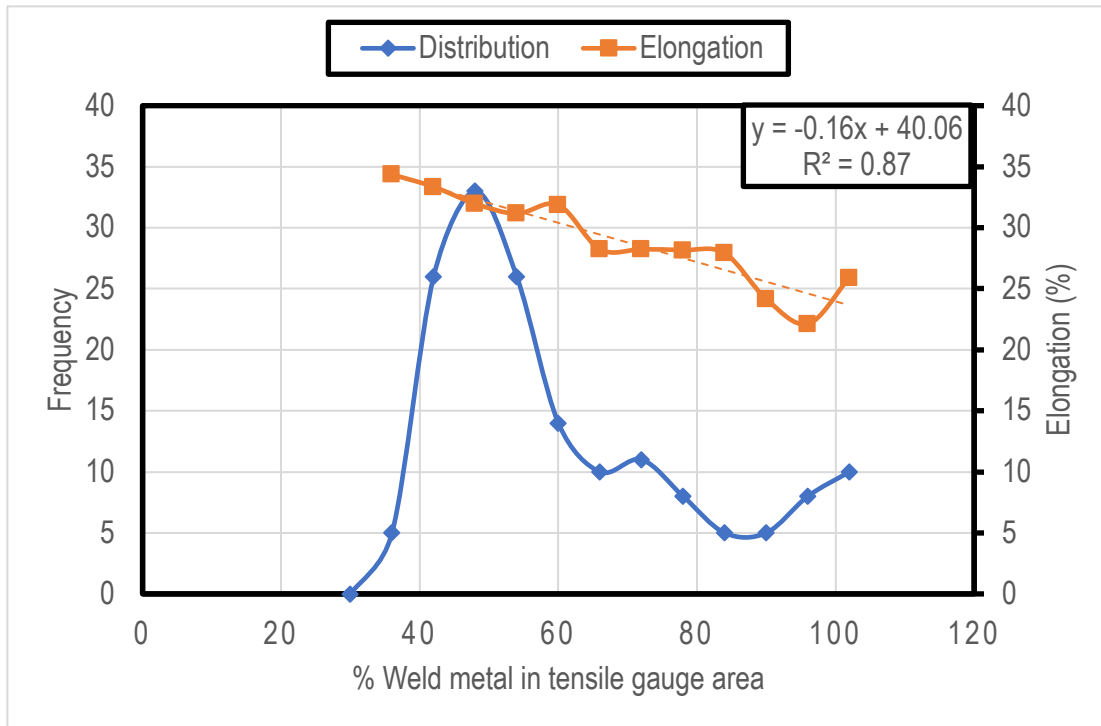
Figure 51: Distribution of the percentage weld metal present in Grade 441 tensile coupon gauge area. The average elongation as a function of the percentage weld metal present was also included. Observations: 257

The tensile curves for the autogenous GTAW of Grade 436 ferritic stainless steel are illustrated in Figure 52. The figure shows the flow curves of three representative base metal specimens, three specimens that only contained weld metal and three specimens that contained 50% base metal and 50% weld metal. The flow curves indicated that the specimens containing 50% base metal - 50% weld metal could withstand a strain in between the specimens that contained only weld metal or only base metal.
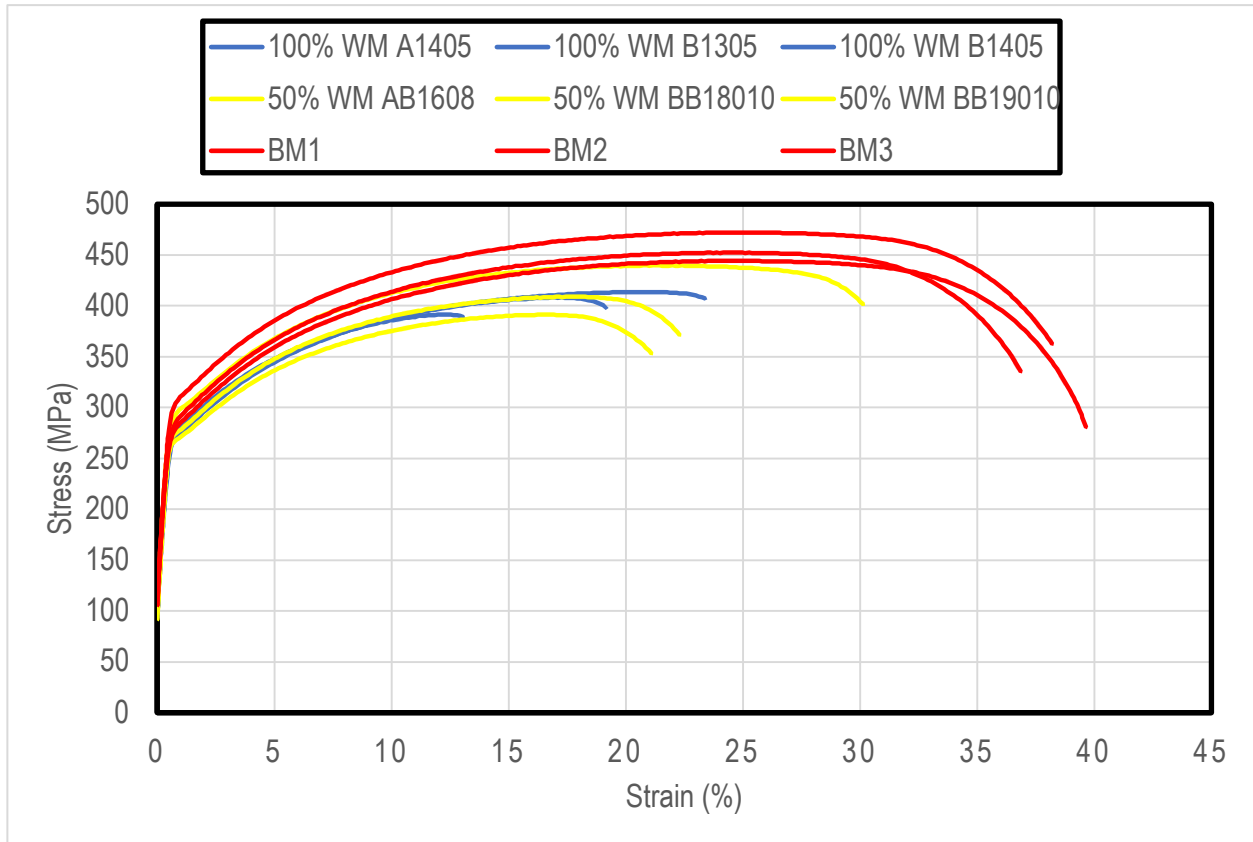
Figure 52: Illustration of different tensile specimens observed in Grade 436. The results indicated how faster welding speeds (50% weld metal, Weld ID: BB18010) compared to slower welding speeds (100% weld metal, Weld ID: A1405) and the 100% base material of Grade 436

The elongation as a function of the heat input for Grade 436 is illustrated by Figure 53. The elongation of the weld material for both pulsed current and constant current did not indicate a clear relationship. The elongation as a function of the grain size is illustrated by Figure 54. Again, the pulsed current and constant current did not indicate a clear relationship with elongation. It could therefore be concluded that the heat input, the use of pulsed or constant current or the grain size did not influence the ductility (quantified as tensile elongation to fracture) of the weld material of Grade 436.
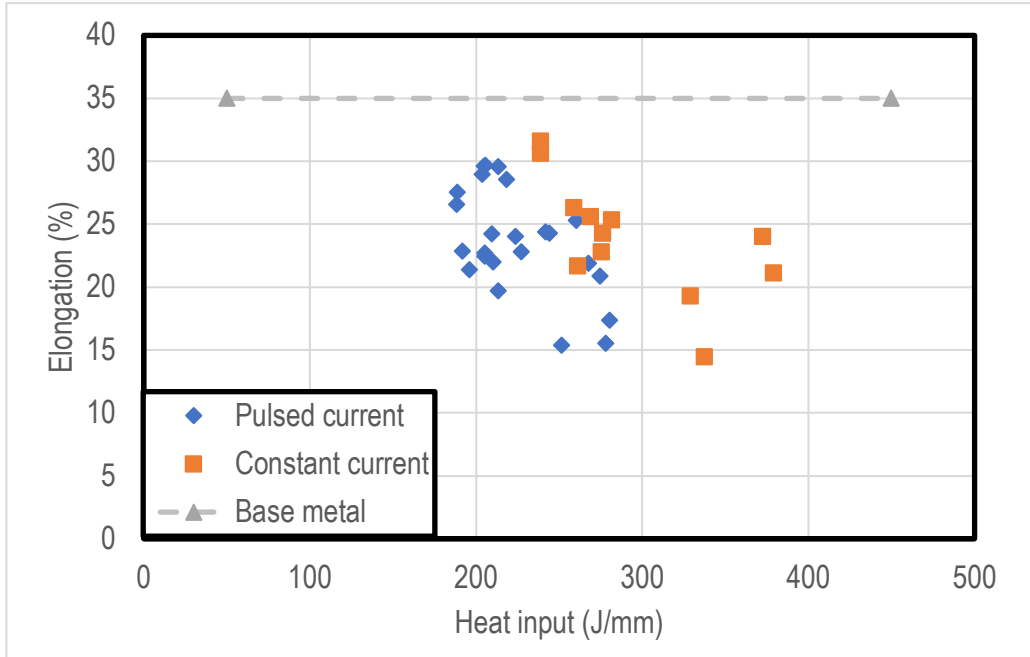
Figure 53: Ductility, quantified as tensile elongation to fracture, as a function of heat input for pulsed and constant current welds of Grade 436. The average base metal elongation was added for comparison
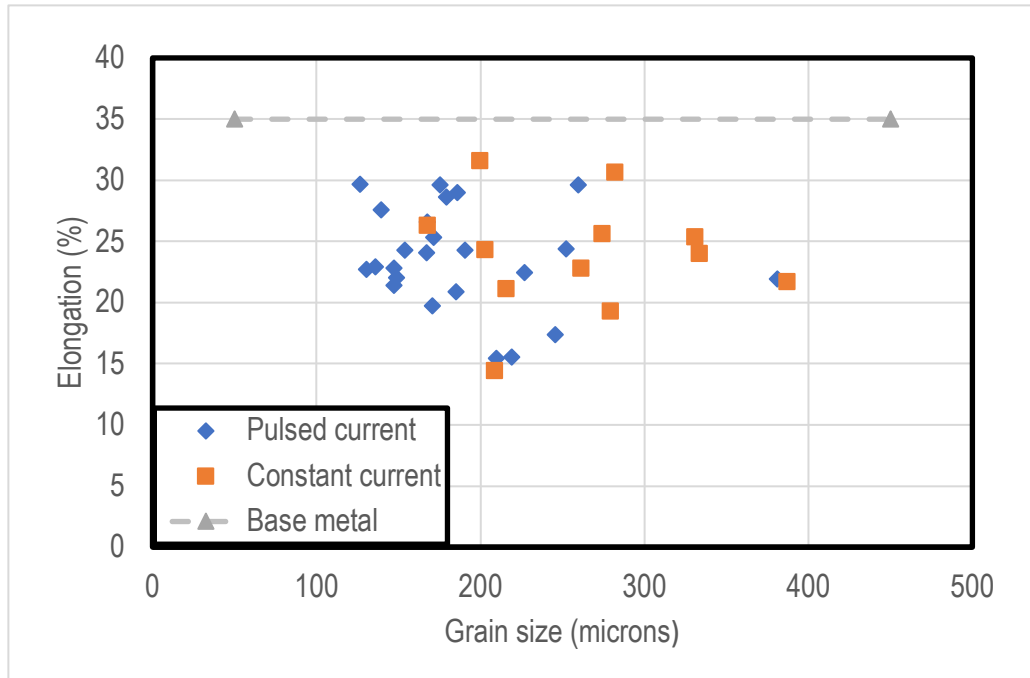
Figure 54: Ductility, quantified as tensile elongation to fracture, as a function of grain size of Grade 436 for constant and pulsed current. The average base metal elongation was added for comparison

Figure 55 indicates the distribution of Grade 436 tensile data as a function of the percentage weld metal present in the tensile coupon gauge area. The figure also included the average elongation that relates to the percentage weld metal present in the gauge area of the tensile coupon. The fit of this data extrapolates to 26% elongation, a value that was not consistent with the average elongation recorded for Grade 436 base material (35%). The lack of fit for the elongation (R^2 = 0.19), in terms of the % weld metal in the tensile coupon, can be due to the low number of samples tested for this grade. Since Grade 441 had varying amounts of equiaxed grains present in the weld metal and having similar grain sizes and shapes as the as received base metal grains, it is expected that the weld metal to behave in a similarly manner than the base metal. It could be for the lack of equiaxed grains in the weld metal of Grade 436 that the elongation was not sensitive to the amount of weld metal present in the tensile gauge area.
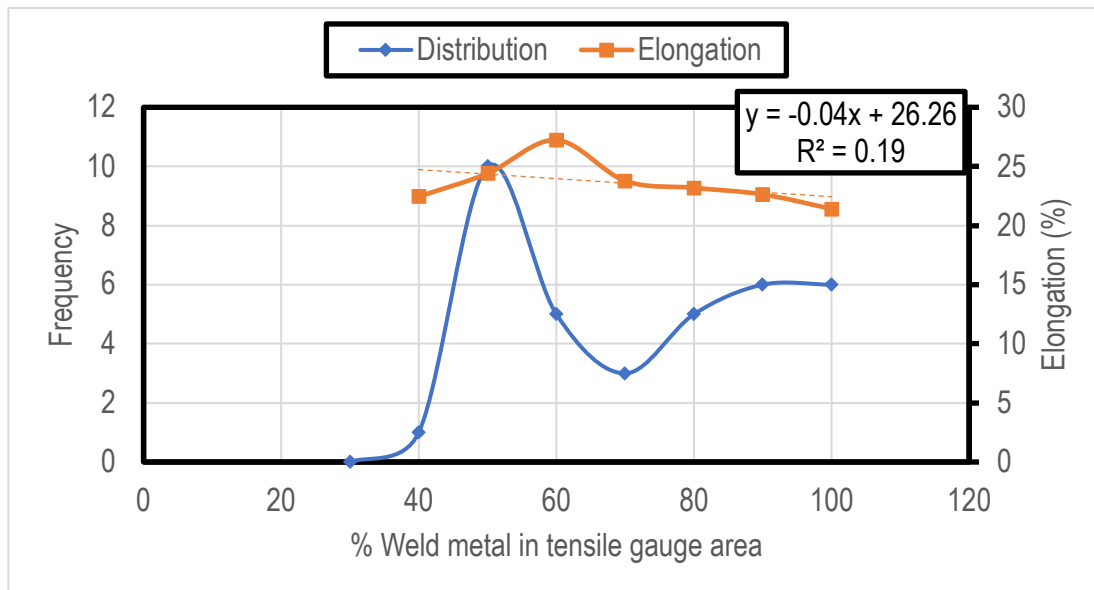
Figure 55: Distribution of the percentage weld metal present in Grade 436 tensile coupon gauge area. The average elongation as a function of the percentage weld metal present was also included. Observations: 36

Figure 56 and Figure 57 show the scanning electron micrographs (SEM) of fracture surfaces of tensile coupons of Grade 441 and 436. Both Grades 441 and 436 followed similar trends where the thinnest sections were in the middle of the coupon where the weld metals were present and flaring out at the edges of the coupons where the base metal is present. The shape of the fracture surface indicated that the ductility of the weld metal was not significantly lower than that of the base metal and the presence of dimples indicated plasticity - Figure 51.
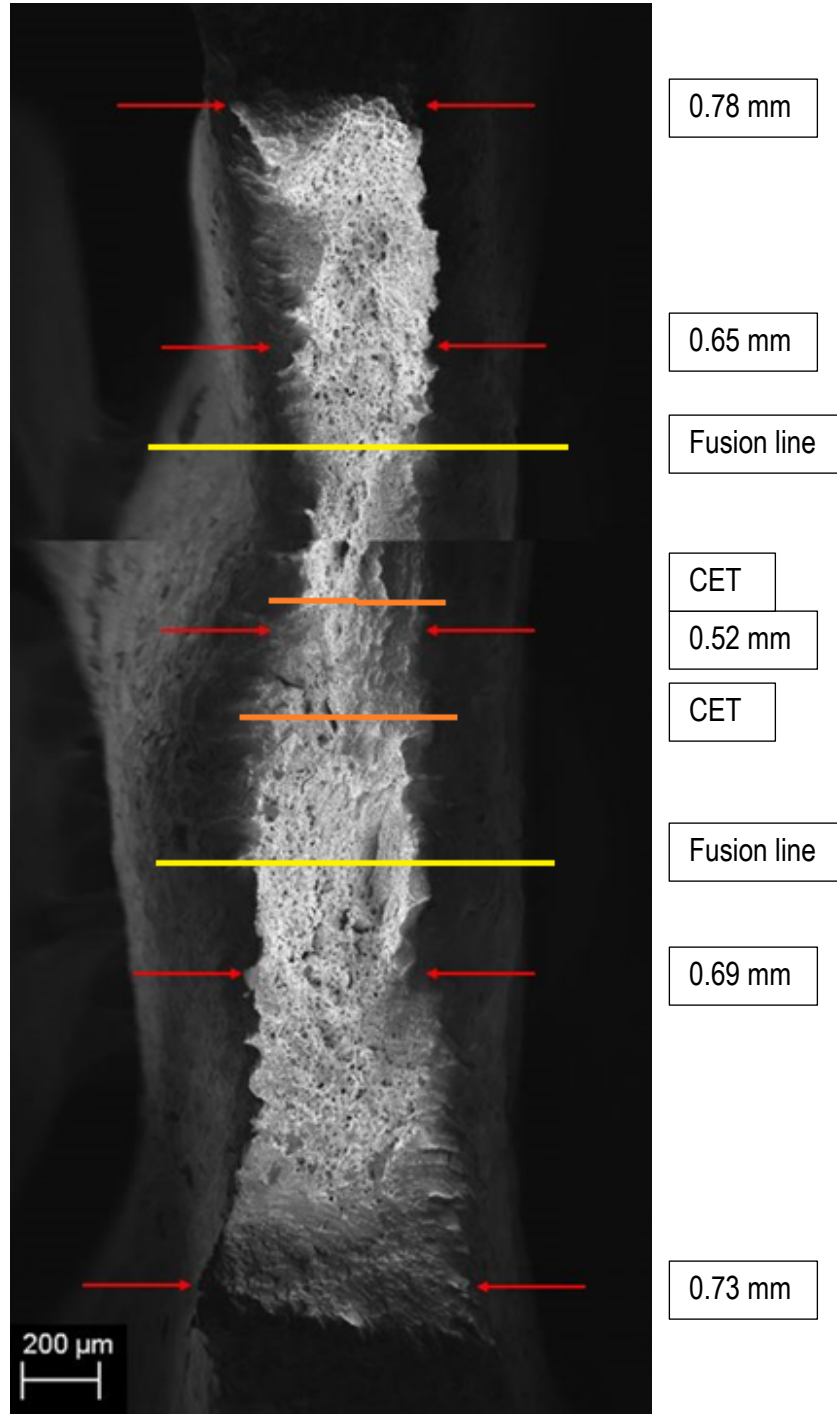
Figure 56: Scanning electron micrograph of the fracture surface of a tensile coupon machined from a Grade 441 weld that had 30% weld metal in the tensile gauge width. The shape of reduction in area is indicated by dimensions, the fusion line and columnar-to-equiaxed transition was added as indicated. (Weld ID: CB13012, with a pulse frequency of 20Hz, an electrode taper angle of 30°, peak welding current of 130A and a welding speed of 12 mm/s. The sample had 54% equiaxed grains and a 37% elongation). Magnification: 80x
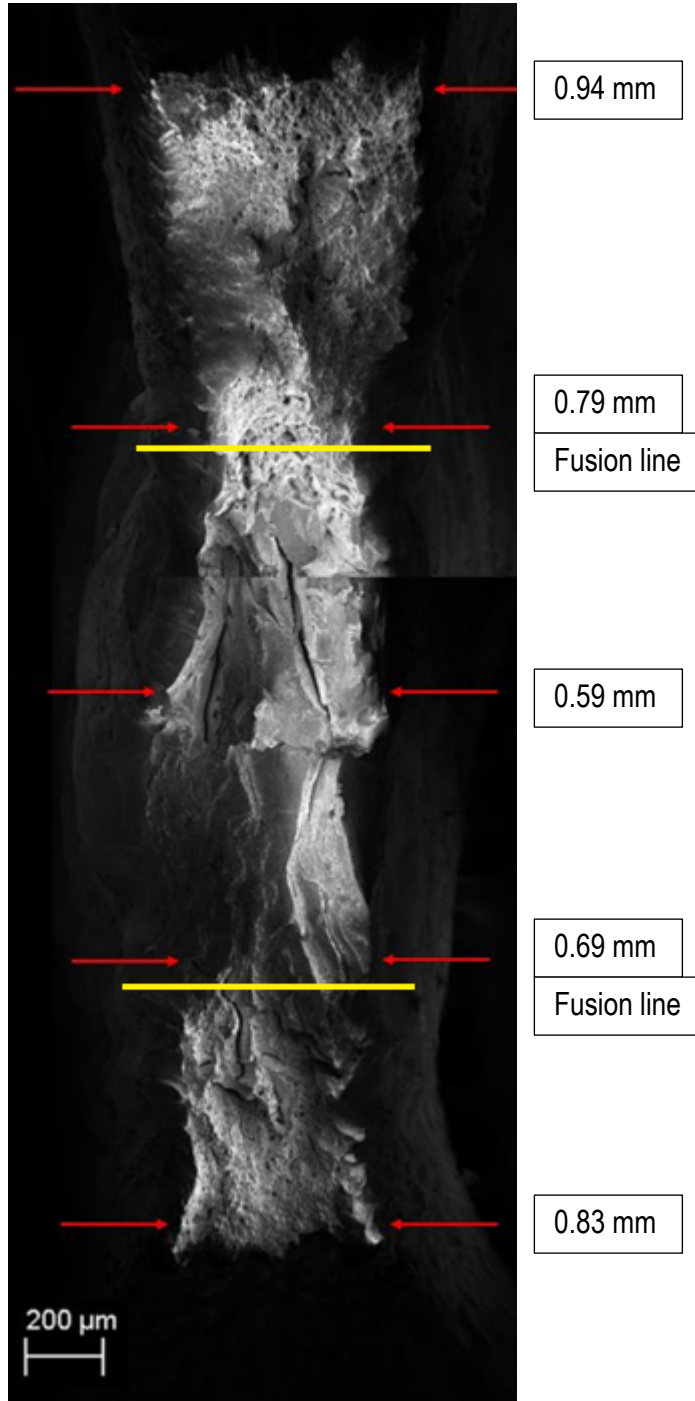
Figure 57: Scanning electron micrograph of the fracture surface of a tensile coupon machined from a Grade 436 weld that had 30% weld metal in the tensile gauge width. The shape of reduction in area is indicated by dimensions, the fusion line and columnar-to-equiaxed transition was added as indicated. (Weld ID: AA19010, with a pulse frequency of 15Hz, an electrode taper angle of 30°, peak welding current of 190A and a welding speed of 10 mm/s. The sample had a 180 µm average grain size and a 29% elongation). Magnification: 80x

Figure 58 shows the typical fracture surface of a Grade 441 base metal test coupon. The figures indicated spherical ductile dimples. Figure 59 shows the normal section of a tensile coupon. The area investigated is illustrated in red. The area was where the columnar-to-equiaxed transition (CET) occurred. This area was then investigated by SEM-analysis in Figure 60, which was representative of tensile coupons that had 100% weld metal in the gauge area. Figure 61 represents the fracture surface of tensile coupons with 50% weld metal in the gauge area. Clear from Figure 60, Figure 61 were the spherical ductile dimples, cleavage fracture and intergranular fracture of Grade 441 weld metal. Cleavage fracture was found where the fracture occurred trans-granularly and the fracture passed through the grains in specific crystallographic planes (Callister & Rethwisch, 2011).
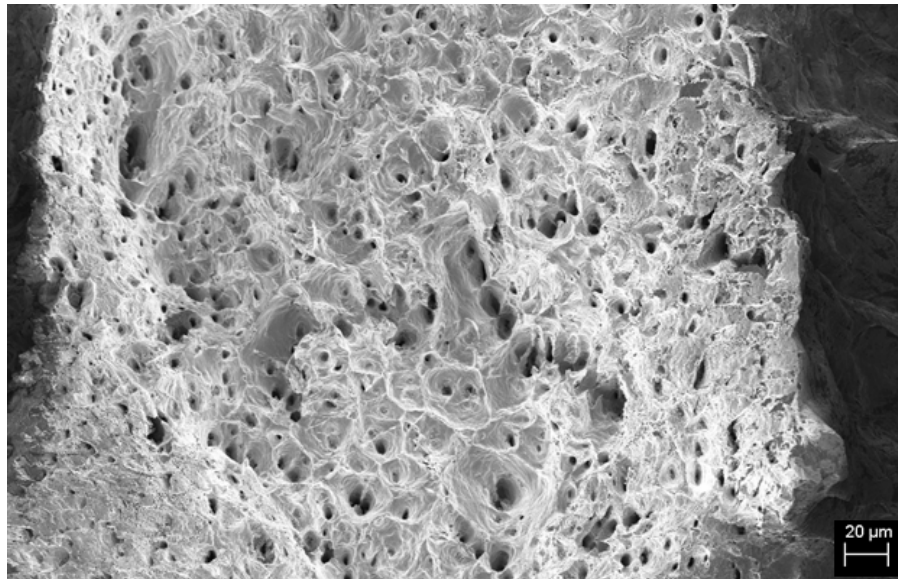
Figure 58: Scanning electron fractograph of Grade 441 base material. Spherical dimples are visible that indicated ductile fracture, consistent with a 39% elongation.
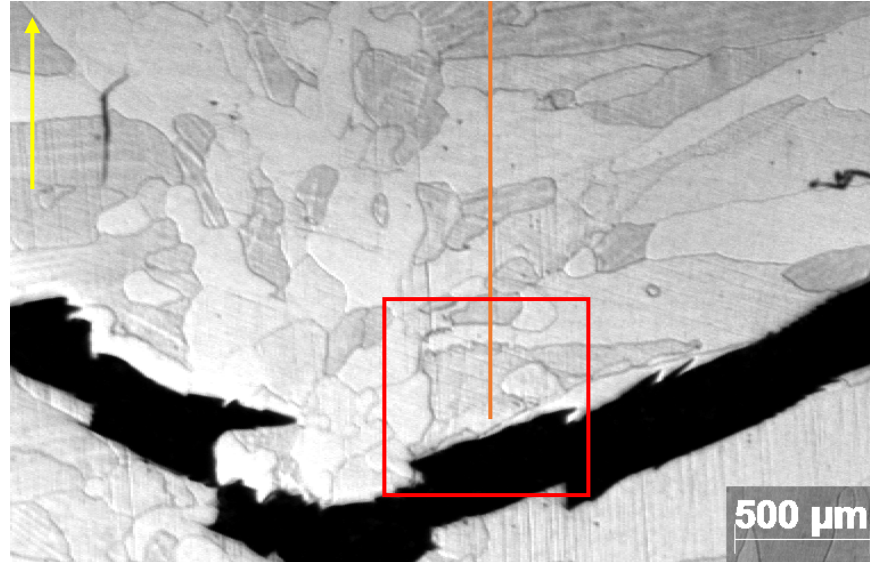
Figure 59: Normal section of a fractured tensile coupon from Grade 441. The columnar-to-equiaxed transition (CET) is indicated by the orange line, the welding direction is indicated by the yellow arrow. The area illustrated in Figure 60 is illustrated by the red square. (Weld ID: AD1205,with an electrode tip angle of 20°, pulse frequency of 30Hz, peak welding current of 120A and a welding speed of 5 mm/s. The sample had 52% equiaxed grains and a 30% elongation).
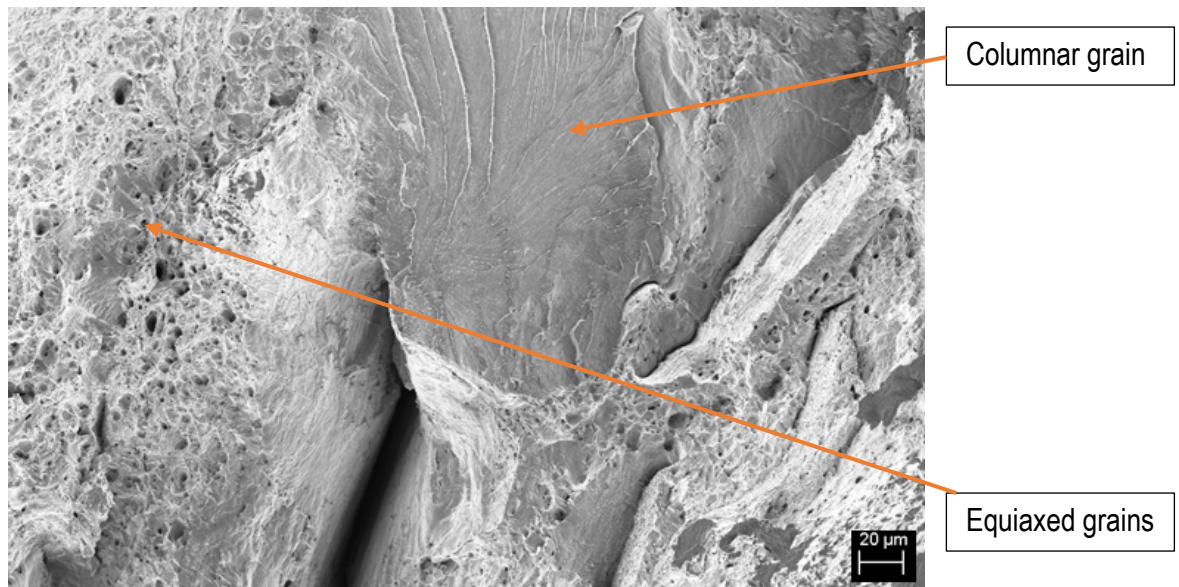
Figure 60: Scanning electron fractograph of a tensile coupon containing only weld metal in Grade 441. Ductile dimples, cleavage fracture and intergranular fracture was observed. (Weld ID: BC12010,with an electrode tip angle of 30°, pulse frequency of 25Hz, peak welding current of 120A and a welding speed of 10 mm/s. The sample had 53% equiaxed grains and a 23% elongation).
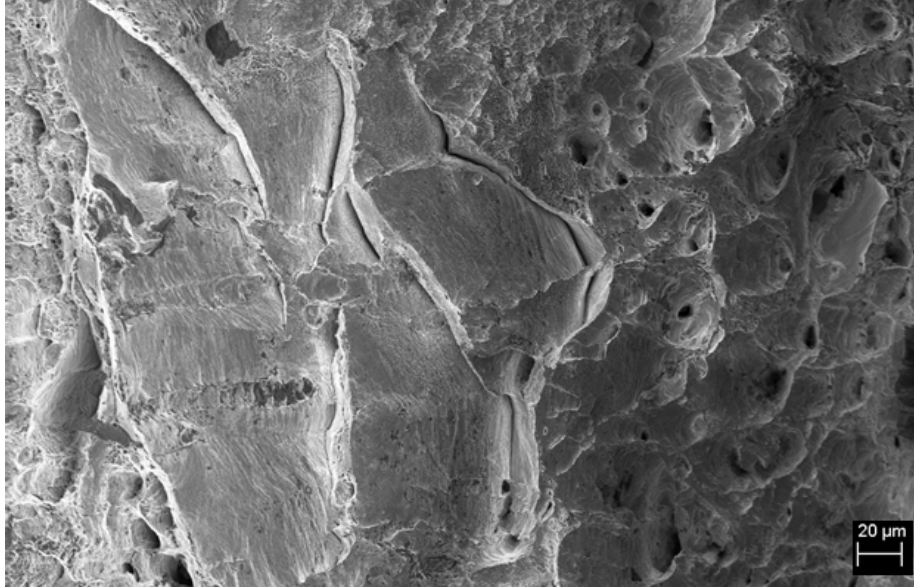
Figure 61: Scanning electron fractograph of Grade 441 weld metal. The figure is representative for a tensile coupon consisting of 50% weld metal. Ductile dimples, cleavage fracture and intergranular fracture was observed. (Weld ID: BD12010, with an electrode tip angle of 30°, pulse frequency of 30Hz, peak welding current of 120A and a welding speed of 10 mm/s. The sample had 54% equiaxed grains and a 19% elongation).

Figure 62 illustrates the typical fracture surface of Grade 436 base material. The mode of fracture was ductile as spherical ductile dimples were present. Figure 63 represents the typical fractograph of Grade 436 weld metal. The figure illustrates ductile dimples, cleavage fracture and intergranular fracture.
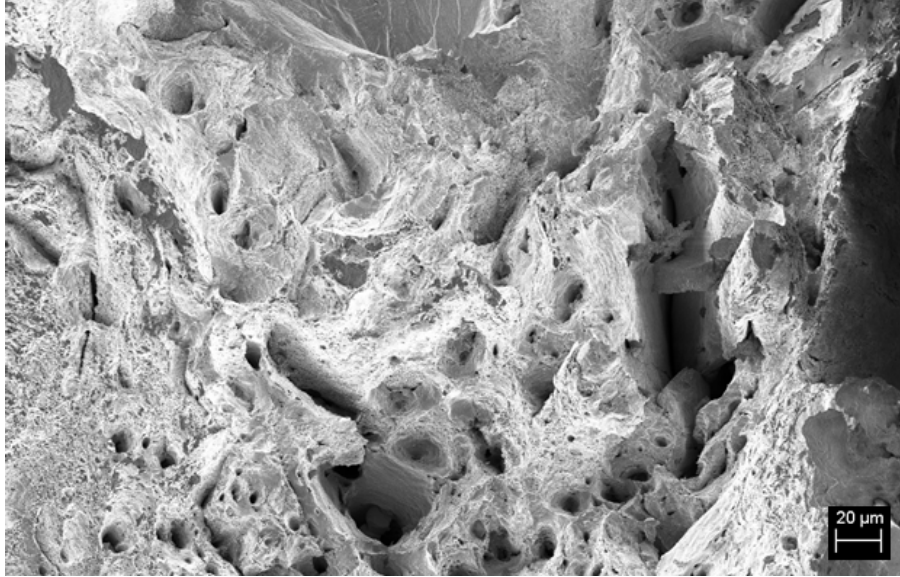
Figure 62: Scanning electron fractograph of Grade 436 base material. Spherical ductile dimples were present, consistent with an elongation of 35%.

Columnar grain
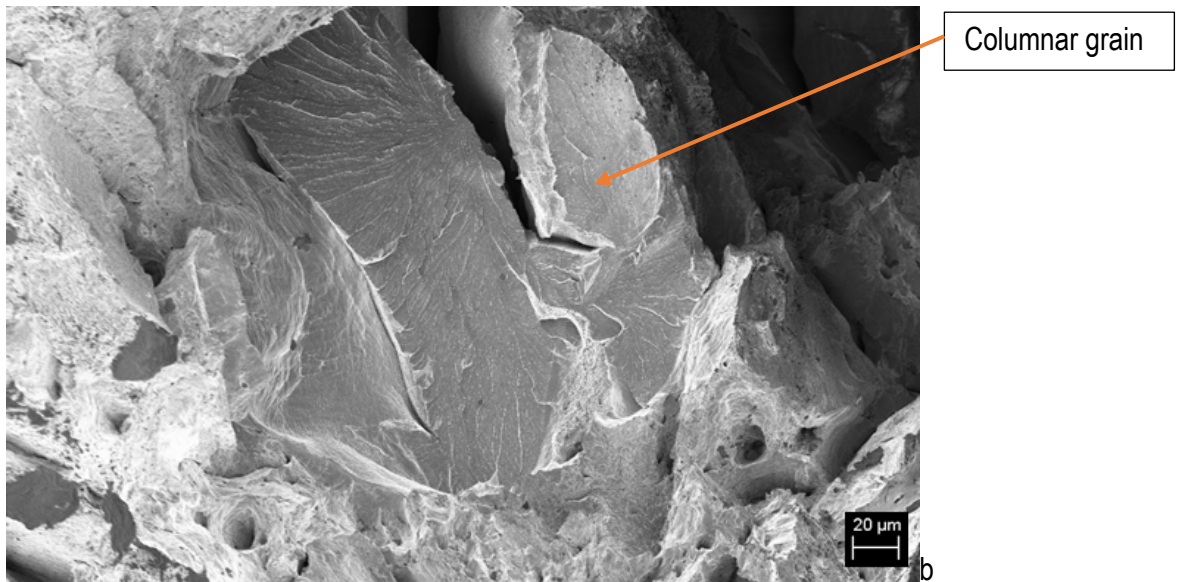
Figure 63: Scanning electron fractograph of Grade 436 weld metal. Ductile dimples, cleavage fracture and intergranular fracture was observed. (Weld ID: AA19010, with an electrode tip angle of 30°, pulse frequency of 15Hz, peak welding current of 190A and a welding speed of 10 mm/s. The sample had 180 μm average grain size and a 29% elongation).

4.4 Effect of titanium on the fraction equiaxed grains in the weld metal

Since the current investigation was focussed on the effects of the welding parameters on the microstructural changes of Grade 441 and 436, the effect of alloying elements on the weld metal microstructure was not considered systematically. However, given that two steels (Grade 441 with 0.18% titanium and Grade 436 with no titanium) were evaluated, a brief discussion on the effects of titanium on the amount of equiaxed grains is possible. Figure 64 shows the results for Grade 441 and 436 (from the current study) and of Villafuerte, Pardo and Kerr (1990) that evaluated the effects of welding speeds and titanium content on the amount of equiaxed grain formation with GTAW. Figure 64 also includes the work done by Villaret, Deschaux-Beaume, and Bordreuil (2013), who investigated different filler wire compositions (with different titanium contents) with GMAW butt-welds on Grade 444 ferritic stainless steel. Villaret, Deschaux-Beaume, and Bordreuil (2013) did not specify the welding speed.

The following observations were made from Figure 64:

- A low titanium weld metal contains a low fraction of equiaxed grains.
- A higher titanium weld metal contains a higher fraction of equiaxed grains.
- There appears to be an abrupt change in the equiaxed grain amount in the weld metal with titanium content.
- Gas metal arc welds with a titanium content above 0.15% had a high fraction of equiaxed grains (Villaret, Deschaux-Beaume, and Bordreuil, 2013).
- Gas tungsten arc welds with a titanium content above 0.25% had 20 to 35% equiaxed grains (Villafuerte, Pardo & Kerr, 1990).
- Gas tungsten arc welds with a titanium content of 0.18% had 17 to 77% equiaxed grains (current study).

It was clear that the behaviour of Grade 436 with no titanium addition as determined during the current study, was consistent with reports from previous studies, with no equiaxed grains in the weld metal. Grade 436 weld metal should not, according to Villaret, Deschaux-Beaume, and Bordreuil (2013), contain any equiaxed grains, regardless of welding speed, peak welding current or the use of pulsed current.

The titanium content of Grade 441 was such that the equiaxed grain percentage should be high, regardless of the welding speed. Villaret, Deschaux-Beaume, and Bordreuil (2013) found that the titanium content would increase the amount of equiaxed grains. It could be that the Grade 441 base metal used for the current study fell within this region of transition, where the equiaxed grains could either be low or high, especially when considering the results achieved by Villaret, Deschaux-Beaume, and Bordreuil (2013) and Villafuerte, Pardo and Kerr (1990).
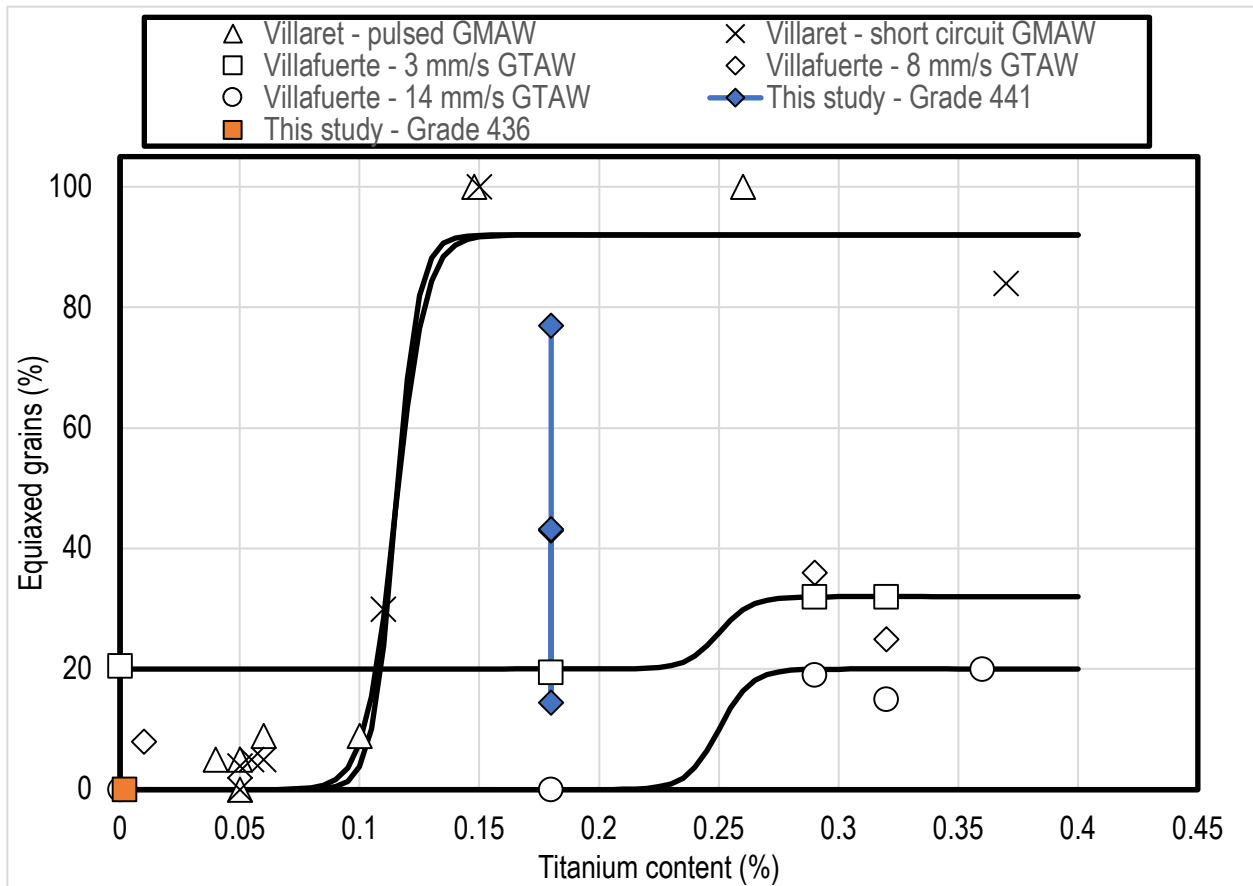
Figure 64: Effect of titanium addition on the amount of equiaxed grain formation for both Grade 436 and 441 of the current investigation as compared to unknown grades of stainless steel from Villafuerte, Pardo and Kerr (1990) at three different GTA welding speeds. Results of GMAW filler metals by Villaret, Deschaux-Beaume, and Bordreuil (2013) were also included for comparison

It was clear from Figure 64 that the titanium content of ferritic stainless steel plays an important role in the formation of equiaxed grains. These results were broadly consistent with the results of previous work, where an abrupt change in percentage of equiaxed grains were observed with increasing titanium content. The percentage of equiaxed grains did not seem to be particularly sensitive to the changes in welding parameters.

It seems that the presence of nuclei in the weld pool (for this study, probably TiN) may be more important to the solidification morphology than the heat flow conditions in the weld pool. The ranges of welding speed and peak welding used in the study was similar for Grades 441 and 436. In spite of the welding parameter similarities, the solidification structure was different.

.

Chapter 5: Discussion of results

5.1 Descriptive statistics of welding variables on the final microstructure of two ferritic stainless steels

The descriptive statistics summarised the welding data to enable ease of interpretation and selection of further statistical analysis methods. Table 16 and Table 17 show the descriptive statistics of Grade 441 pulsed current and constant current, respectively. The median and the mean was similar for both pulsed and constant currents, indicating that the data was symmetrically distributed. The mean amount of equiaxed grains present for pulsed and constant currents differed by 13%, with pulsed current welds containing more equiaxed grains. It could be stated that the use of pulsed current had a definite influence on the amount of equiaxed grains that form in the weld center. It should be noted that the maximum fraction of equiaxed grains was achieved using pulsed current and a certain set of welding parameters, typically found by faster welding speeds. Further, lower heat inputs could be achieved using a pulsed current. The equiaxed grain size determined did not have a significant influence from using a pulsed current power source and the grain sizes were similar for pulsed and constant current welds.

Table 16: Descriptive statistics results for dependent and independent variables of pulsed current Grade 441. The dependent variables include only the % equiaxed grains and fusion line angle. These results included 257 observations

Variable	Dependent/ independent variable	Mean	Standard deviation	Median	Minimum	Maximum
% Equiaxed grains	Dependent	43	14	43	15	77
Fusion line angle (°)	Dependent	67	11	69	36	90
Peak welding current (A)	Independent	115	20	110	90	170
Electrode tip angle (°)	Independent	38	15	30	20	60
Pulse frequency (Hz)	Independent	23	6	25	15	30
Welding speed (mm/s)	Independent	8	3	7	4	14
Heat input (J/mm)	Dependent	156	35	145	101	256
Distance between a pulse (mm)	Dependent	0.4	0.17	0.33	0.13	0.93
Equiaxed grain size (μm)	Dependent	115	47	111	31	278

Table 17: Descriptive statistics results for dependent and independent variables of constant current Grade 441. The dependent variables include only the % equiaxed grains and fusion line angle. These results included 16 observations

Variable	Dependent/ independent variable	Mean	Standard deviation	Median	Minimum	Maximum
% Equiaxed grains	Dependent	30	8	31	17	43
Fusion line angle (°)	Dependent	73	7	75	51	84
Peak welding current (A)	Independent	115	5	115	110	120
Electrode tip angle (°)	Independent	39	16	38	20	60
Welding speed (mm/s)	Independent	9	1	9	8	10
Heat input (J/mm)	Dependent	165	19	167	136	196
Equiaxed grain size (μm)	Dependent	107	46	86	58	200

Table 18 and Table 19 show the descriptive statistics of Grade 436 pulsed current and constant current welds respectively. As the microstructures were fully columnar, the amounts of equiaxed grains could not be determined. It was decided to measure the average columnar grain thickness by means of the line intercept method. The data was again symmetrically distributed, as indicated by the similar values for the median and means of each variable. The average columnar grain thickness decreased from 262 to 188 microns with the use of a pulsed current. The heat input was significantly lower for pulsed current welds as compared to constant current welds, similar to previous work (Abu-Aesh, Taha, Sabbagh & Dorn, 2019).

Table 18: Descriptive statistics results for dependent and independent variables of pulsed current Grade 436. The dependent variables include only the average grain thickness and fusion line angle. These results included 24 observations

Variable	Dependent/ independent variable	Mean	Standard deviation	Median	Minimum	Maximum
Grain thickness (μm)	Dependent	188	55	173	127	381
Fusion line angle (°)	Dependent	71	7	73	51	84
Peak welding current (A)	Independent	165	17	165	140	190
Electrode tip angle (°)	Independent	45	15	45	30	60
Pulse frequency (Hz)	Independent	20	5	20	15	25
Welding speed (mm/s)	Independent	8	2	8	5	10
Heat input (J/mm)	Dependent	225	30	213	188	280

Table 19: Descriptive statistics results for dependent and independent variables of constant current Grade 436. The dependent variables include only the average grain thickness and fusion line angle. These results included 12 observations

Variable	Dependent/ independent variable	Mean	Standard deviation	Median	Minimum	Maximum
Grain thickness (μm)	Dependent	262	66	268	168	388
Fusion line angle (°)	Dependent	76	9	78	58	88
Peak welding current (A)	Independent	155	18	155	130	180
Electrode tip angle (°)	Independent	45	16	45	30	60
Welding speed (mm/s)	Independent	8	2	8	5	10
Heat input (J/mm)	Dependent	294	49	276	239	379

From the descriptive statistical summaries for both Grade 441 and 436, the heat input decreased when pulsed current welding was used, consistent with previous work done by Abu-Aesh, Taha, Sabbagh and Dorn (2019). For Grade 441, the percentage equiaxed grains increased as pulsed current was used for the welding (Figure 41) and the grain size remained largely unchanged. For Grade 436, the grain thickness decreased as pulsed current was used. It could be concluded that the use of pulsed current does have a positive effect on the heat input into the welding process.

5.2 Statistical correlation between welding variables

Figure 65, Figure 66 and Figure **67** illustrate the matrix of scatter diagrams for testing pairs of variables against each other for Grade 441 (percentage equiaxed grains and grain size respectively) and Grade 436 (grain thickness) respectively. (Given the large number of independent and dependent variables associated with the welding of Grade 441, the matrix of scatter diagrams were split into two figures, Figure 65 and Figure 66.)

The Grade 441 matrix of scatter diagrams, Figure 65, indicated that heat input, fusion line angle and % equiaxed grains were correlated, the peak welding current and welding speed had a positive linear relationship and the welding speed and heat input had a decreasing relationship. From these correlations witnessed, further regression analysis could be performed with some idea of welding parameter correlations on the final weld microstructure. The frequency distribution plots on the diagonal line showed that the data

for pulsed current Grade 441 welds were not normally distributed. The correlations seen in Figure 65 warranted further statistical analysis to be done on the pulsed current welding data of Grade 441.

Figure 66 indicates the same welding parameters of welding speed, peak welding current, electrode tip angle, pulse frequency and heat input as in Figure 65 for Grade 441. Figure 66 illustrates the effects of these welding parameters on the grain size and the distance between a pulse, as explained in Figure 21. The Grade 441 matrix of scatter diagrams in Figure 66, indicated that there was no correlation between the heat input and the distance between a pulse on the grain size of Grade 441 weld metal. This was clear from the highly random scattered diagrams between these variables. From the scatter diagrams in Figure 66, it was clear that the welding parameters had no influence on the grain size of Grade 441 weld metal. It was therefore decided that the grain size of Grade 441 weld metal be excluded from further statistical analysis. The distance between a pulse were linearly correlated with peak welding current and welding speed.

Grade 436 matrix of scatter diagrams, Figure 67, did not indicate any correlation between welding variables. This could have been due to the low number of welding samples examined for this ferritic stainless steel grade. The frequency distributions also indicated that the data were not normally but symmetrically distributed, as noted earlier.

For both Grade 441 and 436, only the pulsed current welding data was considered for further statistical analysis. This is due to the low number of samples welded for both grades using a constant current. Further statistical analysis included the Pearson and Spearman correlation coefficients and response surface regression analysis.
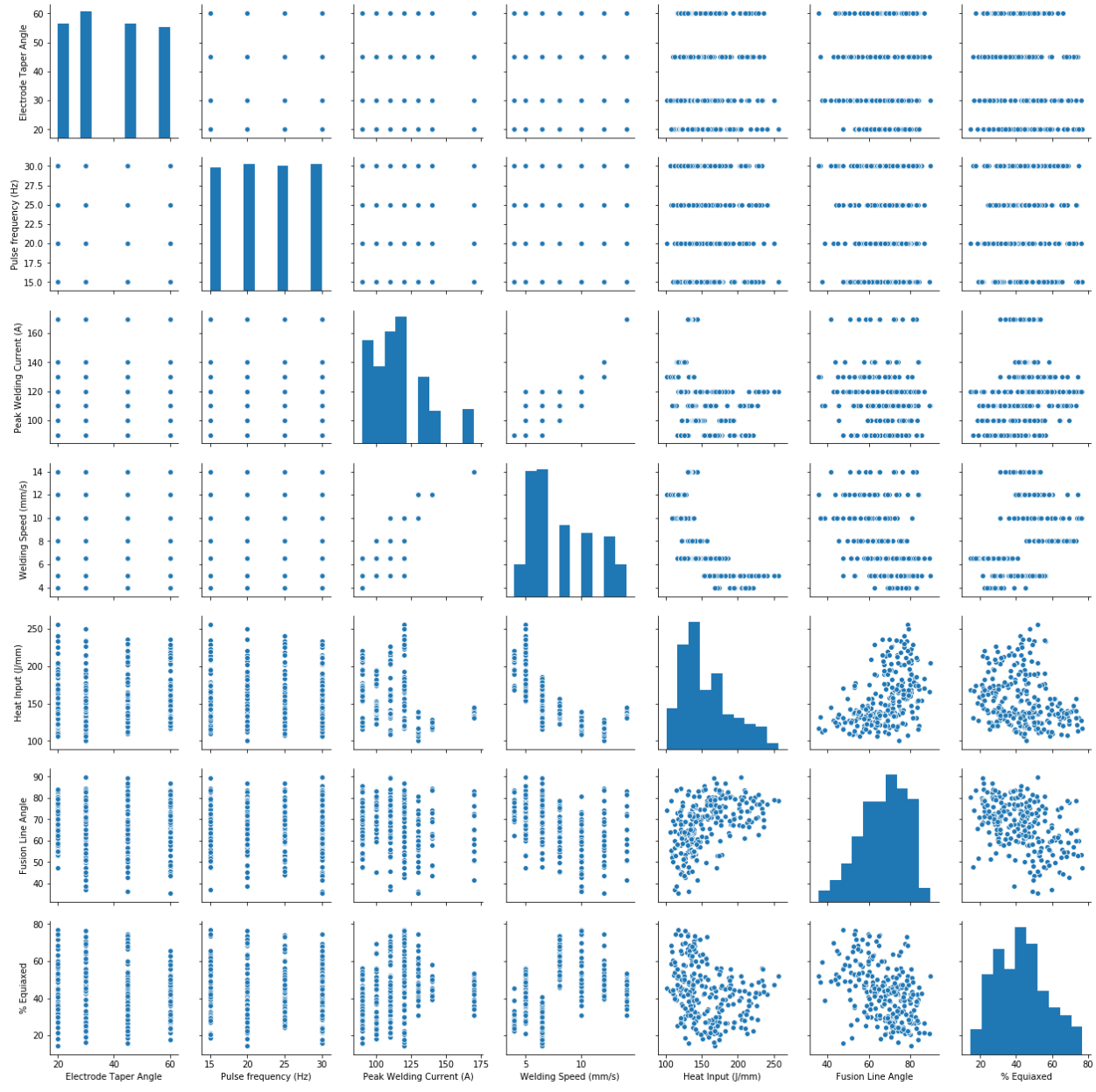
Figure 65: Matrix of scatter diagrams used for Grade 441 pulsed welds to test pairs of variables (dependent and independent) against each other and the percentage equiaxed grains. The plot on the diagonal line shows the distribution of the specific welding variable
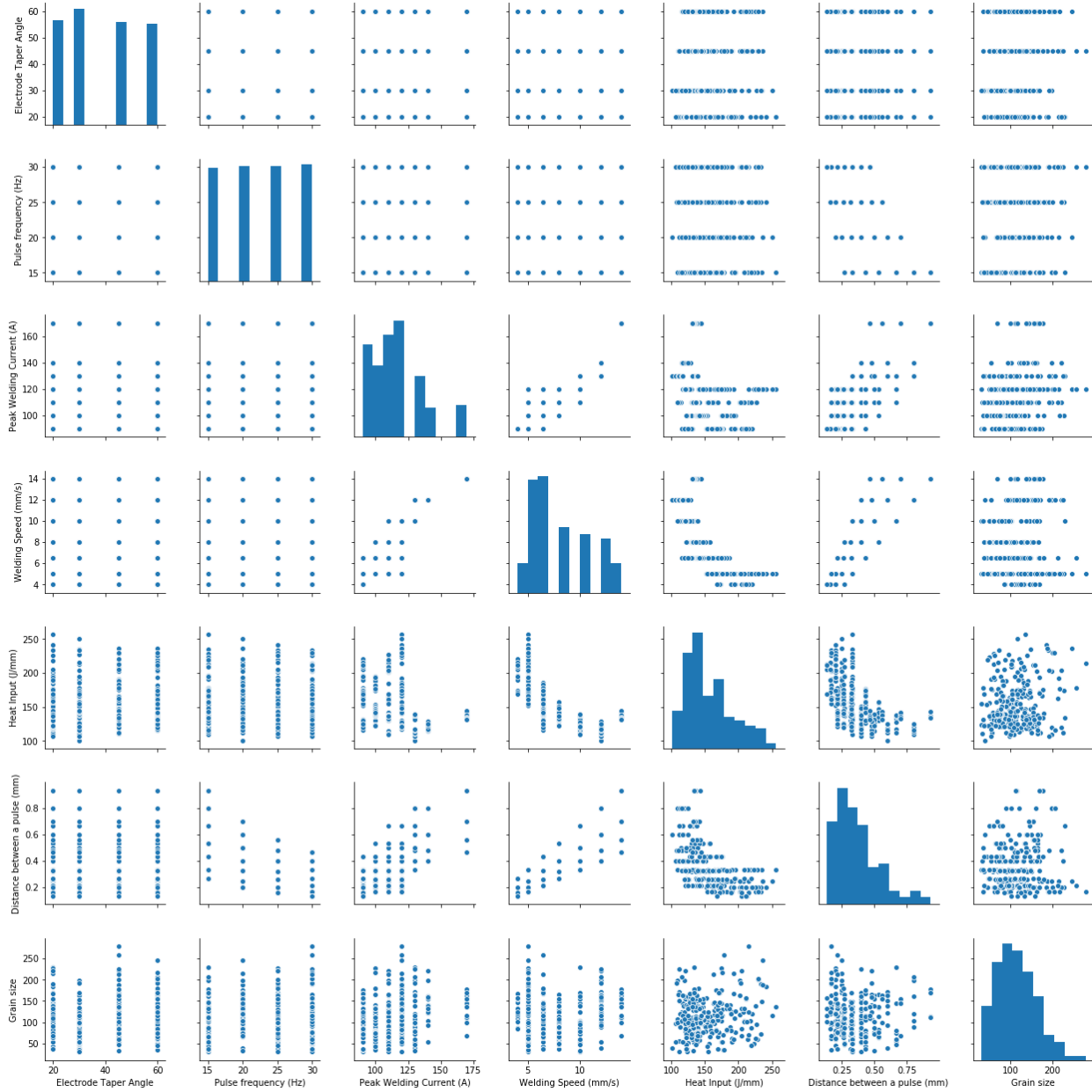
Figure 66: Matrix of scatter diagrams used for Grade 441 pulsed welds to test pairs of variables (dependent and independent) against each other and the grain size and distance between a pulse. The plot on the diagonal line shows the distribution of the specific welding variable
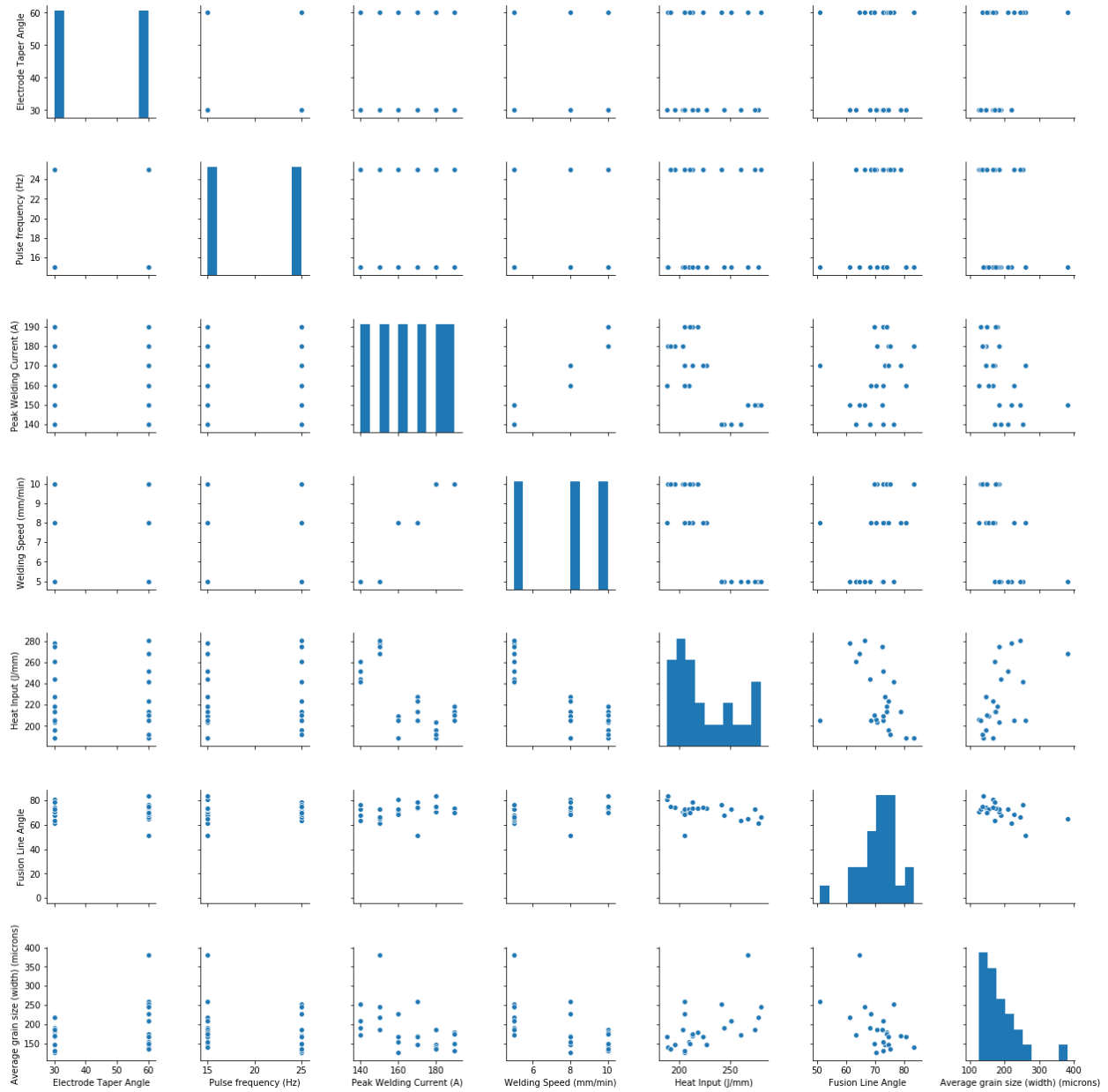
Figure 67: Matrix of scatter diagrams used for Grade 436 pulsed welds to test pairs of variables (dependent and independent) against each other. The plot on the diagonal line shows the distribution of the specific welding variable

Correlation coefficients were determined to examine possible correlations between dependent and independent variables. Table 20 indicates the Pearson correlation coefficient and p-value for Grade 441 pulsed current welds. The p-value is indicated by the bottom number in each column and row. The correlation data indicated that there was multicollinearity between the welding variables. This was seen with high p-values for both welding speed and peak welding current on the heat input - <0.0001. The corresponding Pearson correlation coefficients had a stronger fit for the welding speed data (-0.721) and weaker fit for the peak welding current data (-0.293). This was expected as the heat input is typically calculated by the welding speed and peak welding current; Equation 4, which indicates the conventional equation used to determine the heat input.

From Table 20, the peak welding current, welding speed, heat input and fusion line angle had a statistically significant linear relationship with the percentage equiaxed grains. The welding speed had a positive linear relationship on the percentage equiaxed grains, which indicated that an increase in welding speed, would increase the percentage of equiaxed grains, as was expected from previous work (Abu-Aesh, Taha, Sabbagh & Dorn, 2019). The peak welding current had a negative linear relationship on the percentage of equiaxed grains, which indicated that an increase in peak welding current would decrease the amount of equiaxed grains. The effect of peak welding current and welding speed on the amount of equiaxed grains is consistent with Equation 4 and previous work (Villafuerte, Pardo and Kerr, 1990).

There was a strong statistical linear relationship between the welding speed and peak welding current in Table 20 and Table 21, where the Pearson correlation coefficient equalled 0.849 and Spearman correlation coefficient equalled 0.774. This indicated that the welding speed and peak welding current were strongly dependent on each other, which was expected as the peak welding current was increased to allow full penetration welds, as the welding speed was increased for this study. There was also a very strong statistical linear relationship between the welding speed and the heat input as indicated by the very high Pearson (-0.721) and Spearman (-0.818) correlation coefficients, again as expected from previous work (Abu-Aesh, Taha, Sabbagh & Dorn, 2019; Villafuerte, Pardo and Kerr, 1990).

It could further be concluded that the pulse frequency had no statistical influence on any welding parameter, as indicated by the high p-values, contrary to work by Abu-Aesh, Taha, Sabbagh & Dorn (2019). The

electrode tip angle had a very weak influence on the % equiaxed grains; however, no published evidence was found on the effect of electrode tip angle on the weld metal microstructure.

Table 20: Pearson correlation coefficient (top value) and ρ-value (statistical significance) shown at the bottom of a specific cell, based on 257 observations for Grade 441 pulsed current welds.

	% Equiaxed grains	Fusion line angle (°)	Peak welding current (A)	Electrode tip angle (°)	Pulse frequency (Hz)	Welding speed (mm/s)	Heat input (J/mm)
% Equiaxed grains	1.000	-0.429	0.249	-0.127	-0.027	0.358	-0.261
		<.0001	<.0001	0.042	0.665	<.0001	<.0001
Fusion line angle (°)	-0.429	1.000	-0.174	0.043	-0.033	-0.431	0.491
	<.0001		0.005	0.491	0.599	<.0001	<.0001
Peak welding current (A)	0.249	-0.174	1.000	-0.001	0.006	0.849	-0.293
	<.0001	0.005		0.984	0.918	<.0001	<.0001
Electrode tip angle (°)	-0.127	0.043	-0.001	1.000	0.003	-0.027	0.054
	0.042	0.491	0.984		0.966	0.672	0.387
Pulse frequency (Hz)	-0.027	-0.033	0.006	0.003	1.000	0.018	-0.046
	0.665	0.599	0.918	0.966		0.770	0.463
Welding speed (mm/s)	0.358	-0.431	0.849	-0.027	0.018	1.000	-0.721
	<.0001	<.0001	<.0001	0.672	0.770		<.0001
Heat input (J/mm)	-0.261	0.491	-0.293	0.054	-0.046	-0.721	1.000
	<.0001	<.0001	<.0001	0.387	0.463	<.0001	

Due to the Pearson and Spearman correlation coefficients being similar, the data could be considered to follow a linear relationship. The Spearman correlation coefficient analysis indicated the same statistical trend

than Pearson's, where multicollinearity (where one independent variable is influenced by another independent variable, i.e the welding speed and peak welding current on the heat input) existed.

Table 21: Spearman correlation coefficient (top value) and ρ-value (statistical significance) shown at the bottom of a specific cell, based on 257 observations for Grade 441 pulsed current welds.

	% Equiaxed grains	Fusion line angle (°)	Peak welding current (A)	Electrode tip angle (°)	Pulse frequency (Hz)	Welding speed (mm/s)	Heat input (J/mm)
% Equiaxed grains	1.000	-0.442	0.335	-0.110	-0.024	0.399	-0.297
		<.0001	<.0001	0.080	0.702	<.0001	<.0001
Fusion line angle (°)	-0.442	1.000	-0.172	0.056	-0.019	-0.459	0.523
	<.0001		0.006	0.370	0.762	<.0001	<.0001
Peak welding current (A)	0.335	-0.172	1.000	-0.005	0.008	0.774	-0.348
	<.0001	0.006		0.939	0.896	<.0001	<.0001
Electrode tip angle (°)	-0.110	0.056	-0.005	1.000	0.003	-0.025	0.050
	0.080	0.370	0.939		0.967	0.685	0.426
Pulse frequency (Hz)	-0.024	-0.019	0.008	0.003	1.000	0.020	-0.044
	0.702	0.762	0.896	0.967		0.749	0.479
Welding speed (mm/s)	0.399	-0.459	0.774	-0.025	0.020	1.000	-0.818
	<.0001	<.0001	<.0001	0.685	0.749		<.0001
Heat input (J/mm)	-0.297	0.523	-0.348	0.050	-0.044	-0.818	1.000
	<.0001	<.0001	<.0001	0.426	0.479	<.0001	

Table 22 and Table 23 provide the results for the Pearson and Spearman correlation coefficients, respectively for Grade 436. The number of observations conducted for this ferritic stainless steel grade was 24, close to the minimum required number of observations for statistical analysis (25) for five independent variables. The Pearson correlation coefficients in Table 22 indicated multicollinearity that existed between the heat input, welding speed and peak welding current, as expected per Equation 4 and discussed in Grade 441. The columnar grain thickness was significantly influenced by the welding speed and heat input to a 95% level of confidence.

Similar to Grade 441 welds, there was strong collinearity between welding speed and peak welding current, as expected, where the peak welding current was increased with welding speed to maintain full penetration welds. The strong relationship was indicated by the Pearson correlation coefficient (0.95) and the Spearman correlation coefficient (0.96) in Table 22 and Table 23 respectively.

The Spearman correlation coefficient in Table 23 for Grade 436 pulsed current welds, had small differences to the Pearson correlation coefficients in Table 22, which could indicate that the data is linear and monotonic. The peak welding current and welding speed, therefore, strongly influenced the columnar grain thickness.

The correlation coefficients and p-values in Table 22 and Table 23 indicated that there were not enough data points present to conduct a successful analysis. This was evident for some welding parameters having correlation coefficients (top value) being equal to 0, which indicated no statistical linear relationship and the p-values (bottom value) equal to 1, which indicate no statistical linear significance.

Table 22: Pearson correlation coefficient (top value) and ρ-value (statistical significance) indicated by the bottom value for Grade 436 pulsed current welds. The results indicated included 16 observations

	Grain thickness (microns)	Peak welding current (A)	Electrode tip angle (°)	Pulse frequency (Hz)	Welding speed (mm/s)	Heat input (J/mm)
Grain thickness (microns)	1	-0.476	0.359	-0.228	-0.580	0.551
		0.019	0.085	0.285	0.003	0.005
Peak welding current (A)	-0.476	1	0	0	0.950	-0.696
	0.019		1	1	<.0001	0.0002
Electrode tip angle (°)	0.359	0	1	0	0	-0.037
	0.085	1		1	1	0.862
Pulse frequency (Hz)	-0.228	0	0	1	0	0.019
	0.285	1	1		1	0.930
Welding speed (mm/s)	-0.580	0.950	0	0	1	-0.867
	0.003	<.0001	1	1		<.0001
Heat input (J/mm)	0.551	-0.696	-0.037	0.019	-0.867	1
	0.005	0.0002	0.862	0.929	<.0001	

Table 23: Spearman correlation coefficient (top value) and ρ-value (statistical significance) indicated by the bottom value for Grade 436 pulsed current welds. The results indicated included 16 observations

	Grain thickness (microns)	Peak welding current (A)	Electrode tip angle (°)	Pulse frequency (Hz)	Welding speed (mm/s)	Heat input (J/mm)
Grain thickness (microns)	1	-0.543 0.006	0.265 0.211	-0.265 0.211	-0.619 0.001	0.523 0.009
Peak welding current (A)	-0.543 0.006	1	0 1	0 1	0.956 <.0001	-0.610 0.002
Electrode tip angle (°)	0.265 0.211	0 1	1	0 1	0 1	-0.024 0.911
Pulse frequency (Hz)	-0.265 0.211	0 1	0 1	1	0 1	0.024 0.911
Welding speed (mm/s)	-0.619 0.001	0.956 <.0001	0 1	0 1	1	-0.767 <.0001
Heat input (J/mm)	0.523 0.009	-0.610 0.002	-0.024 0.911	0.024 0.911	-0.767 <.0001	1

The correlation coefficient analyses is summarised in Table 24 for Grade 441 and 436 respectively. The results indicate the statistical significance of the welding parameters on the amount of equiaxed grains for Grade 441 and the columnar grain thickness for Grade 436. Clear from Table 24 is that the Pearson and Spearman correlation coefficients yielded similar results and similar levels of statistical significance for Grade 436. It is for this that the data for Grade 436 could be considered linear and monotonic.

For Grade 441, the Pearson and Spearman analyses had identical results with identical statistical significance. The only difference was that the Pearson correlation coefficient showed that the welding variables had higher levels of significance for the electrode tip angle than for the Spearman correlation coefficient.

Therefore, the percentage of equiaxed grains in Grade 441 was determined by the independent variables: peak welding current, electrode tip angle, welding speed and the dependent variables: fusion line angle and the heat input. The columnar grain thickness of Grade 436 were determined by the independent variables of peak welding current and welding speed and the dependent variable: heat input.

Table 24: List of welding parameters with a statistically significant effect on the % equiaxed grains for Grade 441 and on the columnar grain thickness of Grade 436 with Pearson and Spearman correlation coefficient analysis. Statistical significance is indicated at the bottom of the table

Variable	Grade 441 – percentage equiaxed grade		Grade 436 – columnar grain thickness	
	Pearson pulsed current	Spearman pulsed current	Pearson pulsed current	Spearman pulsed current
Fusion line angle (°)		***	-	-
Peak welding current (A)	***	***	**	***
Electrode tip angle (°)	**	*	-	-
Pulse frequency (Hz)	-	-	-	-
Welding speed (mm/s)	***	***	***	***
Heat input (J/mm)	***	***	***	***

*** Highly significant – Level of significance = 0.01 (99%)

** Significant – Level of significance = 0.05 (95%)

* Significant – Level of significance = 0.1 (90%)

– No significance

5.3 Response surface regression analysis of welding parameters on Grade 441 and 436 weld microstructures

5.3.1 Grade 441 response surface regression analysis

The response surface regression analysis was performed to obtain the best quadratic fit for the set of welding parameters that contributed to the amount of equiaxed grains in Grade 441 and the grain size in Grade 436. The total response surface model indicated that 23.2% of the variance is to be explained by the welding parameters – a low R^2 = 0.232. The response surface model included linear analysis of individual welding parameter effects on the amount of equiaxed grains, the quadratic analysis of each welding parameter and the interaction between different welding parameters as the cross products. The individual model effects of linear, quadratic and cross-products are indicated by Table 25. The table indicated a strong statistical significance of the total model with a ρ-value of <0.0001. For the individual models, only the linear and quadratic effects indicated a strong statistical significance with ρ-values of 0.001 or lower for the linear effects. The welding parameters in the individual effects (linear, quadratic and cross-product) as illustrated by Table 25, is indicated in Table 26.

Table 25: Summary of the individual response surface regression effects applied to the data for determining the % equiaxed grains in Grade 441

Regression	Type I Sum of Squares	R-Square	F Value	Pr > F or ρ-value
Linear effect	8131	0.153	12.01	<.0001
Quadratic effect	4028	0.076	5.95	0.0001
Cross-product effect	223	0.004	0.22	0.9704
Total Model	12382	0.232	5.23	<.0001

Table 26 indicates that the linear welding parameter effects had no statistical significance on the amount of equiaxed grains of Grade 441, as indicated by the high values of Pr > |t| or ρ-values. This indicated multicollinearity to exist between the welding parameters.

Table 26: Parameter estimates and nill-hypothesis test for linear, quadratic and cross product effects of Grade 441

Parameter	Estimate	Standard error	t Value	Pr > |t| or ρ-value
Intercept	-68.105	47.632	-1.43	0.154
Linear				
Peak welding current	1.272	1.01	1.26	0.209
Electrode tip angle	0.095	0.592	0.16	0.873
Pulse frequency	1.005	1.823	0.55	0.582
Welding speed	5.633	6.544	0.86	0.39
Quadratic				
Peak welding current*Peak welding current	-0.004	0.006	-0.63	0.532
Electrode tip angle*Electrode tip angle	-0.002	0.005	-0.32	0.751
Pulse frequency*Pulse frequency	-0.009	0.032	-0.28	0.779
Welding speed*Welding speed	0.175	0.32	0.55	0.584
Cross-product				
Pulse frequency*Peak welding current	-0.004	0.014	-0.29	0.771
Pulse frequency*Electrode tip angle	-0.003	0.01	-0.28	0.777
Electrode tip angle*Peak welding current	0.001	0.005	0.14	0.888
Welding speed*Peak welding current	-0.041	0.08	-0.51	0.612
Welding speed*Electrode tip angle	-0.013	0.037	-0.36	0.723
Welding speed*Pulse frequency	-0.016	0.096	-0.17	0.866

Table 27 summarizes all welding parameters and their relationship effects in the total model to the amount of equiaxed grains in Grade 441. It was clear that the welding speed had a strong statistical significance (ρ-value of 0.0001) and the peak welding current was significant at a 0.1 significance level (ρ-value of 0.0676). From the surface response regression analysis, the electrode tip angle and the pulse frequency had no statistically significant influence on the amount of equiaxed grains. This observation was consistent with the weak Pearson and Spearman correlation coefficients. The welding speed and peak welding current did have a strong significant influence on the amount of equiaxed grains.

Table 27: Summary of independent variable contributions for the total model of linear, quadratic and cross product for Grade 441

Factor	Sum of Squares	Mean Square	F Value	Pr > F or p-value
Peak welding current (A)	1766.413	353.283	2.09	0.0676
Electrode tip angle (°)	701.337	140.267	0.83	0.5301
Pulse frequency (Hz)	220.133	44.027	0.26	0.9344
Welding speed (mm/s)	4546.061	909.212	5.37	0.0001

From the response surface regression analysis, the residual plot fit of the model is illustrated by Figure 68, illustrating the weak fit of the response surface regression (R^2 of 0.232). The figure shows the fit of the actual equiaxed grain percentage to the predicted value, based on the regression model. The ideal model would provide similar values for predicted versus actual, but the actual model for welding parameters was limited to a vertical range between 30 and 60 percent equiaxed grains as predicted by the model.
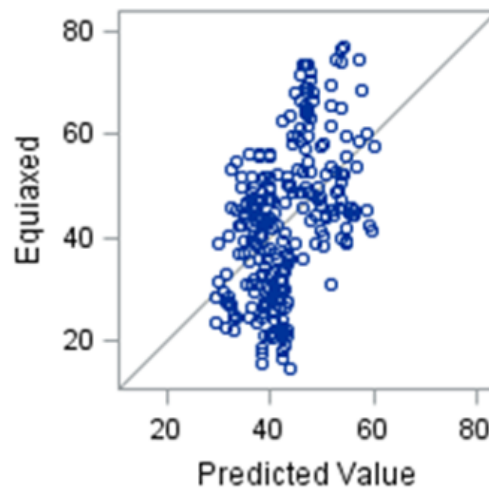
Figure 68: Residual plots for the total model of linear, quadratic and cross-product analysis to predict the amount of equiaxed grains of Grade 441 based on the response surface regression model

The response contours are illustrated by Figure 69 and Figure 70. For plotting both figures, the pulse frequency, peak welding current, electrode tip angle and welding speed were fixed to a specific value. These specific values indicate the optimum value for the individual variables as based upon the regression models in SAS Version 9.4 - Table 25, Table 26 and Table 27. The optimum values determined by the response surface contour plots in Figure 69 and Figure 70 were:

- Welding speed: 8 - 12 mm/s

- Peak welding current: 110 – 130 A

- Electrode tip angle: 20 - 45°

- Pulse frequency: 15 -30 Hz

Both the top contour plots in Figure 69 indicate saddle points between the pulse frequency and electrode tip angle plotted against the peak welding current. The model therefore indicated that at these saddle points, the data points were not local extremes (neither a minimum, nor maximum value). These two plots further indicated that at fixed values of electrode tip angle, pulse frequency and peak welding current, the amount of equiaxed grains changed little. For a welding current between 110 and 130 amperes, the percentage equiaxed grains would not change with a change in electrode tip angle between 20° and 45°. For the same welding current between 110-130 amperes, the percentage equiaxed grains would remain constant for a change in a pulse frequency between 15 to 30 Hertz.

The response contour analysis therefore confirmed that the pulse frequency and electrode tip angle had no effect on the amount of equiaxed grains that form in the weld metal microstructure of Grade 441 - Table 24. The plot of peak welding current against the welding speed in the left bottom figure of Figure 69 indicated a very low error and that for a specific peak welding current, between 110 and 130 amperes, the equiaxed grains would increase as the welding speed is increased from 6.5 mm/s to 12 mm/s. Previous studies showed that, as the welding speed increases to higher values, a corresponding increase in peak welding current is required to maintain full penetration welds (Villafuerte & Kerr, 1990; Villafuerte, Pardo & Kerr, 1990). This confirms the work done by Villafuerte and Kerr (1990), where the increase of welding speed, and consequently the peak welding current, will lead to a decrease in the temperature gradient (G), and increase in the solidification velocity (R), thus increasing the amount of equiaxed grains forming in the weld metal.
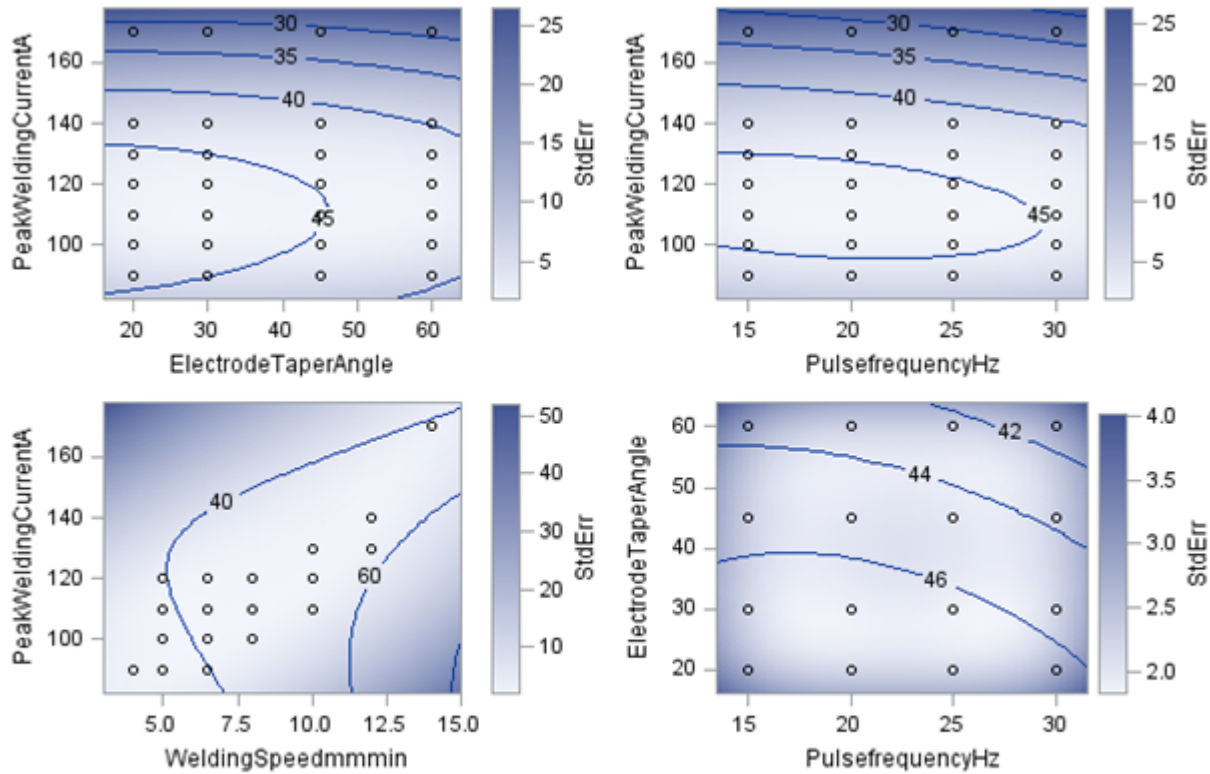
Figure 69: Response surface contours for the % equiaxed grains (values on the contour lines) in Grade 441 with fixed values for peak welding current, electrode tip angle, welding speed and pulse frequency as indicated

Figure 70 further strengthened the argument that the welding speed had the strongest effect on the amount of equiaxed grains. The contours for electrode tip angle and pulse frequency versus welding speed were approximately vertical to the y-axis. This indicated that as the welding speed increased, the equiaxed grain percentage would also increase and that the electrode tip angle and pulse frequency did not have a strong effect on the percentage of equiaxed grains in the weld metal.
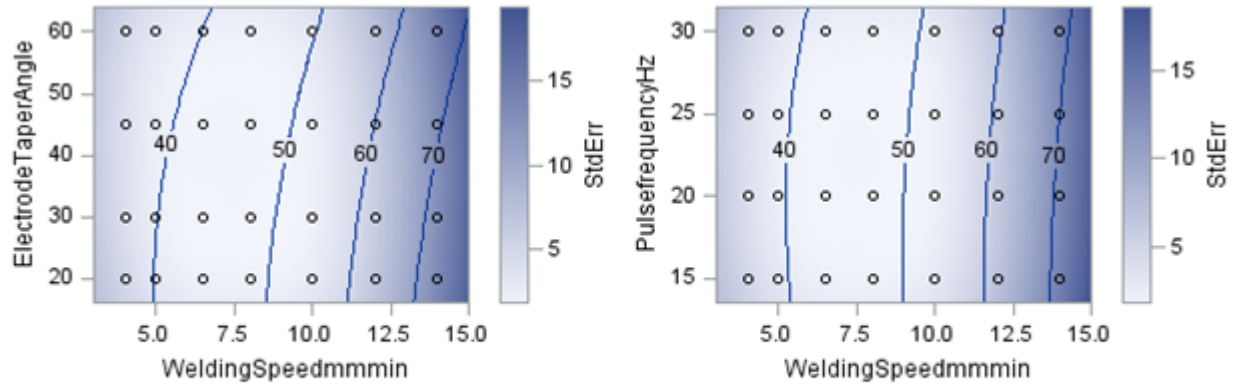
Value when Fixed: Peak Welding Current (A)=115.06, Pulse frequency (Hz)=22.549, Electrode Taper Angle=38. 346

Figure 70: Response surface contours for the % equiaxed grains (values on the contour lines) in Grade 441 with fixed values for peak welding current, pulse frequency and electrode tip angle as indicated

5.3.2 Grade 436 response surface regression analysis

As noted previously, Grade 436 welds had a fully columnar microstructure. From the response surface regression analysis, the model had a high R^2-value of 0.80. This indicated that 80% of the variation in average columnar grain thickness in the weld metal was explained by the welding parameters. Again, the total model included the linear, quadratic and cross-product interactions to the average columnar grain thickness. It is clear that even though there was not a strong statistical significance between the regression models and the average columnar grain thickness, the linear effects provided the strongest significance of all three effects tested, as indicated by the low p-value of 0.003 - Table 28.

Table 28: Summary of individual response surface regression effects applied to the data for determining the average columnar grain thickness in Grade 436

Regression	Type I Sum of Squares	R-Square	F Value	Pr > F or p-value
Linear effect	41758	0.575	7.96	0.0029
Quadratic effect	2076	0.029	0.79	0.4775
Cross-product effect	14392	0.198	1.83	0.1827
Total Model	58226	0.801	3.70	0.0191

The linear, quadratic and cross-product effects discussed in Table 28 are tabulated in Table 29. There were no individual welding parameters that had a statistically significant influence on the weld metal columnar grain thickness other than the cross-product of pulse frequency and peak welding current with a p-value of 0.074 and the cross-product of pulse frequency and peak welding speed with a p-value of 0.075. The linear welding parameter effects in the model indicated that there was no statistical significance with high values for Pr > |t| or p-values. This further strengthened the conclusion that multicollinearity existed between independent variables and the significantly strong influence of peak welding current and welding speed on one another as previously discussed with Table 22 and Table 23.

Table 29: Parameter estimates and null-hypothesis test for the linear, quadratic and cross product effects of Grade 436

Parameter	Estimate	Standard error	t Value	Pr > |t| or ρ-value
Intercept	-692.381	4422.788	-0.16	0.878
Linear				
Peak welding current	-1.185	82.971	-0.01	0.989
Electrode tip angle	-2.906	10.028	-0.29	0.777
Pulse frequency	52.739	29.828	1.77	0.105
Welding speed	112.733	650.560	0.17	0.866
Quadratic				
Peak welding current*Peak welding current	0.087	0.395	0.22	0.831
Pulse frequency*Pulse frequency	0.000	.	.	.
Electrode tip angle*Electrode tip angle	0.000	.	.	.
Welding speed*Welding speed	12.808	25.779	0.5	0.629
Cross-product				
Pulse frequency*Peak welding current	-0.548	0.277	-1.98	0.074
Pulse frequency*Electrode tip angle	0.009	0.099	0.09	0.931
Electrode tip angle*Peak welding current	0.082	0.092	0.89	0.393
Welding speed*Peak welding current	-2.293	6.274	-0.37	0.722
Welding speed*Electrode tip angle	-1.238	0.767	-1.61	0.135
Welding speed*Pulse frequency	4.527	2.302	1.97	0.075

Table 30 summarises the different welding parameters and their relationships to the average columnar grain thickness. The welding speed had a strong statistical significance on the average columnar grain thickness, similarly to the amount of equiaxed grains of Grade 441. For Grade 436 welds, the electrode tip angle also had a similar statistically significant influence on the columnar grain thickness than the welding speed, where both fell within a 0.05 significance level or 95% level of confidence.

Table 30: Summary of independent variable contribution for the total model of linear, quadratic and cross product for Grade 436

Factor	Sum of Squares	Mean Square	F Value	Pr > F or ρ-value
Peak welding current (A)	12226	2445.251	1.86	0.181
Electrode tip angle (°)	18335	4583.644	3.49	0.045
Pulse frequency (Hz)	9011	2252.836	1.72	0.216
Welding speed (mm/s)	22913	4582.659	3.49	0.039

From the response surface regression analysis, the residual plot fit of the model is illustrated by Figure 71. The relatively strong fit of the response surface regression (R^2 of 0.80) is illustrated by data following the ideal line drawn in the figure. The relatively strong fit of the data could be attributed to the low number of datapoints included for the welding of Grade 436.
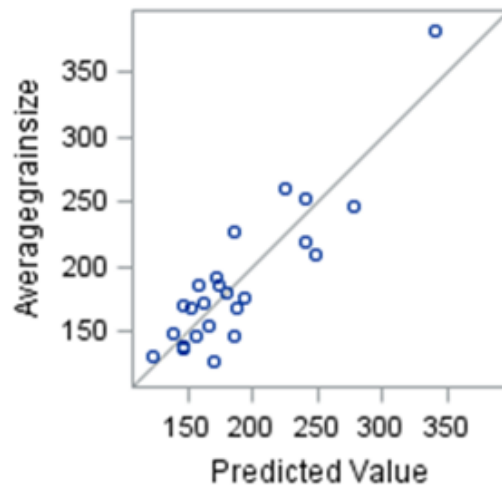
Figure 71: Residual plots for the total model of linear, quadratic and cross-product analysis to predict the average columnar grain thickness of Grade 436 based on the response surface regression model

The response contours of Grade 436 are illustrated by Figure 72 and Figure 73. The pulse frequency, peak welding current, electrode tip angle and welding speed were fixed to a specific value by SAS Version 9.4 to draw the contour plots. The optimum values determined from the contour plots were:

- Welding speed: 8 - 10 mm/s
- Peak welding current: 1140 - 170 A
- Electrode tip angle: 30 - 60°
- Pulse frequency: 15 - 25 Hz

Saddle points were witnessed for the top figures in Figure 72. It is clear from the top left figure that the electrode tip angle had a small effect on the average columnar grain thickness at peak welding currents between 150 and 170 amperes, which is consistent with the Pearson correlation coefficient in Table 22. Clear from the contour plots is the higher standard error beyond the optimum values discussed earlier, as expected with smaller data sets. The contour plots indicated that the welding parameters did in fact have a good

relationships with the average columnar grain thickness. The contour plots were consistent with the results of the Pearson and Spearman correlation coefficients. It seems that all welding parameters influenced the thickness of the columnar grains during current pulsing of Grade 436. The same results were concluded from Figure 73, where the optimum welding speed was determined to be between 8 to 10 mm/s to provide the smallest average columnar grain thickness.
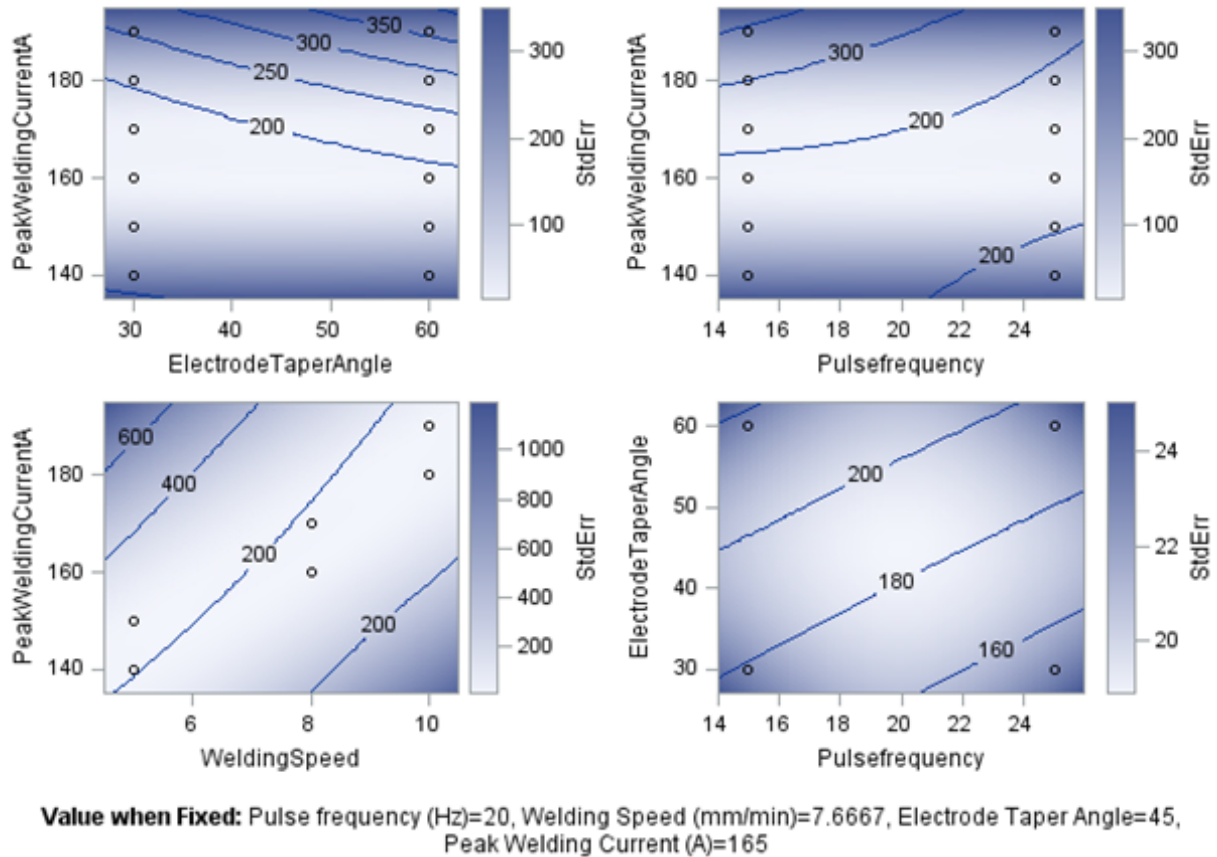
Figure 72: Response surface contours for the average columnar grain thickness in Grade 436 with fixed values for peak welding current, electrode tip angle, welding speed and pulse frequency, as indicated
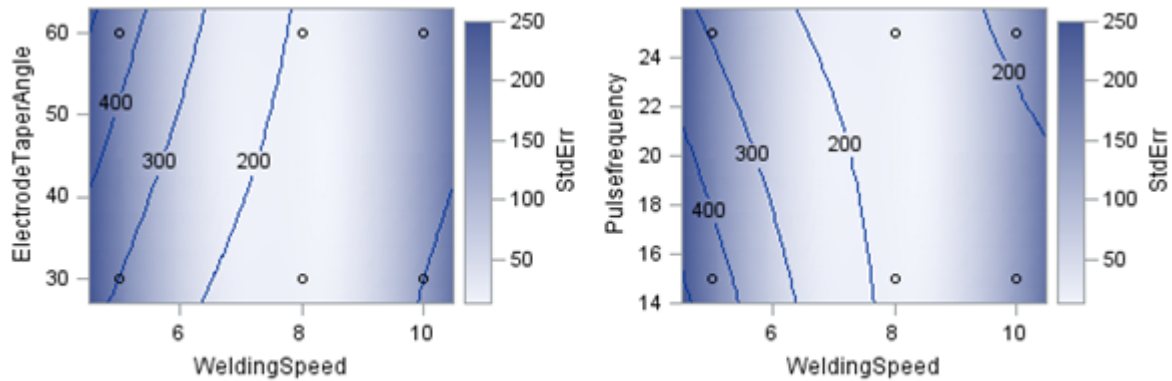
Figure 73: Response surface contours for the average columnar grain thickness in Grade 436 with fixed values for peak welding current, pulse frequency and electrode tip angle, as indicated

5.4 Explanation of results of statistical analysis in terms of the behaviour of weld metal

5.4.1 Grade 441

For Grade 441, a pulsed current had an effect on the amount of equiaxed grains that formed as compared to constant current, as illustrated by Figure 41 where the equiaxed grain amount increased with the use of pulsed current with a selected subset of welds. The equiaxed grain formation can only partly be explained by the welding parameters: welding current, welding speed, pulse frequency and electrode tip angle. This was also supported by the statistical analysis by using the response surface methodology. It indicated that the variation in amount of equiaxed grains could only be explained by 23% ($R^2 = 0.23$).

The statistical analysis indicated that the equiaxed grain percentage was mainly determined by the peak welding current and the welding speed, consistent with previous results (Villafuerte & Kerr, 1990). The pulse frequency had no statistical influence on the formation of equiaxed grains in the autogenous GTAW of Grade 441 ferritic stainless steel. Figure 74 indicates the distribution of the distance associated with a pulse. This figure indicates that there was minimal variance in the distance associated with a pulse and it was distributed close to the average. With the narrow distribution of distance associated with a pulse (less than 1 mm), the pulse frequency had a very small effect on the distance associated with a pulse. The small difference in the distance associated with a pulse is consistent with the statistical results where pulse frequency (between 15-30 Hz) had no significant effect on the equiaxed grain percentage.

The response surface regression methodology indicated that there was a significant influence of the electrode tip angle on the amount of equiaxed grains in Grade 441 weld metal. However, the response surface regression contour plots in Figure 69 and Figure 70, showed that the electrode tip angle between 20° and 45° did not influence the amount of equiaxed grains due to a saddle point in the data, where the equiaxed grain percentage would be close to 45%. The response surface regression contour plots also show that for a higher tip angle (60°), the equiaxed grain amount would be close to 40%. This small difference in equiaxed grain percentage with regards to change in electrode tip angle, indicates that the electrode tip angle has no significant influence on the percentage of equiaxed grains in Grade 441 weld metal. The reasons for this lack of effect is not quite clear.
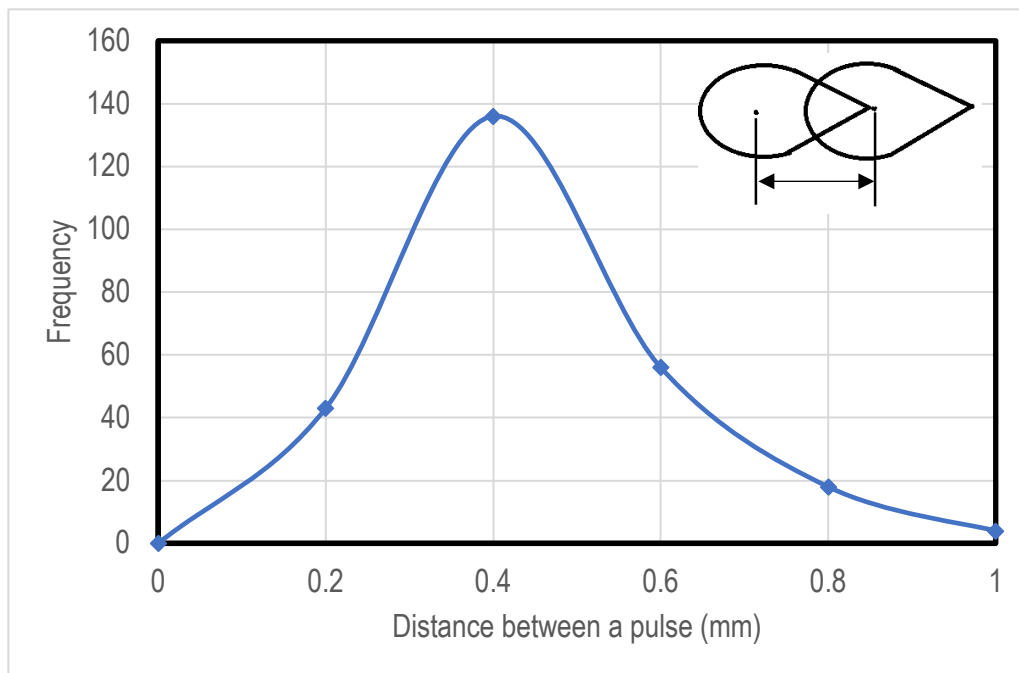
Figure 74: Distribution of the distance associated with a pulse (a function of the welding speed and pulse frequency) for Grade 441 pulsed welds

The elongation of Grade 441 autogenous welds was not a function of the amount of equiaxed grains present, but rather on the amount of weld metal present in the gauge area of tensile coupons. This phenomenon was confirmed by the strong fit of the elongation curve to actual results in Figure 51.

The fracture surface of the tensile coupons of Grade 441 indicated that the base material underwent a ductile fracture as confirmed by the presence of spherical dimples. The weld metal of Grade 441, regardless of the

113

amount of equiaxed grains and percentage weld metal in the gauge area of the tensile coupon, indicated spherical ductile dimples, cleavage fracture and intergranular fracture.

The titanium content present in the base material of ferritic stainless steels, could have a significant influence on the final microstructural features (formation of equiaxed grains). The work of Villafuerte and Kerr (1990) supports the notion that an increase in the amount of titanium content in the base material would increase the amount of equiaxed grains in the weld metal (Villafuerte & Kerr, 1990). This phenomenon was observed with the current Grade 441 that was investigated, where it seemed that the material lied within a transition of high or low amounts of equiaxed grains – as was witnessed in Figure 64. It is possible that a higher titanium content than that currently used will result in a fully equiaxed weld microstructure.

Villafuerte, Kerr and David (1995) stated that TiN precipitates were found in the centers of equiaxed grains and were most likely the heterogeneous nucleation sites for the formation of equiaxed grains. This could be true, but SEM-EDS analysis in this work indicated that these TiN precipitates were present throughout the entire weld microstructure. These precipitates were found distributed throughout the equiaxed grains, on grain boundaries and within the columnar grains. A better understanding of the influence of the titanium content requires further investigation.

5.4.2 Grade 436

Villafuerte, Kerr and David (1995) stated that a fully columnar weld microstructure should be expected with a ferritic stainless steel grade that contained no titanium. This was observed with Grade 436 (no titanium) where fully columnar grain structures were present, regardless of the welding parameters. The use of a pulsed current did not have a significant influence on the thickness of columnar grains. The welding speed and peak welding current were the main welding parameters to have influenced the columnar grain thickness. The electrode tip angle had a statistically significant effect on the columnar grain thickness of Grade 436.

The elongation of Grade 436 was not statistically strong influenced by the columnar grain thickness, nor the amount of weld metal present in the gauge area of the tensile coupons. This was illustrated by the weak R^2 of 0.19 in Figure 55. The Grade 436's fracture surface indicated ductile spherical dimples, cleavage fracture and intergranular fracture to be the modes of failure. It is not clear why the electrode tip angle had a statistically significant influence on the grain size for Grade 436.

CHAPTER 6: Conclusions

For Grade 441, a ferritic stainless steel with 0.18% titanium, the following conclusions could be made:

- Grade 441 had a broad range of the fraction of equiaxed grains with pulsed and constant current welding. The equiaxed grains in Grade 441 weld metals were only partly explained by the welding parameters as statistical analysis indicated an R^2 of 0.23 with highly statistical significance of welding speed and peak welding current.

- Current pulsing decreased the heat input and increased the equiaxed grain percentage relative to the constant current welds.

- The pulse frequencies between 15 and 30Hz had no statistically significant effect on the formation of equiaxed grains for Grade 441 or on the thickness of columnar grains in Grade 436.

- The electrode tip angle (between 30-60°) had no statistically significant effect on the formation of equiaxed grains in Grade 441.

  - The results indicated that Grade 441 (0.18% Ti) provided for this study, had a titanium content that was likely to be in the transition zone between high and low amounts of equiaxed grains.

For Grade 436, a molybdenum-containing titanium free alloy, the following conclusions could be made:

- Grade 436 had a fully columnar weld metal microstructure regardless of pulsed or constant current.

- The columnar grain thickness of Grade 436 weld metal had a strong response surface regression fit to the data with an R^2 of 0.8. The grain size was strongly influenced by the welding speed, peak welding current and electrode tip angle.

For both grades, elongation was found not to be a function of the amount of equiaxed grains present, but rather depends on the amount of weld metal present in the gauge area of tensile coupons.

CHAPTER 7: Recommendations

7.1 Welding of components manufactured using Grades 441 and 436

- The use of pulsed current rather than constant current, will decrease the heat input and increase the fraction of equiaxed grains in the weld metal. Changes to the pulse frequency between 15-30 Hz, does not have any effect on the equiaxed grain percentage. The pulse frequency could therefore be set to any desired value between those limits.

- The electrode tip angle has no effect on the fraction of equiaxed grains in the weld metal.

- When possible, the titanium content needs to be about 0.20% or more to ensure that high amounts of equiaxed grain weld microstructures are achieved.

7.2 Further experimental work

- The titanium content seems to have a larger effect on the amount of equiaxed grains than the welding parameters. A systematic study of the effect of the titanium content on the fraction of equiaxed grains is recommended. Various techniques exist to change the titanium content of the weld metal.

- The aluminium content in the base material also seems to have an influence on the formation of equiaxed grains. It could therefore be useful to test welds at high and low amounts of aluminium contents.

- The pulse frequency and electrode tip angles did not have a large influence on the amount of equiaxed grains that formed. Therefore, further investigation should focus on high and low welding speeds and welding currents.

REFERENCES

Abbaschian, R., Abbaschian, L. and Reed-Hill, RE. (2009). Physical metallurgy principles. Stamford, Connecticut; Cengage Learning.

Abu-Aesh, M., Taha, M., El -Sabbagh, A., and Dorn, L. (2019). Welding of fully – Austenitic stainless steel using PCGTAW process; Part I: Bead structure. *Journal of Manufacturing Processes, 38*, 21–29. DOI: 10.1016/j.jmapro.2018.12.037

Amuda, MOH. and Mridha, S. (2012). Comparative Evaluation of Grain Refinement in AISI 430 FSS Welds by Elemental Metal Powder Addition and Cryogenic Cooling, *Materials and Design, 35(2012)*, 609–618. DOI: 10.1016/j.matdes.2011.09.066.

Analytics Vidhya Content Team. (2019). Statistics foo data science: Introduction to t-test and its different types (with implementation in R). Online available: https://www.analyticsvidhya.com/blog/2019/05/statistics-t-test-introduction-r-implementation/ [Visited: 27 September]

Anttila, S. and Heikkinen, H. (2014). Study of weldability. *Structural Application of Ferritic Stainless Steels (SAFSS), 2.* Tornio, Finland; Outokumpu Stainless Oy.

ASTM E8 (2013) Standard Test Methods for Tension Testing of Metallic Materials. ASTM International.

AWS Committee on B4 Committee on Mechanical Testing of Welds. (2016). *Standard Methods for Mechanical Testing of Welds (8th Edition) - AWS B4.0:2016.* American Welding Society (AWS). Online available: https://app.knovel.com/hotlink/toc/id:kpSMMTWE02/standard-methods-mechanical/standard-methods-mechanical

Baghel, PK. and Nagesh, DS. (2016). Pulse TIG welding: Process, Automation and Control. *Journal for Welding and Joining*. DOI: 10.5781/JWJ.2016.00255

Bell, T. (2018). Ferritic Stainless Steel. *The Balance*. Online available: https://www.thebalance.com/metal-profile-ferritic-stainless-steel-2340133

British Standards Institution (BSI) (2005). BS EN 10088-2: Stainless steels – Part 1: List of stainless steels. European Committee for Standardization. Chiswick High Road, London.

Butte, S. (2014). Multivariate analysis of gas metal arc welding defects using principal component analysis approach. *SeekOptima Research Review Conference. Online available:* https://www.researchgate.net/publication/269764807_Multivariate_Analysis_of_Gas_Metal_Arc_Welding_Defects_Using_Principal_Component_Analysis_Approach

Callister, WD. and Rethwisch, DG. (2011). Material Science and Engineering. Hoboken, New Jersey; John Wiley & Sons Inc.

Chalmers, B. (1964). Principles of Solidification. Hoboken, New Jersey; John Wiley & Sons Inc.

Columbus Stainless (Pty) Ltd, (2011). Standard Ferritic Stainless Steels: Technical Brochure. Online available: https://www.columbus.co.za/downloads/Ferritics_Standard.pdf

David, SA., Babu, SS. and Vitek, JM. (2003). Welding: Solidification and microstructure. *JOM: The Journal of The Minerals, Metals & Material Society*, *55*(6), 14–20. DOI: 10.1007/s11837-003-0134-7

Davis, JR. (1993). *Metals handbook. Vol. 1, Properties and selection: irons, steels, and high-performance alloys,* Materials Park, ASM International.

Diamond Ground Products (2013). Guidebook for the proper selection and preparation of tungsten electrodes for arc welding. Online available: https://44s8c5wyz4734tca273b4ltn-wpengine.netdna-ssl.com/TungstenGuidebook.pdf

Easterling, K. (1992). Introduction to the physical metallurgy of welding. Second edition. Jordan Hill, Oxford; Butterworth-Heinemann Ltd.

Farahani, E., Shamanian, M. and Ashrafizadeh, F. (2012). A comparative study on direct and pulsed current gas tungsten arc welding of alloy 617. *AMAE International Journal on Manufacturing and Material Science, 2(1), 1-6.*

Fattah-alhosseini, A., Vafaeian, S., 2015. Comparison of electrochemical behavior between coarse-grained and fine-grained AISI 430 ferritic stainless steel by mottschottky analysis and EIS measurements. J. Alloy. Compd. 639, 301–307.

Folkhard, E. (1987). Welding Metallurgy of stainless steels. Wien, New York; Springer-Verlag. DOI: 10.1007/978-3-7091-8965-8

Fu, J.W., Qiu, W.X., Nie, Q.Q., Wu, Y.C., 2017b. Precipitation of TiN during solidification of AISI 439 stainless steel. J. Alloy. Compd. 699, 938–946

Inoue, Y., Kikuchi, M. (2003). Present and future trends of stainless steel for automotive exhaust system. *Nippon Steel technical report No. 88.* Online available: https://www.nipponsteel.com/en/tech/report/nsc/pdf/n8814.pdf

Jooste, F. (2019). Heat input calculation using current and voltage measurements. Literature Review NLO 700. University of Pretoria, South Africa.

Jordaan, J. (2019). Statistical Consultation. 4 July 2019. Department of Statistics, University of Pretoria, South Africa.

Jula, M., Dehmolaei, R., and Alavi Zaree, SR. (2018). The comparative evaluation of AISI 316/A387-Gr.91 steels dissimilar weld metal produced by CCGTAW and PCGTAW processes. *Journal of Manufacturing Processes*, *36*, 272–280. DOI: 10.1016/j.jmapro.2018.10.032

Kang, M., Ryznar, R. (2007). 11.220 Quantitative reasoning and statistical methods for planning. Massachusetts Institute of Technology, Department of Urban Studies and Planning. Online available: http://web.mit.edu/11.220/www05/brushup/spss/boxplot.htm

Kang, Y., Zhang, Z., Wang, H. and Qin, Q. (2005). Experimental investigation of the effect of thickness on fracture toughness of metallic foils. *Materials Science & Engineering A*, 394(1), 312–319. DOI: 10.1016/j.msea.2004.11.044.

Karunakaran, N. and Balasubramanian, V. (2011). Effect of pulsed current on temperature distribution, weld bead profiles and characteristics of gas tungsten arc welded aluminum alloy joints. *Transactions of Nonferrous Metals Society of China*, *21*(2), 278–286. DOI: 10.1016/S1003-6326(11)60710-3

Kenton, W. (2019). Tools for Fundamental Analysis, T-Test. Online available: https://www.investopedia.com/terms/t/t-test.asp

Kim, WH. and Na, S.J. (1998). Heat and fluid flow in pulsed current GTA weld pool. *International Journal of Heat and Mass Transfer*, *41*(21), 3213–3227. DOI 10.1016/S0017-9310(98)00052-0

Kou, S. (2003). Welding Metallurgy. Hoboken, New Jersey; John Wiley & Sons Inc.

Kou, S. and Le, Y. (1988). Welding parameters and the grain structure of weld metal – A thermodynamic consideration. *Metallurgical Transactions A, 19A*, 1075-1082.

Lakshminarayanan, A. K., & Balasubramanian, V. (2012). Evaluation of Microstructure and Mechanical Properties of Laser Beam Welded AISI 409M Grade Ferritic Stainless Steel. *Journal of Iron and Steel Research, International*, *19*(1), 72–78. DOI: 10.1016/S1006-706X(12)60050-8

Lakshminarayanan, A., Shanmugam, K. and Balasubramanian, V. (2009). Effect of Autogenous Arc Welding Processes on Tensile and Impact Properties of Ferritic Stainless Steel Joints. *Journal of Iron and Steel Research, International, 16(1)*, 62 - 16. DOI: 10.1016/S1006-706X(09)60012-1.

Lippold, JC. (2015). Welding metallurgy and weldability. Hoboken, New Jersey; John Wiley & Sons Inc.

Lippold, JC., and Kotecki, DJ. (2005). Welding metallurgy and weldability of stainless steels. Hoboken, New Jersey; John Wiley & Sons Inc.

Madhusudhan Reddy, G., Mohandas, T., Sambasiva Rao, A., and Satyanarayana, VV. (2005). Influence of welding processes on microstructure and mechanical properties of dissimilar austenitic-ferritic stainless steel welds. *Materials and Manufacturing Processes*, *20*(2), 147–173. DOI: 10.1081/AMP-200041844

Mallaiah, G., Kumar, A., Ravinder Reddy, P. and Madhusudhan Reddy, G. (2012). Influence of Grain Refining Elements on Mechanical Properties of AISI 430 Ferritic Stainless Steel Weldments - Taguchi Approach. *Materials and Design*, 36. 443–450. DOI: 10.1016/j.matdes.2011.11.063.

Manikandan, M., Nageswara, RM., Ramanujam, R. and Ramkumar, D. (2014). Optimization of the pulsed current gas tungsten arc welding process parameters for alloy C-276 using the Taguchi method. *Procedia Engineering, 97*, 767-774.

McElhinny, MW. and McFadden, PL. (2000). International Geophysics, Chapter Two – Rock Magnetism. Volume 73, Academic Press. DOI: [10.1016/S0074-6142(00)80095-9](10.1016/S0074-6142(00)80095-9)

McGuire, MF. (2008). Stainless Steels for Design Engineers. Materials Park, Ohio; ASM International.

Melfi, T. and Daniel, J. (2010). Measurement of heat input in complex wave form welding. *Materials at high temperatures, 27*, 201.

Mmadi, MC. (2016). The microstructure and properties of autogenous gas tungsten arc and laser welds in type 441 ferritic stainless steel. Master's dissertation; University of Pretoria, South Africa.

Montgomery, DC. and Runger, GC. (2014). Applied statistics and probability for engineers. Sixth edition. International student version. Hoboken, New Jersey; John Wiley & Sons Singapore Pte. Ltd.

O'Brien, A. and Guzman, C. (2011). Welding handbook Volume 4: Materials and applications. Part 1. Ninth edition. ed. Miami, Florida; American Welding Society.

Omar, A.A, Lundin, C.D. (1979). Pulsed Plasma-Pulsed GTA Arc: A Study of the Process Variables. *Supplement to the Welding Journal, April 1979.* American Welding Society. Online available: https://app.aws.org/wj/supplement/WJ_1979_04_s97.pdf

Ramkumar, KD., Chandrasekhar, A., Singh, AK., Ahuja, S., Agarwal, A., Arivazhagan, N., & Rabel, AM. (2015). Comparative studies on the weldability, microstructure and tensile properties of autogeneous TIG welded AISI 430 ferritic stainless steel with and without flux. *Journal of Manufacturing Processes*, *20*, 54–69. DOI: 10.1016/j.jmapro.2015.09.008

Reddy, GM. and Mohandas, T. (2001). Explorative studies on grain refinement of ferritic stainless steel welds. *Journal of Materials Science Letters*, *20*(8), 721–723. DOI: [10.1023/A:1010963025259](10.1023/A:1010963025259)

Saedi, HR. and Unkel, W. (1988). Arc and weld pool behaviour for pulsed current GTAW. *Supplement to the Welding Journal*, November 1988.

SAS Institute Inc. (2013). *SAS/STAT® 13.1 User's Guide: The RSREG Procedure.* North Carolina, USA.

Savage, WF., Nippes, EF. and Miller, TW. (1976). Microsegregation in 70Cu-30Ni weld metal. *Welding Journal, 55(6),* 165-173

Shan, Y., Luo, X., Hu, X. and Liu, S. (2010). Mechanisms of Solidification Structure Improvement of Ultra-Pure 17 wt% Cr Ferritic Stainless Steel by Ti, Nb Addition. *Journal of Materials Science & Technology, 27(4)*, 352-358. DOI: 10.1016/S1005-0302(11)60073-X.

Shi, C., Cheng, G., Li, Z., Zhao, P., 2008. Solidification structure refining of 430 ferrite stainless steel with TiN nucleation. J. Iron Steel Res. Int. 15, 57–60.

Singh, R. (2012). Applied Welding Engineering: Processes, Codes, and Standards. Waltham, Massachusetts; Butterworth-Heinemann.

The American Society of Mechanical Engineers (2017). An international Code, 2015 ASME Boiler and Pressure Vessel Code. *ASME Section IX: Qualification Standard for Welding, Brazing and Fusing Procedures; Welders; Brazers and Welding, Brazing and Fusing Operators.* 2017 Edition. Two Park Avenue, New York, USA.

The James F. Lincoln Arc Welding Foundation, (2000). The procedure handbook of arc welding. Fourteenth edition. Cleveland, Ohio, USA.

Tong, Z., Zhentai, Z. and Rui, Z. (2013). A dynamic welding heat source model in pulsed current gas tungsten arc welding. *Journal of Materials Processing Technology*, *213*(12), 2329–2338. DOI: 10.1016/j.jmatprotec.2013.07.007

Underwood, EE. (1970). Quantitative Stereology. Reading, Massachusetts; Addison-Wesley Publishing Company.

Van Niekerk, CJ., Du Toit, M. and Erwee, MW. (2012). Sensitization of AISI 409 Ferritic Stainless Steel During Low Heat Input Arc Welding. *Welding in the World*, 56(5), 54-64, , DOI: 10.1007/bf03321350.

Villafuerte, JC. and Kerr, HW. (1990). Electromagnetic stirring and grain refinement in stainless steel GTA welds. *Supplement to the Welding Journal, January 1990*. Online available: https://app.aws.org/wj/supplement/WJ_1990_01_s1.pdf

Villafuerte, JC., Kerr, HW. and David, SA. (1995). Mechanisms of equiaxed grain formation in ferritic stainless steel gas tungsten arc welds. *Materials Science and Engineering: A*, *194*(2), 187–191. DOI: 10.1016/0921-5093(94)09656-2

Villafuerte, JC., Pardo, E. and Kerr, HW. (1990). The effect of alloy composition and welding conditions on columnar-equiaxed transitions in ferritic stainless steel gas-tungsten arc welds. *Metallurgical Transactions A, 2(7)*, 2009-2019. DOI: 10.1007/BF02647249.

Villaret, V., Deschaux-Beaume, F. and Bordreuil, C. (2016). A solidification model for the columnar to equiaxed transition in welding of a Cr-Mo ferritic stainless steel with Ti as inoculant. *Journal of Materials Processing Technology,* 233, 115 - 124. DOI: 10.1016/j.jmatprotec.2016.02.017

Villaret, V., Deschaux-Beaume, F., Bordreuil, C., Rouquette, S. and Chovet, C. (2013). Influence of filler wire composition on weld microstructures of a 444 ferritic stainless steel grade. *Journal of Material Processing Technology, 213(9),* 1538-1547. DOI: 10.1016/j.jmatprotec.2013.03.026.

Zhang, H., Zhang, H., Zhao, X., Wang, Y., and Li, N. (2016). Study of Thickness Effect on Fracture Toughness of High Grade Pipeline Steel. *MATEC Web of Conferences*, 67. DOI: 10.1051/matecconf/20166703016.